



UiT The Arctic University of Norway

Faculty of Science and Technology
— Department of Mathematics and Statistics

**Efficient Bayesian analysis of long memory processes
applied to climate**

—

Eirik Myrvoll-Nilsen

A dissertation for the degree of Philosophiae Doctor – January 2020

ABSTRACT. Temperature fluctuations can be described by a persistent correlation structure known as long-range dependence (LRD). This is a phenomenon which implies that the autocorrelation function follows a power-law decay and that observations may still be significantly correlated even if the temporal or spatial distance between them is large. Moreover, temperature is widely known to be influenced by radiative forcing, or how much of the solar radiation is absorbed by the earth. This is affected by factors such as solar variation and emission of climate gases.

The topic of this thesis is to develop efficient statistical methodology to obtain Bayesian inference for global and local climatic time series data. This is achieved using the general hierarchical modeling framework of latent Gaussian models (IGMs). Bayesian analysis can be performed efficiently using the methodology of integrated nested Laplace approximation (INLA), utilising the sparse structure of the precision, inverse covariance, matrix of the latent Gaussian field. Obtaining inference for LRD processes using INLA is inefficient on account of their precision matrix being dense. For an $n \times n$ matrix essential matrix operations such as Cholesky factorization generally require $\mathcal{O}(n^3)$ floating point operations to perform.

Paper I demonstrates how stationary Gaussian LRD processes with memory governed by a single-parameter can be approximated using a mixture of only four first-order autoregressive (AR) processes. This approximation ensures that the LRD model retains conditional independence and that inference can be obtained efficiently. The accuracy of this approach is remarkable and the computational benefits are excellent, allowing inference to be obtained by INLA in linear time and memory.

Paper II details how this methodology can be used to design a Bayesian model for global mean surface temperature (GMST) that reflects climate dynamics by incorporating radiative forcing data. This model has been made available as part of the R-package `INLA.climate`, and is used to estimate the transient climate response and to predict temperature response to future forcing scenarios. Paper III uses the GMST model to estimate equilibrium climate sensitivity, and paper IV applies the same methodology to gridded local time series from the GISS Surface Temperature Analysis spatio-temporal data set.

Acknowledgements

I would like to thank the Department of Mathematics and Statistics for giving me the opportunity to do a PhD. This has been a very enriching experience.

Most of all I would like to thank my main supervisor Sigrunn whom has been providing excellent guidance and supervision throughout my PhD. I would also like to thank my co-supervisor Martin for helping me grasp climate science, and my co-supervisor Håvard for all the help regarding INLA.

I am also grateful for all the friends and colleagues I've met through my PhD as a PhD candidate, both here at UiT as well as those I've through my work in SiN and TODOS. In particular I would like to thank Øistein for creating the template that I have used to write my dissertation.

Last, but not least I would like to thank Maria, my friends and my family for all the support the last few years.

Contents

Abstract	iii
Acknowledgements	v
Chapter 1. Introduction	1
1.1. Thesis outline	3
1.2. List of publications	4
Chapter 2. Theoretical background	5
2.1. Long-range dependence	5
2.2. Incorporating LRD in a flexible modeling framework	9
Chapter 3. Approximating long memory by aggregating short memory processes	15
3.1. Achieving sparsity by introducing a Markovian approximation	15
3.2. Simulation based aggregation	16
3.3. Numerical based aggregation	17
3.4. Selecting optimization parameters	18
3.5. Support in R-INLA	20
Chapter 4. Applications in climate science	27
4.1. Modeling global mean surface temperature	27
4.2. Statistical model	29
4.3. Temperature predictions	30
4.4. Climate sensitivity measures	32
4.5. Local temperature data	34
4.6. Future work: Spatio-temporal modeling	36
Chapter 5. Concluding remarks	41
Appendix A. The <code>INLA.climate</code> package	43
A.1. Installation	43
A.2. How to use the package	44
A.3. Troubleshooting	48
Bibliography	51

Paper I	61
Paper II	77
Paper III	107
Paper IV	125

CHAPTER 1

Introduction

The main aim of this project is to develop efficient statistical methodology to analyse climatic time series, including both global mean surface temperature (GMST) and local temperature data. These have both been observed to exhibit persistent correlation structure known as long-range dependence (LRD) (Rypdal et al., 2013). The concept of LRD implies that correlation follows a power-law decay and that observations far apart in time or space are still significantly correlated. LRD is found to describe behaviour found in many different fields of research, see e.g. Beran (1994) and Beran et al. (2013) for various examples of analysing LRD. Specifically, we will use a fractional Gaussian noise (fGn) (Mandelbrot and van Ness, 1968) model component to describe LRD in climatic data.

Climatic time series are widely known to be affected by radiative forcing. This is the net amount of the sun's radiation to be absorbed by the earth and is influenced by factors such as volcanic activity and greenhouse gases. The contribution to radiative forcing from some of these factors can be determined using proxy data from e.g. corals, tree rings and ocean sediments. To reflect real climate dynamics the temperature change associated with these forcing contributions should be accounted for in our model. Rypdal et al. (2013) argue that global temperature can be described as a scale-invariant response to radiative forcing for time scales that apply to all data analysed in this project. The same persistent behaviour has also been observed for local temperature time series data (Løvsletten and Rypdal, 2016). The temperature variation that is not explained from known radiative forcing is assumed to be described by an fGn.

Using a Bayesian statistical framework is beneficial in that it allows for prior information about model parameters and variables to be incorporated in the form of prior distributions. This improves reliability as uncertainty in the assumed probability model is accounted for. Existing methods of performing Bayesian analysis of time series with LRD properties include Graves et al. (2015) and Makarava et al. (2011). For this project we propose to perform Bayesian analysis by formulating a latent Gaussian model. Latent Gaussian models represent a unified computational framework to perform Bayesian analysis of a wide range of statistical models. Specifically,

this framework defines a three-stage hierarchical model in which underlying temporal and spatial dependency structure of observed data is modelled in terms of a latent Gaussian field. The variability and structure of the latent field is governed by hyperparameters. Traditionally, the most commonly used approach to analyse such models is Markov chain Monte Carlo (MCMC) methods, see e.g. Gamerman and Lopes (2006) and Robert and Casella (1999). Although such methods are general and flexible they are often very time-consuming. Rue et al. (2009) present a computationally superior alternative, namely the methodology of integrated nested Laplace approximations (INLA). This is available as the R package `R-INLA`, which can be downloaded for free at www.r-inla.org. Since its introduction, this method has become a widespread tool applied to a wide range of different scientific fields. Instead of relying on simulations INLA computes the posterior marginal distributions for all model parameters directly by using numerical approximations and integration. A key assumption is that the inverse covariance matrix of the latent Gaussian field is sparse. However, LRD processes such as fGn are inherently unsuited for such algorithms as they are characterised by having a dense inverse covariance matrix.

For stationary Gaussian LRD processes where the memory structure is expressed by a single parameter, we introduce an accurate and computationally efficient approximation in terms of a weighted sum of first order autoregressive (AR) processes. We find that by using only four AR(1) processes we obtain an aggregate process with autocorrelation function almost identical to that of the LRD process we wish to approximate. This allows for accurate Bayesian inference to be obtained in linear time and memory consumption using INLA. Support within the R-INLA framework is advantageous in that the LRD latent model component can easily be incorporated into more complex models with other fixed and random effects such as linear responses or seasonal variations.

By employing this approximation within R-INLA, we provide a computationally efficient modeling framework for analysing the GMST in terms of radiative forcing. The model is available in the R-package `INLA.climate`, which provides a user-friendly interface for our developed methodology, making it accessible also for applied climate scientists. This package has been used to estimate the climate sensitivity measures known as transient climate response (TCR), defined as the temperature increase following a gradual CO₂-doubling, and the equilibrium climate sensitivity (ECS), defined as the temperature increase following an immediate and sustained CO₂-doubling. Whereas advanced Earth System Models (ESMs) require a substantial runtime in order to provide these estimates, our approach can obtain Bayesian inference in seconds. Furthermore, it can also be applied to general data sets that are not produced by simulating ESMs. This approach

can also be easily adopted to perform temperature predictions by expressing the future temperature as a response to some known future forcing scenario. Specifically, we have used the Representative Concentration Pathway trajectories to describe the future forcing. This modeling framework has also been used to analyse local data independently. Here, we also include a linear trend which is found to be significant for 84% of local time series, indicating a temperature increase for the majority of Earth’s surface.

1.1 Thesis outline

Chapter 2 provides theoretical background and introduces the concept of long-range dependence along with the two most commonly applied LRD processes. This chapter also presents the framework of latent Gaussian modeling and applies this methodology to a real data example and explains how incorporating LRD into such a framework is problematic.

Chapter 3 summarises the first paper of this thesis and explains how approximating LRD in terms of a weighted sum of short-range dependent processes resolves the computational issues associated with LRD. This chapter presents such an approximation by adopting a mixture of AR(1) processes with weights and first-lag autocorrelation parameters selected using numerical optimization. Further discussion not included in the paper regarding choosing the quantities of the optimization procedure and how the accuracy of the approximation is affected is also included.

Chapter 4 elaborates on adopting the AR(1) mixture approximation to form a realistic model for climatic data which incorporates data on radiative forcing as described in paper II. This chapter also covers the various climate applications of our model that we have studied during this project. This includes temperature prediction, estimation of the transient climate response (TCR) and equilibrium climate sensitivity (ECS), as well as trend testing of local data. Brief summaries of papers II–IV are also included.

Chapter 5 provides concluding remarks, followed by the four papers included in this thesis, of which three have been published.

Appendix A includes a description and tutorial of the `inla.climate` package.

1.2 List of publications

Paper I

Sørbye, S. H., E. Myrvoll-Nilsen and H. Rue (2019), **An approximate fractional Gaussian noise model with $\mathcal{O}(n)$ computational cost**, *Statistics and Computing*, **29**, 821–833, doi:0.1007/s11222-018-9843-1.

Paper II

Myrvoll-Nilsen, E., S. H. Sørbye, H.-B. Fredriksen, H. Rue and M. Rypdal, **Statistical estimation of global surface temperature response to forcing under the assumption of temporal scaling**, submitted to *Earth System Dynamics*.

Paper III

Rypdal, M., H.-B. Fredriksen, E. Myrvoll-Nilsen, K. Rypdal and S. H. Sørbye (2018), **Emergent Scale Invariance and Climate Sensitivity**, *Climate*, **6** (93), doi:10.3390/cli6040093.

Paper IV

Myrvoll-Nilsen, E., H.-B. Fredriksen, S. H. Sørbye and M. Rypdal (2019), **Warming trends and long-range dependent climate variability since year 1900: a Bayesian approach**, *Frontiers in Earth Science*, **7**, doi: 10.3389/feart.2019.00214.

CHAPTER 2

Theoretical background

2.1 Long-range dependence

Long-range dependence (LRD) or long memory is a property relating to the rate of decay of statistical dependence of two observations as the temporal or spatial distance between them increases. For long memory processes the autocorrelation function (acf) typically follows a power-law decay. Conversely, the acf of short-range dependent (SRD) processes exhibit an exponential decay. Although numerous competing mathematical definitions of LRD have emerged over the years (Guegán, 2005), the long memory property is often defined by the behaviour of the covariance between two variables as the temporal distance between them increases. In this thesis we have only studied stationary LRD processes and as such we define long memory by the asymptotic behaviour of the acf, denoted ρ . Specifically, the stationary stochastic process $\{x_t\}$ is said to exhibit LRD if

$$\lim_{k \rightarrow \infty} \rho(k) = c k^{2H-2},$$

where $c > 0$ is a constant and $H \in (0.5, 1)$ is the memory parameter known as the *Hurst exponent* or *Hurst parameter*. For non-stationary processes, a prevalent alternative definition is to define LRD as when the sum of the covariance at each lag diverges towards infinity, i.e.

$$\sum_{k=-\infty}^{\infty} \text{Cov}(x_t, x_{t+k}) = \infty.$$

Both of these definitions have equivalent definitions in the spectral domain. Long memory has been used to describe behaviour found in many different fields such as econometrics (Baillie, 1996; Diebold and Inoue, 2001), climate science (Franzke, 2012; Koutsoyiannis, 2003) and dendrochronology (Baillie and Chung, 2002). One of the most important contributions on this topic is a study performed by Hurst (1951) on the fluctuations of the water level in the Nile river. To measure the variability of the time series Hurst developed the rescaled range statistic, denoted $(R/S)_t$ for some time point t . For observations $\mathbf{y} = (y_1, \dots, y_n)^\top$, define $\mathbf{z} = (z_1, \dots, z_n)^\top$ and

$\mathbf{u} = (u_1, \dots, u_n)^\top$ by

$$z_t = \sum_{i=1}^t (y_i - \mathbb{E}[y_i]) \quad \text{and} \quad u_t = \frac{1}{t} \sum_{i=1}^t y_i.$$

The rescaled range statistic is then defined as

$$(R/S)_t = \mathbb{E} \left[\frac{R(t)}{S(t)} \right] = \mathbb{E} \left[\frac{\max(z_1, \dots, z_t) - \min(z_1, \dots, z_t)}{\sqrt{\frac{1}{t} \sum_{i=1}^t (y_i - u_t)^2}} \right].$$

This statistic provides an assessment of how the variability of a time series changes with the length of the time-period being considered. For large t , Hurst observed that $(R/S)_t \propto t^H$, where $H \approx 0.72$. This implies that the variability is expected to increase according to a power-law of order H . In hydrology, this describes the tendency of dry years to cluster together to form periods of drought, and conversely for wet years to cluster and form wet periods. This behaviour has since also been called the Joseph effect (Mandelbrot and Wallis, 1968), referring to the biblical story of Joseph, whom predicted seven years of great abundance to be followed by seven years of famine.

This behaviour had been studied before, see e.g. Kolmogorov (1941), but Hurst was able to show that this phenomenon could not be explained using contemporary hydrological models. Specifically, he showed that for independent identically distributed (iid) Gaussian models the $(R/S)_t$ statistic should exhibit growth proportional to $t^{1/2}$ as $t \rightarrow \infty$. This was later proven mathematically to hold for standardized iid random variables with finite variance, with contributions from e.g. Feller (1951). Hurst's result lead to substantially more interest on the topic, which is why both the Hurst exponent H as well as the behaviour expressed when $H > 1/2$, since referred to as the *Hurst phenomenon*, is named after him. This phenomenon puzzled both hydrologists and mathematicians, whom for years tried to create a model that could successfully reproduce it.

It should be noted that, although similar to the concept of long memory, the Hurst phenomenon is not synonymous with it, see e.g. Franzke et al. (2015) or Bhattacharya et al. (1983). However, the rescaled range statistic remains a useful method for identifying the Hurst exponent of an observed time series suspected of exhibiting LRD. Moreover, research motivated by explaining the Hurst phenomenon lead to major breakthroughs in developing models that capture LRD, including those we have employed in this thesis. For an overview of the discussion and research that followed the Hurst study see e.g. Graves et al. (2017).

2.1.1 Fractional Gaussian noise

Fractional Brownian motion (fBm) was first introduced by Kolmogorov (1940). However, it was not until the seminal paper by Mandelbrot and van Ness (1968) where the relevance of fBm in explaining the Hurst phenomenon was first recognized, see e.g. Taqqu (2013) for a review. It was also in this paper where the process received its name and where many of its useful properties were derived. Fractional Brownian motion is a continuous stochastic process defined by the stochastic integral

$$B_H(t) = B_H(0) + \frac{1}{\Gamma(H + 1/2)} \left(\int_{-\infty}^0 \left((t-s)^{H-1/2} - (-s)^{H-1/2} \right) dB(s) + \int_0^t (t-s)^{H-1/2} dB(s) \right),$$

where B is a regular Brownian motion process, Γ is the gamma function and $H \in (0, 1)$ is the Hurst exponent. This process is a generalization of a Brownian motion that exhibits long-range dependency. The behaviour of the fBm can be categorized in three different cases. If $0.5 < H < 1$ the fBm exhibits long-range dependence and positive correlation. If $H = 0.5$ the fBm is memory-less and reduces to a regular Brownian motion. If $0 < H < 0.5$ the fBm exhibits anti-persistence and is negatively correlated. The fBm is also self-similar (also referred to as self-affine), which is another property introduced in Mandelbrot and van Ness (1968). This means that if we let B_H denote an fBm with Hurst exponent H and let c be an arbitrary real number, then

$$B_H(ct) = c^H B_H(t).$$

In fact, fractional Brownian motion is the only self-similar Gaussian process with stationary increments

$$\varepsilon_H(t) = B_H(t+1) - B_H(t),$$

see e.g. Tudor (2013) for proof. These increments form another LRD process called fractional Gaussian noise (fGn) which also possess several important properties. One of the most significant findings of Mandelbrot and van Ness (1968) was that the rescaled range of the fGn was proportional to t^H as $t \rightarrow \infty$. Mandelbrot and van Ness had thus been able to construct a stationary Gaussian process which reproduced the Hurst phenomenon. Furthermore, the fGn also fulfills the criterion for defining LRD in stationary processes. This can be seen by inspecting the acf of an fGn

$$\rho(k) = \frac{1}{2} (|k-1|^{2H} - 2|k|^{2H} + |k+1|^{2H}), \quad (2.1)$$

which follows $\rho(k) \approx H(2H - 1)|k|^{2(H-1)}$ for large lags k . Similar to the fBm, the fGn is long-range dependent when $0.5 < H < 1$, anti-persistent if $0 < H < 0.5$ and memoryless if $H = 0.5$. Only fGn processes with Hurst exponents in the persistent range $H \in (0.5, 1)$ will be considered in this project.

A nice property of fGn processes is that since it is defined as the increment of the self-similar fBm many asymptotic relations hold also for finite sample sizes (Taqqu et al., 1995). FGn has also enjoyed popularity due to its analytic tractability (Purczyński and Włodarski, 2006). In some situations, the parsimony of the fGn can be considered a flaw as it is not as flexible as other LRD processes that has been introduced since. Most notable of these is the class of autoregressive fractionally integrated moving average (ARFIMA) processes which can incorporate both LRD and SRD. Nevertheless, the fGn holds historical importance as being the first LRD process to successfully describe the Hurst phenomenon.

2.1.2 Autoregressive fractionally integrated moving averages

Fractional Gaussian noise is essentially a discrete approximation of a fractional derivative of Brownian motion. Hosking (1981) proposed to discretise first, then perform fractionally differencing. This was partly based on an idea presented by Granger (1978) whom later developed the theory independently (Granger and Joyeux, 1980). These contributions lead to the the ARFIMA class of models. In short, the ARFIMA models are an extension of ARIMA(p, d, q)

$$\phi(B)^p(1 - B)^d x_t = \theta(B)^q \varepsilon_t,$$

where B denotes the backshift operator $Bx_t = x_{t-1}$, and $\phi(B)^p$ and $\theta(B)^q$ describes the backshift polynomial corresponding to the AR(p) component and the MA(q) component, respectively. ARFIMA(p, d, q) models allow d to be a non-integer number. This change has interesting consequences for the covariance structure. Consider first the case of ARFIMA($0, d, 0$) also known as a fractionally integrated (FI) process

$$x_t = (1 - B)^{-d} \varepsilon_t.$$

Using Taylor expansions this can be interpreted as a moving average process

$$x_t = \sum_{s=0}^{\infty} \frac{\Gamma(s + d)}{\Gamma(d)\Gamma(s + 1)} \varepsilon_{t-s},$$

where $0 < d < 1/2$. Granger and Morris (1976) show that this process has acf

$$\rho(k) = \frac{\Gamma(1 - d)}{\Gamma(d)} \frac{\Gamma(k + d)}{\Gamma(k + 1 - d)}.$$

Using Sterling’s theorem the acf can, for large k , be approximated by $\rho(k) \approx Ck^{2d-1}$, where C is an appropriate constant. For $d > 0$, the acf has an asymptotic hyperbolic decay and thus satisfies the criterion for long range dependence. For $d < 0$, the process exhibits negative correlation. The ARFIMA(0, d , 0) has very similar properties as an fGn with Hurst exponent $H = d + 1/2$. They both exhibit long-range dependency explained parsimoniously by a single parameter and their acfs exhibit similar asymptotic behaviour. The ARFIMA(p , d , q) process is both stationary and invertible for $-1/2 < d < 1/2$, however, only ARFIMA(0, d , 0) processes which exhibit long memory, i.e. $0 < d < 1/2$ will be considered in this thesis.

A notable advantage of the ARFIMA(0, d , 0) model is its flexibility as it is a case of the more general class of ARFIMA(p , d , q) models thus allowing the Box–Jenkins method (Box et al., 2016) to be applied. The ARFIMA(0, d , 0) model also has a very simple spectral density function (Taqqu et al., 1995)

$$f(\lambda) = \frac{1}{2\pi} \left(2 \sin \frac{\lambda}{2} \right)^{-2d} \sim \frac{1}{2\pi} |\lambda|^{-2d} \quad \text{as } \lambda \rightarrow 0,$$

where λ is the frequency. The re-scaled partial-sums ARFIMA(0, d , 0) model converges in distribution to fBm (Taqqu, 2003) and thus exhibits self-similarity asymptotically. However, introducing non-zero p or q will destroy this property.

Although other LRD processes exist, see e.g. the broken-line process of Rodriguez-Iturbe et al. (1972), the fGn and ARFIMA models are by far the most widely used. While the ARFIMA models are preferred in most scientific fields, fGn seems to be the most used model in physics (Graves et al., 2017). As this thesis focuses on problems in climate science, much of the methodology developed here will therefore be presented with the fGn in mind. However, all methods developed for the fGn can just as easily be adopted for the ARFIMA(0, d , 0) model.

2.2 Incorporating LRD in a flexible modeling framework

Inference about LRD processes primarily includes estimating the Hurst exponent H , and over the years various methods to estimate this parameter have been developed. Popular methods include the aforementioned rescaled range analysis (Hurst, 1951), detrended fluctuation analysis (Peng et al., 1994) and Whittle’s estimator (Whittle, 1951). Bayesian methods include approximating the likelihood which is incorporated into a Markov chain Monte Carlo approach (Graves et al., 2015), and estimating H in terms of linear mixed models (Makarava et al., 2011).

2.2.1 Latent Gaussian modeling

Fractional Gaussian noise and ARFIMA(0, d , 0) do not enjoy the same flexibility as the general ARFIMA(p , d , q) models which can incorporate both short and long memory in the same model. Real data, and many of the cases considered in this thesis, cannot always be explained by a single LRD component. Therefore, we introduce fGn as a latent model component in the existing framework of latent Gaussian models (LGms), a subclass of structured additive regression models. This is a hierarchical Bayesian model where the mean of the observation variable y_i is linked to a structured additive predictor η_i through a link function g such that $g(\mathbb{E}[y_i]) = \eta_i$. The predictor expresses the effects of various covariates

$$\eta_i = \beta_0 + \sum_{k=1}^{n_\beta} \beta_k z_{i,k} + \sum_{j=1}^{n_f} f^{(j)}(\mathbf{u}_{j,i}) + \epsilon_i.$$

Here ϵ_i is an unstructured noise term, β_0 is an intercept term and $\{\beta_k\}$ are linear effects of covariates $\mathbf{z}_i = (z_{i,1}, \dots, z_{i,n_\beta})^\top$. The unknown functions $\{f^{(j)}\}$ are called *random effects*. These functions can take on very different forms which enable many different applications. For latent Gaussian models $\beta_0, \{\beta_k\}, \{f^{(j)}\}, \{\epsilon_i\}$ are all assigned Gaussian priors. For the random effects, however, this prior may depend on a set of hyperparameters, denoted $\boldsymbol{\theta}_2$. Let the latent field $\mathbf{x} = (x_1, \dots, x_{n_x})^\top$ denote the vector containing the additive predictor and all stochastic terms therein $\mathbf{x} = (\boldsymbol{\eta}, \beta_0, \{\beta_k\}, \{f^{(j)}\}, \boldsymbol{\epsilon})^\top$. This is a multivariate Gaussian random field which explains the temporal and spatial dependency structure of all stochastic terms in the predictor.

Formally, the latent Gaussian model formulation is defined in three stages. The first stage specifies the likelihood of the observations. Let $\boldsymbol{\theta}_1$ denote the vector of parameters, if any, of the likelihood distribution and $\boldsymbol{\theta} = (\boldsymbol{\theta}_1^\top, \boldsymbol{\theta}_2^\top)^\top = (\theta_1, \dots, \theta_{n_\theta})^\top$ denote all model parameters. We assume the observations to be conditionally independent given the latent field \mathbf{x} and parameters $\boldsymbol{\theta}$, i.e.

$$\pi(\mathbf{y} \mid \mathbf{x}, \boldsymbol{\theta}) = \prod_{i=1}^n \pi(y_i \mid x_i, \boldsymbol{\theta}_1).$$

The second stage specifies the prior distribution for the latent Gaussian field \mathbf{x} given a set of hyperparameters $\boldsymbol{\theta}_2$. For LGms this is a multivariate Gaussian distribution

$$\mathbf{x} \mid \boldsymbol{\theta}_2 \sim \mathcal{N}(\boldsymbol{\mu}, \mathbf{Q}^{-1})$$

where $\boldsymbol{\mu} = \mathbb{E}[\mathbf{x} \mid \boldsymbol{\theta}]$ and precision matrix, defined as the inverse covariance matrix, $\mathbf{Q} = \boldsymbol{\Sigma}^{-1}$.

The final stage specifies the joint prior distribution for the hyperparameters $\pi(\boldsymbol{\theta}_2)$ that specify the form of \mathbf{x} . This distribution is typically formed by assigning a prior to each of the m hyperparameters independently,

$$\pi(\boldsymbol{\theta}_2) = \prod_{i=1}^m \pi(\theta_i).$$

For transparent prior selection we have adopted penalised complexity (PC) priors (Simpson et al., 2017) to our hyperparameters. This is a recently developed class of priors which are based on specific principles that emphasize simplicity. These are governed by two fixed parameters u and α . For an alternative to PC priors which allows the prior to be assigned jointly, see the hierarchical decomposition prior (Fuglstad et al., 2019).

The class of IGM presents a unified framework to analyse a wide range of statistical models and allows us to obtain full Bayesian inference. This implies a complete description of the joint and marginal posterior distributions for the hyperparameters and latent variables. The joint posterior distribution for all components and hyperparameters is obtained by taking the product of the likelihood and the prior distributions

$$\pi(\mathbf{x}, \boldsymbol{\theta}) \propto \pi(\mathbf{y} \mid \mathbf{x}, \boldsymbol{\theta}_1) \pi(\mathbf{x} \mid \boldsymbol{\theta}_2) \pi(\boldsymbol{\theta}).$$

2.2.2 Computation using R-INLA

For latent Gaussian models, the marginal posterior densities $\pi(x_i \mid \mathbf{y})$ and $\pi(\theta_i \mid \mathbf{y})$ can be obtained by using integrated nested Laplace approximation (INLA). INLA is implemented for R as the package R-INLA package which can be downloaded for free at www.r-inla.org. INLA utilises efficient numerical algorithms for sparse matrices to achieve fast approximate Bayesian analysis. However, if the precision matrix of \mathbf{x} is dense, the computational advantage is lost. Applying INLA on LRD processes such as the fGn is therefore inefficient, on account of their long-range dependent memory structure which implies dense precision matrices. This has consequences for computational efficiency and memory usage, in particular for longer time series.

As an fGn model component is not included in the R-INLA package, we specify it manually using `rgeneric`. This is a custom modeling framework that allows the user to define generic latent model components for INLA. This freedom comes at a computational cost as the `rgeneric` model component needs to be interpreted in R which will make it run slower than the built-in model components which are implemented for INLA in C.

The `rgeneric` implementation requires the specification of the precision matrix and its determinant. This requires inverting the covariance matrix which is dense and therefore very costly to perform. Typically, matrix inversion of an $n \times n$ -matrix require $\mathcal{O}(n^3)$ floating points operations (flops)

to perform. However, this can be reduced by taking advantage of the Toeplitz form of the covariance matrix of an fGn. By applying Trench inversion (Trench, 1964; Golub and Loan, 1996) and the Levinson-Durbin algorithm (Durbin, 1960; Levinson, 1947) we obtain the precision matrix and its determinant in $\mathcal{O}(n^2)$ flops. Under certain circumstances however, such as when fGn is observed indirectly with inhomogenous noise, the precision matrix will no longer be Toeplitz and the cost returns to $\mathcal{O}(n^3)$ flops. For the patient user, however, memory might be the more limiting resource. In fact, when testing this approach for a simulated time series of length $n = 2,500$ with my personal computer, a MacBook Pro (mid-2015) with 16GB RAM, INLA crashed due to reaching the computer’s memory limit.

2.2.3 Example: Fitting an lGm to the NileMin data

To illustrate the procedure I will apply the lGm framework to the $n = 663$ NileMin data set given by Tousson (1925), available in the R-package `longmemo`. This is a popular data set for LRD analysis, see e.g. Beran (1994), that describes the annual water level minima measured at the Roda gauge near Cairo for the period 622–1284. We will assume the observations $\mathbf{y} = (y_1, \dots, y_n)^\top$ to be a realisation of a zero-mean fGn, although the same procedure can be carried out similarly for an ARFIMA(0, d , 0) process. We will estimate both the Hurst exponent and the standard deviation, denoted $\boldsymbol{\theta} = (H, \sigma)$, by computing the posterior marginal distributions for each of them. To properly incorporate the long memory structure of the fractional Gaussian noise it is expressed as a random effect instead of a noise term. Using an identity link function the predictor is expressed as

$$\eta_i = f(\mathbf{u}_i) = \varepsilon_i$$

where we have denoted the fGn term by $\boldsymbol{\varepsilon} = (\varepsilon_1, \dots, \varepsilon_n)^\top$. We assume that there is no uncertainty not explained by the predictor and therefore choose to assign a Gaussian likelihood with negligible fixed variance $\sigma_y^2 \approx 0$ and mean η_i . There are hence no unknown parameters associated with the likelihood. This concludes the first stage of defining the lGm. For the second stage the latent Gaussian field is specified. The mean vector of which is assumed to be zero for all variables, and the precision matrix is obtained by inverting the autocovariance matrix formed by equation (2.1). For the last stage, we assign penalised complexity priors for the marginal prior distributions for the hyperparameters. For scaling hyperparameters such as the precision $\kappa = 1/\sigma^2$ the PC prior is computed to be equal to the exponential distribution. The PC prior for the Hurst exponent H is computed numerically as instructed in Sørbye and Rue (2017). Here, we use prior parameters $u_\kappa = 1$ and $\alpha_\kappa = 0.01$ for κ , and $u_H = 0.9$ and $\alpha_H = 0.1$ for H .

Utilizing the Toeplitz form of the precision matrix, INLA converges in around two minutes. Methods such as Whittle’s approximate maximum likelihood estimate and rescaled range analysis produce similar results, but are computed almost instantaneously. Although neither time consumption nor memory usage is an issue for this particular demonstration, more computationally challenging problems with either more observations, hyperparameters or replications might prove infeasible to perform.

Approximating long memory by aggregating short memory processes

This chapter will describe how Bayesian inference for IGms with an LRD latent model component can be obtained efficiently by introducing an approximate Gaussian random field with a high degree of conditional independence. This is obtained using numerical optimization such that the resulting acf matches the theoretical acf of the target LRD process. The research presented in Sørbye et al. (2019) will be summarised, and alternative specifications of the numerical optimization procedure and their impact on speed and accuracy will be discussed.

3.1 Achieving sparsity by introducing a Markovian approximation

Let $\mathbf{x} = (x_1, \dots, x_n)^\top$ denote a multivariate Gaussian vector with mean $\boldsymbol{\mu}$ and precision matrix \mathbf{Q} ,

$$\mathbf{x} \sim \mathcal{N}(\boldsymbol{\mu}, \mathbf{Q}^{-1}),$$

Also, define $\mathbf{x}_{-ij} = (x_1, \dots, x_{i-1}, x_{i+1}, \dots, x_{j-1}, x_{j+1}, \dots, x_n)^\top$. If the Gaussian variables x_i and x_j are conditionally independent given \mathbf{x}_{-ij} , i.e.

$$\pi(x_i, x_j \mid \mathbf{x}_{-ij}) = \pi(x_i \mid \mathbf{x}_{-ij})\pi(x_j \mid \mathbf{x}_{-ij}),$$

then the corresponding term in the precision matrix, Q_{ij} , is zero, see e.g. theorem 2.2 in Rue and Held (2005) for proof. This reflects the Markov property, and a Gaussian random field (GRF) that possesses a high degree of conditional independence is known as a Gaussian Markov random field (GMRF). This implies a sparse precision matrix which allows for many computationally efficient algorithms central to the INLA approach to be employed. Most notably this includes computing the Cholesky factorization $\mathbf{Q} = LL^\top$, where L is a lower triangular matrix. Hence, introducing a GMRF that successfully approximates the latent Gaussian field \mathbf{x} would resolve the computational issues associated with LRD.

This is achieved by forming an aggregate process $\tilde{\mathbf{x}}_m = (\tilde{x}_1, \dots, \tilde{x}_m)^\top$ defined as a weighted sum of m independent AR(1) processes. Let $\{\mathbf{x}_i\}$

denote a set of m independent AR(1) processes of equal length n ,

$$x_{i,t} = \phi_i x_{i,t-1} + \varepsilon_{i,t}, \quad i = 1, \dots, m, \quad t = 1, \dots, n, \quad (3.1)$$

where each ϕ_i are distinct and $\varepsilon_{i,t}$ are iid zero mean Gaussian processes independent of ϕ_i . The aggregate process is given by

$$\tilde{\mathbf{x}}_m = \sigma \sum_{i=1}^m \sqrt{w_i} \mathbf{x}_i + \omega. \quad (3.2)$$

Here, σ denotes the standard deviation of the aggregate process, $\{w_i\}$ denote the individual weights and ω is a noise term with small variance in the $\exp(-15)$ range added to ensure that the precision matrix is positive definite. The complete latent field is defined as

$$\mathbf{x} = (\boldsymbol{\eta}, \tilde{\mathbf{x}}_m, \mathbf{x}_1, \dots, \mathbf{x}_m)^\top.$$

By expanding the joint density

$$\pi(\mathbf{x}_1, \dots, \mathbf{x}_m, \tilde{\mathbf{x}}_m \mid \boldsymbol{\theta}) = \pi(\mathbf{x}_1 \mid \boldsymbol{\theta}) \cdots \pi(\mathbf{x}_m \mid \boldsymbol{\theta}) \pi(\tilde{\mathbf{x}}_m \mid \mathbf{x}_1, \dots, \mathbf{x}_m, \boldsymbol{\theta}),$$

we find that temporal conditional dependence is only present within the underlying AR(1) components and not in $\tilde{\mathbf{x}}$ (Sørbye et al., 2019). Since these processes all possess the Markov property, the complete latent field \mathbf{x} is also a GMRF. By rearranging the variables in \mathbf{x} the resulting precision matrix is a sparse matrix with bandwidth $b = m + 1$. The number of flops is $db^2 = n(m + 1)^3$ and the memory requirement is $d(b + 1) = n(m + 1)(m + 2)$ reals. See e.g. Golub and Loan (1996) sec. 4.3.5 for proof. This ensures great computational benefits assuming m is of order $\mathcal{O}(1)$, which allows the log-likelihood to be evaluated quickly (Rue, 2001) and for INLA to obtain full Bayesian inference in linear time and memory.

3.2 Simulation based aggregation

Let $\{\mathbf{x}_i\}$ denote m individual AR(1) processes of length n as given by equation (3.1). According to Granger and Morris (1976) the sum of m such AR(1) processes can generate an aggregated process $\tilde{\mathbf{x}}_m$ equivalent to an ARMA($m, m - 1$) process, i.e.

$$\tilde{\mathbf{x}}_m = \sum_{i=1}^m \frac{1}{m} \mathbf{x}_i \sim \text{ARMA}(m, m - 1).$$

This result shows that it is possible to create an aggregated process with a correlation structure decreasing more slowly than for the components used to construct it. In fact, it is even possible to apply such an approach to create an aggregated process that exhibit LRD, as proven in Granger (1980). Let the first-lag autocorrelation parameters $\{\phi_i\}$ of equation (3.1) be sampled from a Beta distribution with shape parameter p and scale

parameter q , $\phi_i \sim \mathcal{B}(p, q)$. Then, as $m \rightarrow \infty$, the sum of AR(1) processes $\tilde{\mathbf{x}}_m$ will exhibit long memory. Specifically, $\tilde{\mathbf{x}}_m$ follows an ARFIMA(0, d , 0) process with parameter $d = 1 - q/2$.

In theory, it should therefore be possible to recreate any fractionally integrated process with Hurst exponent $H = d - 1/2$ by sampling $\phi_i \sim \mathcal{B}(p, 3 - 2H)$ for an arbitrary p and aggregate each simulated AR(1) series. However, this turns out to be ineffective in practice. Haldrup and Valdés (2017) show that even when using $m = n$ AR(1) components the ability of the aggregate process to recreate LRD was still inadequate. Since the computational cost of INLA would increase immensely if m is of order $\mathcal{O}(n)$, the potential gain in computational efficiency by adopting an AR(1) mixture representation is lost. It is therefore clear that forming AR(1) aggregations by randomly sampling their first-lag autocorrelation coefficients is an impractical approach.

3.3 Numerical based aggregation

We propose to form the aggregation as a weighted sum of m AR(1) processes, where the weights $\mathbf{w} = (w_1, \dots, w_m)^\top$ and first-lag autocorrelation parameters $\boldsymbol{\phi} = (\phi_1, \dots, \phi_m)^\top$ are selected using a numerical optimization procedure. This is done such that the resulting AR(1) mixture $\tilde{\mathbf{x}}_m$, described by equation (3.2), best reproduces the target LRD process with memory parameter H (or $d = H - 1/2$ for ARFIMA(0, d , 0) processes) under a given criterion. The optimization is repeated for all H in a grid covering the persistent and stationary range of (0.5, 1) and interpolated in order to form a continuous mapping between H and the corresponding set of \mathbf{w} and $\boldsymbol{\phi}$. This mapping allows INLA to link the approximate LRD process with the underlying AR(1) processes and, by tuning H , find the set of $(\mathbf{w}, \boldsymbol{\phi})$ that gives the optimal fit. We will introduce a sum-to-one constraint on the weights, $\sum_{i=1}^m w_i = 1$. To improve mixing we require that $\phi_1 > \dots > \phi_m$. This is achieved by introducing the parametrisation

$$w_i = \frac{\exp(v_i)}{\sum_{j=1}^m \exp(v_j)} \quad \text{and} \quad \phi_i = \frac{1}{1 + \sum_{j=1}^i \exp(-u_j)},$$

where $v_1 = 1$. This also achieves a stable and unconstrained parameter space on $\mathbf{v} = (v_2, \dots, v_m)^\top \in \mathbb{R}^{m-1}$ and $\mathbf{u} = (u_1, \dots, u_m)^\top \in \mathbb{R}^m$. In Myrvoll-Nilsen (2016) the criterion for selecting \mathbf{w} and $\boldsymbol{\phi}$ was

$$(\mathbf{w}, \boldsymbol{\phi})_H = \underset{(\mathbf{w}, \boldsymbol{\phi})}{\operatorname{argmin}} (\hat{H}_{\text{avg}} - H)^2, \quad (3.3)$$

where \hat{H}_{avg} is the average of $R = 10$ maximum likelihood estimates of the Hurst exponent. This is obtained by applying the `FitFGN` function from the

since archived R-package FGN, to aggregations of m simulated AR(1) processes with individual weights w_i and first-lag autocorrelation parameter ϕ_i . To ensure that the parameter space of the optimization algorithm remained consistent it was imperative that the seed for the random number generator within each replication was equal and reset for each iteration of the optimization algorithm. Although the mapping generated using this optimization criterion was able to produce fast and reasonable estimates, it was still slightly inaccurate. The results were found to be biased, underestimating the Hurst exponent for processes with $0.5 < H < 0.75$ and overestimating for $0.75 < H < 1$. This bias might be explained by the low number of replications ($R = 10$) used to produce \hat{H}_{avg} , but increasing this would also further increase the computational cost of obtaining the mapping which was already very intensive.

In Sørbye et al. (2019) we improve upon this method by choosing another optimization criterion. Here, we select (\mathbf{w}, ϕ) such that the theoretical acf of the AR(1) mixture

$$\rho_{\bar{\mathbf{x}}_m}(k) = \sum_{i=1}^m w_i \phi_i^{|k|}, \quad k = 0, 1, \dots, n-1,$$

best matches that of an fGn with Hurst exponent H given in equation (2.1) truncated at some lag k_{max} . For each H , the associated numerical optimization problem is

$$(\mathbf{w}, \phi)_H = \underset{(\mathbf{w}, \phi)}{\operatorname{argmin}} \sum_{k=1}^{k_{\text{max}}} \psi(k) (\rho_{\bar{\mathbf{x}}_m}(k) - \rho_{\mathbf{x}}(k))^2, \quad (3.4)$$

using the same parametrisation as before. Since the smallest lags of the acf are very influential in identifying the Hurst exponent we introduce a lag-weight function ψ to emphasize the accuracy at these lags. The optimization problem is solved in R using the `optim` function, and to ensure continuity the initial value for the numerical scheme at each iteration is chosen to be equal to the optima located in the previous iteration. Since the optimization procedure struggles to find stable solutions at both ends of the interval $(0.5, 1)$ we choose to split it into two subintervals. The first starts at $H = 0.75$ and iterates towards $H = 0.5$, and the second starts at $H = 0.75$ and iterates towards $H = 1$. For $m = 4$, $k_{\text{max}} = 1000$ and $\psi(k) = 1/k$, this results in the mapping illustrated in figure 3.1.

3.4 Selecting optimization parameters

In solving equation (3.4), we need to first make choices for the quantities m , k_{max} and ψ . Choosing proper values for these settings is important to achieve good accuracy for different problems. Sørbye et al. (2019) explain

3.4 – Selecting optimization parameters

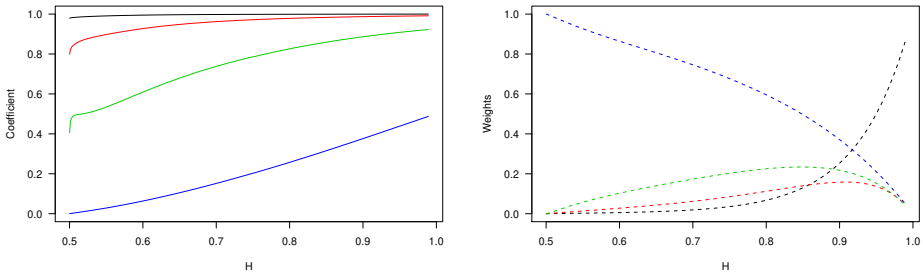


FIGURE 3.1. The mapping from H to the corresponding set of first-lag autocorrelation coefficients (left panel) and weights (right panel).

that choosing $m = 4$, $k_{\max} = 1000$ and $\psi(k) = 1/k$ provides a good approximation in most applications. As the paper does not detail why these specific settings were selected, I will use this opportunity to discuss the topic more in depth.

To illustrate how these quantities influence the accuracy I will perform separate analyses that estimate the Hurst exponent using the approximation obtained by equation (3.4) with different values of m , k_{\max} and ψ , and compare them with the estimate obtained using the exact model. The maximum likelihood of the Hurst exponent for fGn simulations will be estimated using the acf of the AR(1) mixture approximation with the given setting parameters. This is compared with the estimate obtained using the theoretical acf. The analyses will be repeated for 1000 fGn simulations of length $n = 1000$ and with Hurst exponent $H = 0.9$. This is because the differences in accuracy are more pronounced for high values of H . The quantities to be tuned include the number of AR(1) components $m \in \{3, 4, 5\}$, the number of lags for which the target acfs should be compared $k_{\max} \in \{500, 1000, 2000\}$ and the exponent $p \in \{0, 0.5, 1, 2\}$ of the lag-weight function assumed to take the form $\psi(k) = 1/k^p$ for $k \leq k_{\max}$.

As the runtime associated with the model component in equation (3.2) increases as more AR(1) components are incorporated we wish to pick the lowest possible m that yields sufficiently accurate estimates of H . Moreover, since we intend for this approximation to be created only once and applied for time series with different length and memory we also emphasize generality. We therefore pick p and k_{\max} such that the mixture properly recreates the characteristic early descent of the acf, while being able to retain accuracy for $k > k_{\max}$. A high k_{\max} allows the mixture to properly approximate longer time series, but will reduce the emphasis put on the small and mot

important lags as they constitute a smaller part of the acf compared to the overall size. Previously, we used $k_{\max} = 100$ and even for such low k_{\max} the optimization procedure failed to capture the characteristic acf structure without assigning a proper lag weight, ψ . Lag weight functions with high negative order p allows for acfs of higher k_{\max} to be compared without losing accuracy for the important smaller lags of the acf as is illustrated in figure 3.2. However, if p is too high, and thus too much weight is placed on the early lags, we observe that the accuracy is not properly maintained for $k > k_{\max}$. This is illustrated in figure 3.3. Scatter plots describing the correlation between the MLEs obtained using the approximate fGn and the exact fGn are illustrated in figures 3.4 to 3.6. We observe that for $m = 3$ the estimates are generally not sufficiently accurate, nor are the estimates obtained when using $\psi(k) = 1$. Based on the results we argue that selecting $m = 4$, $k_{\max} = 1000$ and $\psi(k) = 1/k$ is a good choice as this combination of quantities seem to generally provide good accuracy and appears to be a good trade-off between achieving accuracy for smaller and higher lags. Of course, other valid choices exist as well.

3.5 Support in R-INLA

Originally the approximate fGn model obtained using the link found in equation (3.4) was implemented for use in R-INLA using the `rgeneric` modeling framework. Doing so reduces the efficiency of INLA, especially if written entirely using R. The fGn model, with the recommended settings above, has since been implemented as a built-in latent model component in R-INLA called `fgn`. This makes the fGn model easily accessible and computationally more efficient as it has been written directly in the R-INLA C code. Moreover, a computational superior version of the fGn model is also available in R-INLA, known as `fgn2`. Here, the GMRF $\mathbf{x} = (\tilde{\mathbf{x}}_m^\top, \tilde{\mathbf{x}}_{m-1}^\top, \dots, \tilde{\mathbf{x}}_1^\top)^\top$ is structured differently and includes the cumulative sums of the m AR(1) processes

$$\tilde{\mathbf{x}}_k = \sum_{i=1}^k \sqrt{w_i} \mathbf{x}_i.$$

Whereas the standard fGn model expands the latent Gaussian field for an fGn of length n into a GMRF of length $(m+1)n$, the alternative approach expands into a GMRF of length mn . This will reduce the runtime, but will not allow for automatic source separation of the individual AR(1) processes. See the documentation within the R-INLA package for more information, accessible by the command `inla.doc("fgn")`.

Although the content of this section has been primarily focused on fGn, the approach for obtaining a similar approximation for other stationary and Gaussian single-parameter LRD processes, such as the ARFIMA(0, d , 0)

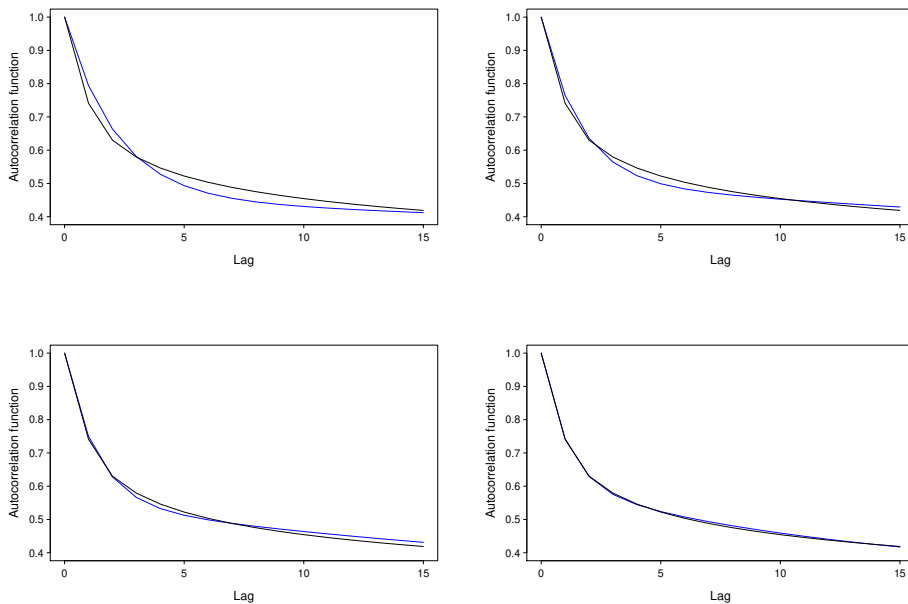


FIGURE 3.2. The acf of the $m = 3$ AR(1) mixture (blue) truncated at $k_{\max} = 1000$ against the theoretical acf an fGn (black) with $H = 0.9$. Panels 1–4 (top left to bottom right) show the acf corresponding to the approximate model using lag-weight $\psi(k) = k^{-p}$ with p equal to 0, 0.5, 1 and 2 respectively. We observe that as p increases fit in for the smaller lags improve.

model, is almost identical. The only difference is which target acf is used in the optimization procedure. However, as the ARFIMA(0, d , 0) model is currently not supported by R-INLA as a latent model component it has to be specified using `rgeneric`.

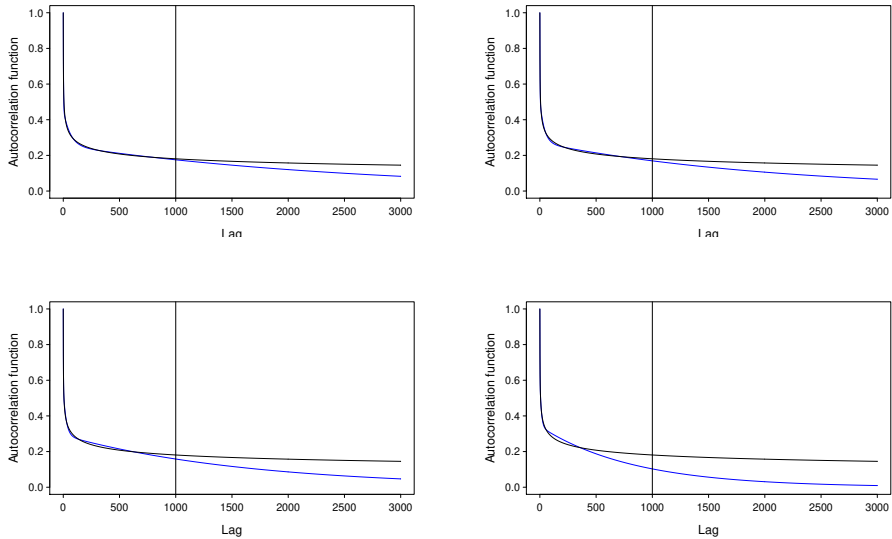


FIGURE 3.3. The acf of the $m = 3$ AR(1) mixture (blue) truncated at $k_{\max} = 1000$ against the theoretical acf an fGn (black) with $H = 0.9$. Panels 1–4 (top left to bottom right) show the acf corresponding to the approximate model using lag-weight $\psi(k) = k^{-p}$ with p equal to 0, 0.5, 1 and 2 respectively. We observe that as $k > k_{\max}$ the approximate decays increasingly rapidly as more emphasis is put on the smaller lags of the acf.

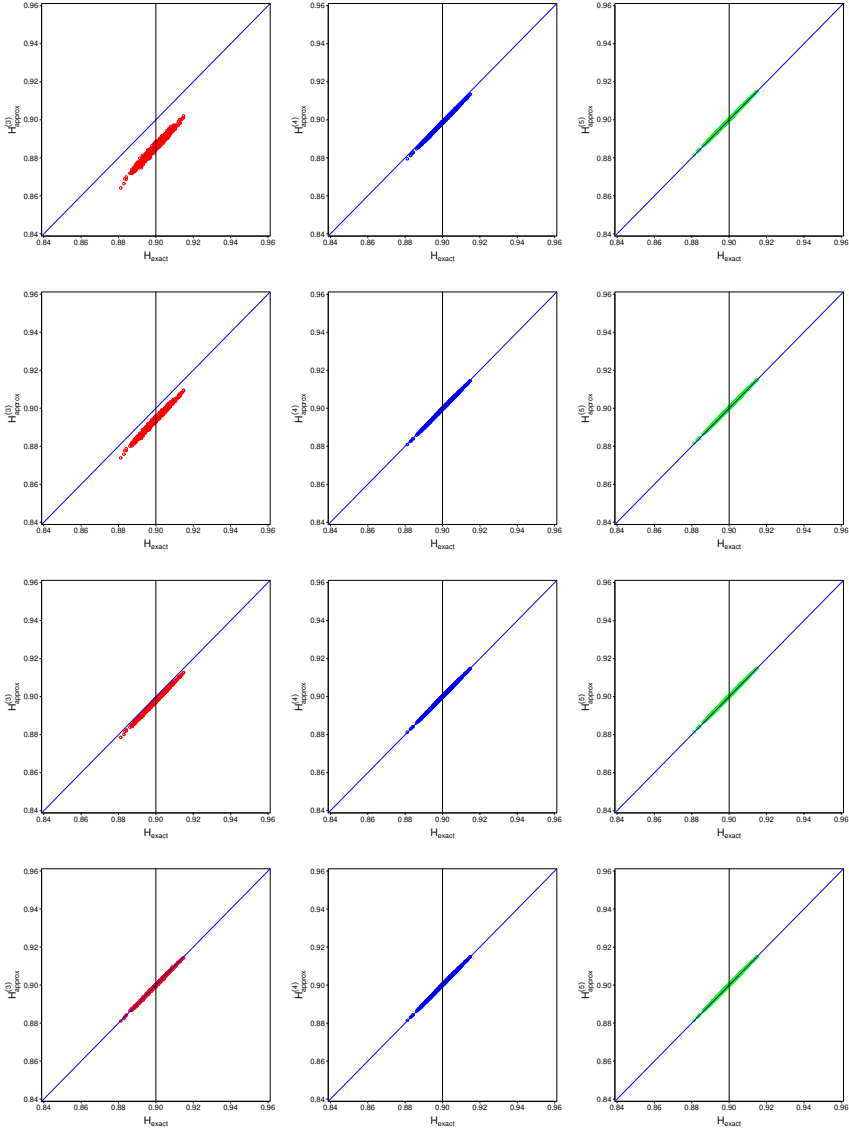


FIGURE 3.4. Scatter plot of the estimated H using the AR(1) mixture approximation with different settings against exact MLE for 1000 simulations with true $H = 0.9$ and length $n = 1000$. Rows 1–4 show result for lag-weight $\psi(k) = 1/k^p$ with p equal to 0, 0.5, 1 and 2 respectively. Columns 1–3 correspond to m equal to 3, 4 and 5 respectively. Here, $k_{\max} = 500$ for all panels.

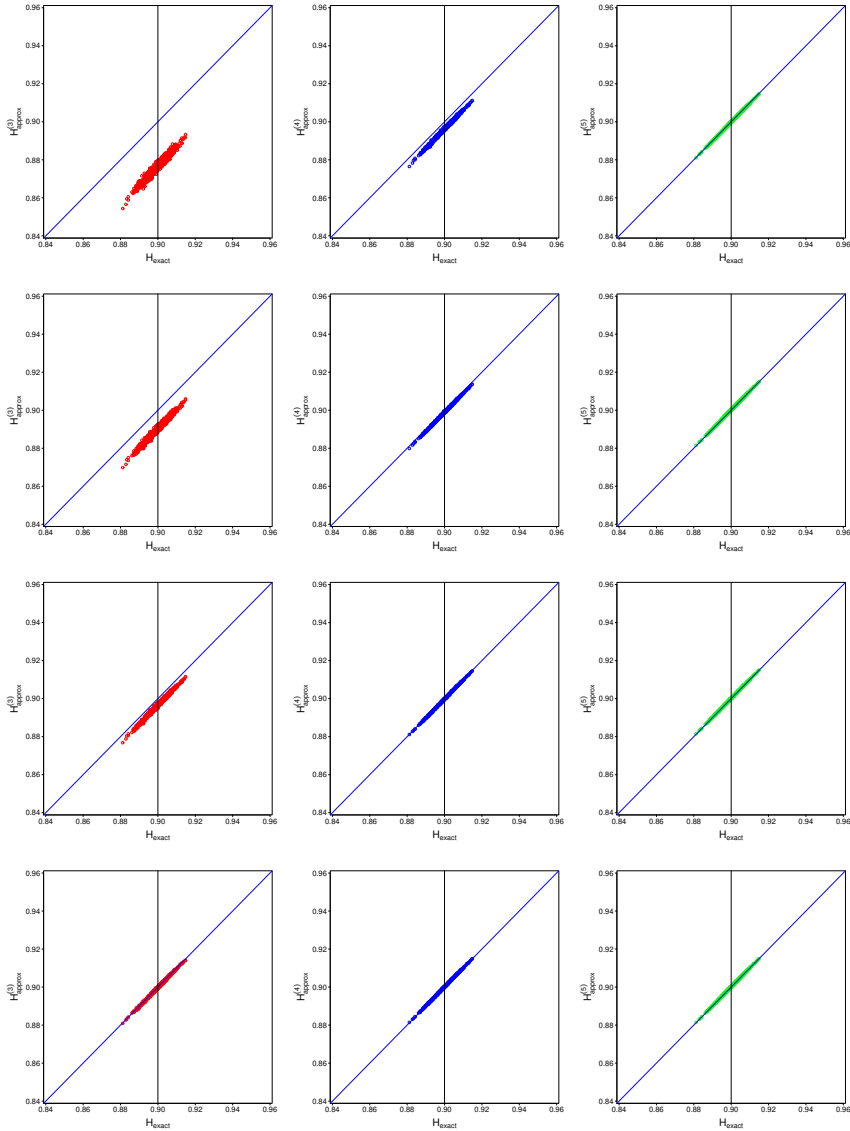


FIGURE 3.5. Scatter plot of the estimated H using the AR(1) mixture approximation with different settings against exact MLE for 1000 simulations with true $H = 0.9$ and length $n = 1000$. Rows 1–4 show result for lag-weight $\psi(k) = 1/k^p$ with p equal to 0, 0.5, 1 and 2 respectively. Columns 1–3 correspond to m equal to 3, 4 and 5 respectively. Here, $k_{\max} = 1000$ for all panels.

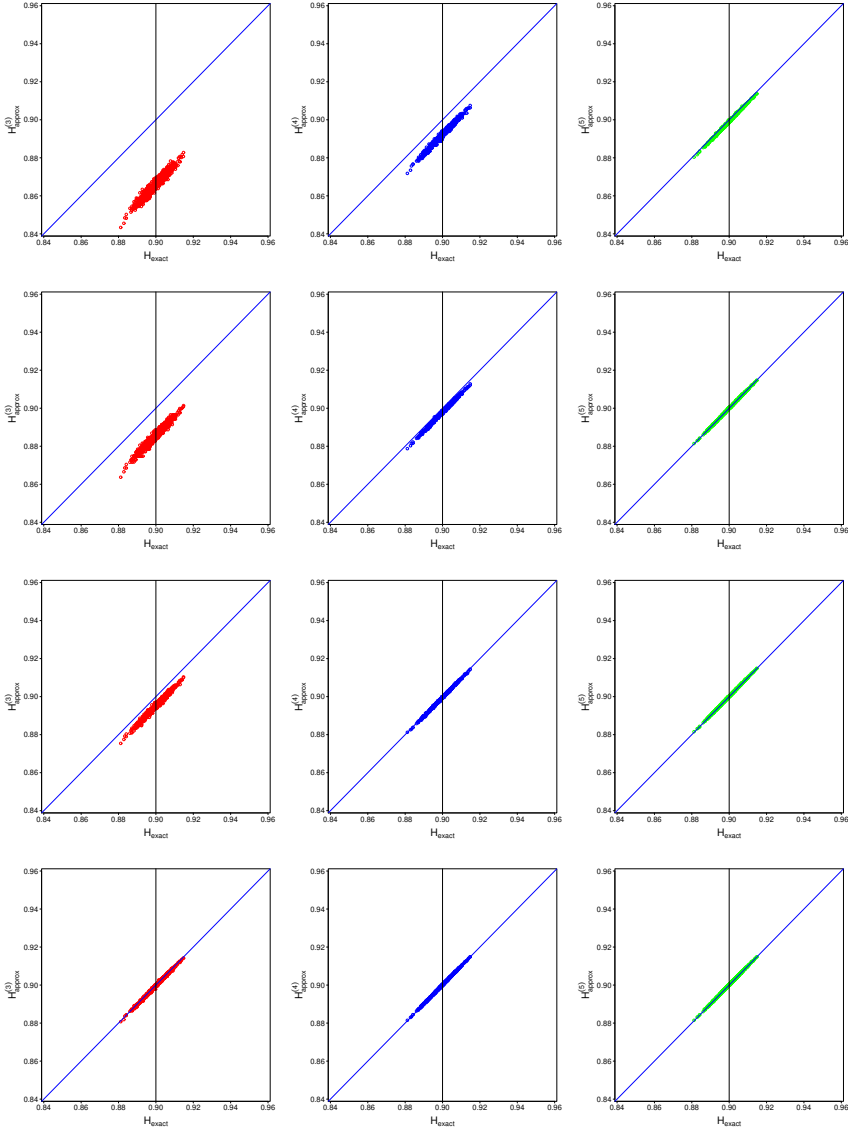


FIGURE 3.6. Scatter plot of the estimated H using the AR(1) mixture approximation with different settings against exact MLE for 1000 simulations with true $H = 0.9$ and length $n = 1000$. Rows 1–4 show result for lag-weight $\psi(k) = 1/k^p$ with p equal to 0, 0.5, 1 and 2 respectively. Columns 1–3 correspond to m equal to 3, 4 and 5 respectively. Here, $k_{\max} = 2000$ for all panels.

CHAPTER 4

Applications in climate science

4.1 Modeling global mean surface temperature

Global radiative forcing F denotes the net effect of changes to how much radiation emitted from the sun is absorbed by the earth. This radiation affects the energy balance of the earth system which leads to temperature change. Understanding the global mean surface temperature (GMST) response to radiative forcing is therefore essential to assess the risks of global climate change. For time scales ranging from months to centuries this response can be expressed as scale-invariant (Rypdal and Rypdal, 2016; Rybski et al., 2006; Lovejoy and Schertzer, 2013; Huybers and Curry, 2006; Franzke, 2010; Fredriksen and Rypdal, 2016), implying long memory properties of the temperature series. This chapter will apply the approximation obtained using the link found by equation (3.4) and introduce a computationally efficient Bayesian approach to analyse temperature series, including response to radiative forcing.

Components the radiative forcing can be determined using proxies such as ocean sediments or volcanic ash layer analysis. These contributions to radiative forcing will be treated deterministically and denoted by F_{known} , and includes forcing originating from solar variations, volcanic activity and anthropogenic effects such as land usage and emission of greenhouse gases. We use time series data produced using earth system models (ESMs) to describe F_{known} . As this data only measures change in forcing we introduce an unknown shift parameter F_0 to describe the initial level of this forcing. The remaining forcing is caused by chaotic atmospheric dynamics and will be explained stochastically using a white noise process dB/dt . Let σ denote a general scaling parameter, the total forcing is then expressed as

$$\sigma F(t) = \sigma_f (F_{\text{known}}(t) + F_0) + \sigma_\varepsilon \frac{dB(t)}{dt}, \quad (4.1)$$

where we introduce two scaling parameters σ_f and σ_ε to allow for the forcing components to be weighted differently. σ^2 denotes the total variance of the GMST anomaly ΔT . The GMST anomaly is expressed as a filtering of F

$$\Delta T(t) = T_0 + \sigma \int_{-\infty}^t g(t-s) F(s) ds, \quad (4.2)$$

where T_0 is an intercept term used to shift the temperature anomaly to the desired reference period. Inserting equation (4.1) into equation (4.2) yields that the GMST anomaly can be expressed as the sum of a forced temperature response

$$\mu(t) = T_0 + \sigma_f \int_{-\infty}^t g(t-s) F_{\text{known}}(s) ds \quad (4.3)$$

and an unforced temperature response

$$\varepsilon(t) = \sigma_\varepsilon \int_{-\infty}^t g(t-s) dB(s).$$

Assuming that the ocean layers can be represented by an m -box model as described in Fredriksen and Rypdal (2017) the response function g is a sum of m exponentials

$$g(t) = \sum_{i=1}^m w_i e^{-t/\tau_i},$$

where w_i and $\tau_i = 1 - 1/\phi_i$ denote the weights and characteristic time scales, and must be treated as unknown hyperparameters. For the 1-box model the response function is a single exponential, and the GMST response exhibits SRD and depends on four hyperparameters. These are the first-lag autocorrelation coefficient $\phi_1 = 1/(1 - \tau_1)$, the standard deviation of the forced and unforced response σ_f and σ_ε and the shift parameter F_0 . For the m -box model, the unforced response is a weighted sum of m Ornstein Uhlenbeck processes, and the GMST response is governed by $2m + 2$ hyperparameters, which is computationally expensive due to the high-dimensional parameter space. Moreover, the model is also prone to overfitting. However, as the number of boxes increase towards infinity, g can be expressed as a scale-invariant response function (Fredriksen and Rypdal, 2017)

$$g(t) = t^{H-3/2},$$

implying LRD properties. As mentioned previously, this assumption is valid for time scales ranging from monthly to centennial. All weight and time scale hyperparameters are then replaced with the Hurst exponent H , meaning that the model now has only four hyperparameters H, F_0, σ_f and σ_ε . This means that the scale-invariant response has just as many hyperparameters as the exponential response associated with the 1-box model, but is able to describe heat transmission between the ocean layers more accurately.

Myrvoll-Nilsen et al. (2019b) compare the two approaches for different applications, and observe that the scale-invariant response routinely provides estimates that are much closer to projections obtained using more sophisticated models compared to using an exponential response, which tend to underestimate.

4.2 Statistical model

If we discretise $\Delta\mathbf{T} = (\Delta T(t_1), \dots, \Delta T(t_n))^\top$ and $\mathbf{F} = (F(t_1), \dots, F(t_n))^\top$ we see that the GMST anomalies follow an fGn with mean vector $\boldsymbol{\mu} = (\mu_1, \dots, \mu_n)^\top$ and covariance matrix $\mathbf{Q}^{-1} = \text{Cov}(\boldsymbol{\varepsilon})$, where $\boldsymbol{\varepsilon} = (\varepsilon_1, \dots, \varepsilon_n)^\top$. We let $\boldsymbol{\theta} = (H, F_0, \sigma_f, \sigma_\varepsilon)^\top$ denote the hyperparameters and define a latent Gaussian model as follows:

- The likelihood of the data $\Delta\mathbf{T}$ is assumed to be Gaussian with fixed negligible variance and mean expressed through the predictor

$$E[\Delta\mathbf{T}] = \boldsymbol{\eta} = \boldsymbol{\mu}(H, F_0, \sigma_f) + \boldsymbol{\varepsilon}(H, \sigma_\varepsilon).$$

- Since both latent model components $\boldsymbol{\mu}$ and $\boldsymbol{\varepsilon}$ in the predictor depend on H our model is of non-standard form and cannot be treated in INLA without modifications. We therefore choose to consider the sum $\boldsymbol{\mu} + \boldsymbol{\varepsilon}$ as a single component. Using the approximate fGn model specified in equation (3.2) with m AR(1) components the latent Gaussian field is defined as $\mathbf{x} = (\boldsymbol{\eta}^\top, (\boldsymbol{\mu} + \tilde{\mathbf{x}}_m)^\top, \mathbf{x}_1^\top, \dots, \mathbf{x}_m^\top)^\top$.
- Priors are assigned independently to the hyperparameters

$$\pi(\boldsymbol{\theta}) = \pi(H)\pi(F_0)\pi(\sigma_f)\pi(\sigma_\varepsilon).$$

For the Hurst exponent H and the precision hyperparameters $\kappa_f = 1/\sigma_f^2$ and $\kappa_\varepsilon = 1/\sigma_\varepsilon^2$ we assign PC priors, and for the shift parameter F_0 we assign a Gaussian prior.

Inference is obtained using INLA, but since the fGn latent model component in R-INLA does not allow for the inclusion of mean $\boldsymbol{\mu}(H, F_0, \sigma_f)$ we have to construct it manually using `rgeneric`. Furthermore, since we consider the sum $\boldsymbol{\mu} + \boldsymbol{\varepsilon}$ as a single latent model component we only get the posterior marginal distributions for $\boldsymbol{\mu} + \boldsymbol{\varepsilon}$, not the marginal for $\boldsymbol{\mu}$ and $\boldsymbol{\varepsilon}$ separately. These can, however, be obtained by performing Monte Carlo simulation from the joint posterior distribution of the hyperparameters, see Myrvoll-Nilsen et al. (2019b) for further details.

In order to make the given temperature response model easily accessible we have provided a user-friendly R-package called `INLA.climate` which takes care of all the technical implementations and presents the results in a readable format. This package is available at the GitHub repository `eirikmn/INLA.climate`. A description and tutorial of the package and its features is included in appendix A.

4.3 Temperature predictions

An important goal in climate analysis is to compute future temperature predictions. Using the `INLA.climate` package we can compute future temperature as a response to future forcing scenarios. By assigning NA values for the variables we want to predict, INLA will produce the marginal posterior distributions of the missing temperature variables. For the `INLA.climate` package this is done automatically within the `inla.climate` function whenever the `forcing` input variable is an object of greater length than the `data` temperature input.

In Myrvoll-Nilsen et al. (2019b) we use future forcing data based on the trajectories for greenhouse gas concentration adopted by the intergovernmental Panel on Climate Change (IPCC), known as representative concentration pathways (RCPs). There are four RCP trajectories selected for climate modeling. These include RCP2.6 (van Vuuren et al., 2007; van Vuuren et al., 2006), RCP4.5 (Clarke et al., 2007; Smith and Wigley, 2006; Wise et al., 2009), RCP6 (Fujino et al., 2006; Hijioka et al., 2008) and RCP8.5 (Riahi et al., 2007; Rao and Riahi, 2006), which are named after the value assumed for the radiative forcing (in W/m^2) for the year 2100. The RCP forcing scenario data sets are downloaded from the Integrated Assessment Modeling Consortium (IAMC) data base hosted by the International Institute for Applied Systems Analysis (IIASA) on 2019-08-22. The data sets consist of decennial global forcing data, and annual data is obtained by interpolation using splines.

For the past interval of 1850–2015, we use the HadCRUT4 temperature dataset, paired with an updated version of the greenhouse gas component of the forcing introduced in Hansen et al. (2011). The RCP scenarios are used to describe the forcing in the 2015–2100 range, and are shifted such that the forcing value at year 2015 equals that for the Hansen forcing. The RCP scenarios are presented in figure 4.1 where they have been appended to the greenhouse gas (GHG) component of the Hansen forcing.

Using a scale-invariant and an exponential response model we obtain predictions of the GMST. These are both compared to the temperature projections presented in table SPM.2 of IPCC’s fifth assessment report (AR5) (IPCC, 2013). The results are illustrated in figure 4.2. When compared to the AR5 projections we observe that an exponential response model underestimates the temperature response. This is because the exponential model does not take into account the heat exchange with the deep ocean which increases the temperature response to forcing. On the other hand, the scale-invariant approach tends to overestimate the response. However, we conclude that the scale-invariant response model is overall more accurate than the exponential model when compared to the AR5 projections.

4.3 – Temperature predictions

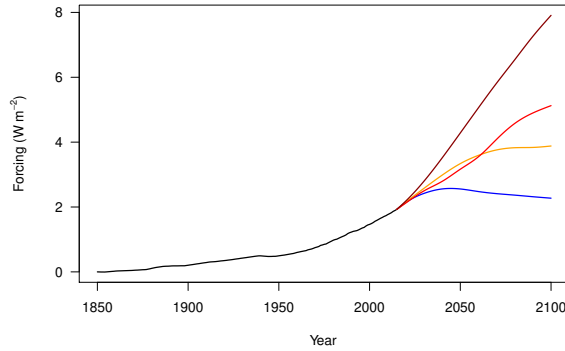


FIGURE 4.1. The RCP2.6 (blue), RCP4.5 (orange), RCP6 (red) and RCP8.5 (darkred) global radiative forcing scenarios appended to the GHG component of the Hansen forcing (black).

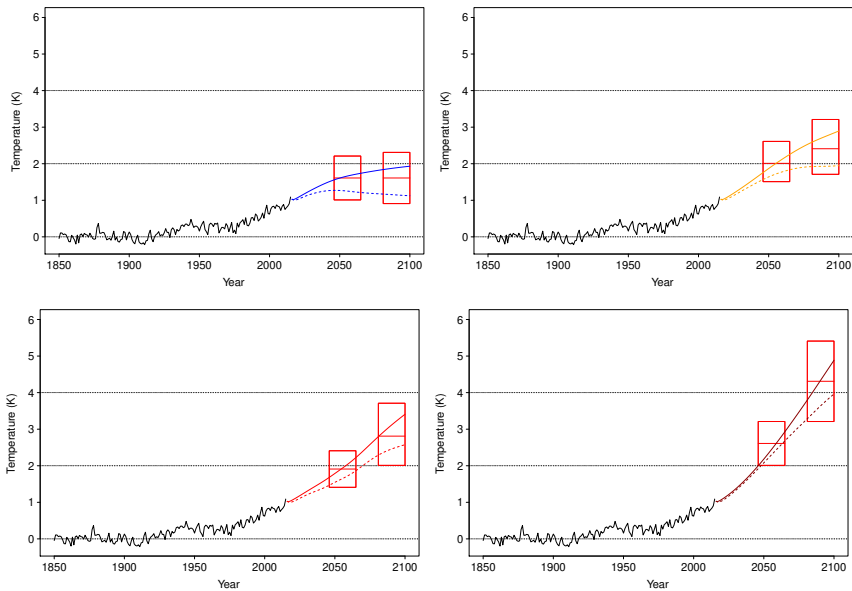


FIGURE 4.2. The posterior marginal means of the GMST response to the RCP2.6 (blue), RCP4.5 (orange), RCP6 (red) and RCP8.5 (darkred) appended to the HadCRUT4 temperature data (black) using both a scale-invariant (solid) and exponential (dashed) response model. The rectangle describes the AR5 projection area for each scenario.

4.4 Climate sensitivity measures

Climate sensitivity describes how the GMST responds to changes in radiative forcing. There are three ways of expressing climate sensitivity. This include the transient climate response (TCR), the equilibrium climate sensitivity (ECS) and the earth system sensitivity (ESS). Each of these are each defined over different time scales. The TCR describes the response after 70 years, the ECS after centuries and the ESS after multiple millennia. For this project we have developed methodology to obtain Bayesian inference empirically for both the TCR and the ECS since these are the sensitivities relevant for the time scales where the scaling assumption is valid.

4.4.1 Transient climate response

The transient climate response is defined as the amount the temperature will increase after a gradual CO₂-doubling in the atmosphere. Following a 1% annual increase this will be reached after 70 years. Mathematically, this implies future radiative forcing

$$f(s) = \frac{Q_{2 \times \text{CO}_2}}{70 \text{yrs}}(s + F_0), \quad \text{for } s = 1, \dots, 80 \text{yrs},$$

where $Q_{2 \times \text{CO}_2}$ is a model specific coefficient describing the increased forcing following a CO₂-doubling. For a list of $Q_{2 \times \text{CO}_2}$ corresponding to the ESMs of the CMIP5 ensemble see Forster et al. (2013). We obtain the posterior distribution of the TCR by Monte Carlo sampling. After fitting the model to some temperature and forcing data with INLA we sample the hyperparameters from the obtained joint posterior distribution $\pi(\boldsymbol{\theta} \mid \mathbf{y})$. Then we compute the forced temperature response to the future forcing, given by

$$\Delta T(t) = \sigma_f \int_0^t (t - s)^{H-3/2} (f(s) + F_0) \quad \text{for } t = 1, \dots, 80 \text{yrs}.$$

Finally, the TCR samples are formed by taking the average of the forced temperature response 60–80 years in the future. This procedure can be done using the `inla.climate.tcr` function in the `INLA.climate` package. Typically, the TCR of temperature and forcing data generated from an ESM are computed by letting the model run for 80 years longer under the appropriate conditions. An advantage of our approach is that it allows for empirical estimation of the TCR based exclusively on the temperature observations and corresponding forcing data. Additionally, this is a great computational advantage since advanced ESMs typically require long runtime to obtain the same results which takes only seconds using our approach. In Myrvoll-Nilsen et al. (2019b) we compare the posterior marginal means for 19 different ESMs from the CMIP5 ensemble with their corresponding TCR values obtained directly from the model realisation. The empirical estimates showed an 86% correlation with TCR values obtained directly from the

ESMs. We also perform similar comparison using instead an exponential response function. This showed a correlation of 78%. During the review process we have also extended the package to allow for general m -box models to be used. In the revised manuscript we will also estimate TCR of the ESMs using a sum of two exponentials response function.

We also estimate the TCR for the historical HadCRUT data set. This was done by pairing the HadCRUT data set with each of the 19 forcing observations as well as the Hansen forcing data set. 100,000 TCR samples are generated for each pairing which resulted in a mean TCR of 1.53K and standard deviation of 0.33K.

4.4.2 Equilibrium climate sensitivity

The equilibrium climate sensitivity describes the expected temperature increase resulting from an immediate and sustained CO₂-doubling after the temperature has reached equilibrium. Mathematically, this is defined as

$$\text{ECS} = Q_{2 \times \text{CO}_2} \int_0^{\infty} g(t) dt, \quad (4.4)$$

where $Q_{2 \times \text{CO}_2}$ denote the model specific constant forcing corresponding to a CO₂-doubling, see IPCC (2013) for a list of estimated values corresponding to the ESMs of the CMIP5 ensemble. In Rypdal et al. (2018) we assume g to be scale-invariant which causes the ECS to diverge towards infinity. This is because scale-invariance is an accurate description of GMST response only for monthly to centennial time scales. The truncated integral

$$\hat{\text{ECS}}_T = Q_{2 \times \text{CO}_2} \int_0^T g(t) dt, \quad (4.5)$$

is therefore a good approximation of the truncated integral of the true response function for $T \leq 1000$. This is true regardless of whether g is exact scale-invariant or approximated using a weighted sum of exponentials selected according to equation (3.4). If we choose the upper limit T to be sufficiently high, the truncated integral will be consistent with the ECS estimate obtained using Gregory plots (Gregory et al., 2004). The estimate can hence be improved by performing a linear fit

$$\text{ECS} = \alpha + \beta \hat{\text{ECS}}_T,$$

where we found $\alpha = 1.09\text{K}$ and $\beta = 0.61$ using the same ESMs used in estimating the TCR previously, and $T = 1000$. Similar to the TCR we estimate the ECS of the HadCRUT4 temperature data set, by pairing it with forcing from Hansen et al. (2011) and forcing data from 19 different ESMs. Here we use forcing $Q_{2 \times \text{CO}_2} = 3.8\text{W/m}^2$ for all 20 analyses. We find that the ECS ranges from 2.3 to 3.4K, see Rypdal et al. (2018) for details about the approach and the results.

4.5 Local temperature data

The speed of the INLA procedure and the AR(1) mixture approximation allows for a larger number of analyses within a feasible time frame. In Myrvoll-Nilsen et al. (2019a) we use the approximate scale-invariant model to perform Bayesian inference for the local time series data from the GISS Surface Temperature Analysis version 4 (GISTEMP v4) (GISTEMP Team, 2018; Lenssen et al., 2019). This is a spatio-temporal gridded data set with spatial resolution of $2^\circ \times 2^\circ$ where for each local point there is a time series covering the annual temperature data between 1900–2015. After eliminating locations where the associated temporal data set were too inconsistently measured, or had too many missing temporal observations, we have $n_s = 11,997$ individual time series. These are denoted $\mathbf{y}_s = (y_{1,s}, \dots, y_{n_t,s})^\top$ and are each of length $n_t = 116$. We do not consider any spatial correlation between the points in space and analyse each local time series independently. The objective of this paper was to investigate temperature increases for local time series by considering a linear trend. We also want to investigate the memory properties of the local time series and compare the results with Løvsletten and Rypdal (2016) whom consider a linear trend model,

$$y_{s,t} = \alpha_s + \beta_s t + \epsilon_{s,t}. \quad (4.6)$$

This model does not account for any forcing and uses either an AR(1) or an fGn process to describe the residuals $\epsilon_{s,t}$.

The first approach we consider to estimate the trend term β is to fit a similar model using a latent Gaussian modeling formulation. We assume each local times series to be explained by the linear predictor

$$\eta_{1,t} = \alpha + \beta t + \varepsilon_t(H, \sigma_\varepsilon). \quad (4.7)$$

Here, α is an intercept term, β is a linear trend term and $\varepsilon_t(H, \sigma_\varepsilon)$ is an fGn term. Inference is obtained using R-INLA.

A second approach to estimating β is to first fit a model corresponding to the linear predictor

$$\eta_{2,t} = \mu_t(H, \sigma_f, F_0) + \varepsilon_t(H, \sigma_\varepsilon). \quad (4.8)$$

Here, $\varepsilon = (\varepsilon_1, \dots, \varepsilon_n)^\top$ is an fGn term and $\boldsymbol{\mu} = (\mu_1, \dots, \mu_n)^\top$ is the forced temperature response as described in equation (4.3). Fitting this model with INLA yields the posterior distribution $\pi(H, \sigma_\varepsilon \mid \mathbf{y})$. We wish to estimate the trend term β from equation (4.7) where H and σ_ε reflect the variation found by fitting equation (4.8). This is done by fitting equation (4.7), where H and σ_ε are fixed to be equal to samples (H_i, σ_i) from the posterior obtained from fitting equation (4.8)

$$(H_i, \sigma_i) \sim \pi(H, \sigma_\varepsilon \mid \mathbf{y}_s).$$

Repeating the analysis for n_{sim} samples of (H, σ_ε) yields n_{sim} posterior marginal mean estimates of β . These are denoted by $\hat{\beta} = (\hat{\beta}_1, \dots, \hat{\beta}_{n_{\text{sim}}})^\top$. The average posterior marginal mean, denoted by $\tilde{\beta}$, of the linear trend term is found by

$$\tilde{\beta} = \frac{1}{n_{\text{sim}}} \sum_{j=1}^{n_{\text{sim}}} \hat{\beta}_j.$$

Let the latent Gaussian field \mathbf{x} includes all stochastic terms in equation (4.7), including the trend term β . Since equation (4.7) has no free hyperparameters left the posterior distribution of \mathbf{x} is expressed as

$$\pi(\mathbf{x} \mid \mathbf{y}_s) \propto \pi(\mathbf{y}_s \mid \mathbf{x})\pi(\mathbf{x}).$$

Since both $\pi(\mathbf{y}_s \mid \mathbf{x})$ and $\pi(\mathbf{x})$ are Gaussian then so is $\pi(\mathbf{x} \mid \mathbf{y}_s)$, and by extension $\pi(\beta \mid \mathbf{y}_s)$. This implies linearity meaning $\tilde{\beta}$ is the posterior marginal mean estimate found by fitting equation (4.7), using fixed hyperparameters H and σ equal to the posterior marginal means \hat{H} and $\hat{\sigma}_\varepsilon$ obtained by fitting equation (4.8). This means that we can obtain $\tilde{\beta}$ using a single INLA analysis without having to sample from the posteriors of equation (4.8). Using these two approaches we form separate IGms which are analysed using the R-INLA framework for all local time series. What would otherwise be a computationally infeasible task is, by taking advantage of INLA and the AR(1) mixture approximation for the fGn component, completed in around 20 hours.

We found that when using either of the two approaches, the probability of a positive trend was highly positive, i.e. $\text{Prob}\{\beta > 0 \mid \mathbf{y}_s\} > 0.95$, for 84% of local time series using the model corresponding to equation (4.7), and 89% for the model corresponding to equation (4.8). This exceeded the ratio of 80% found in Løvsletten and Rypdal (2016) using equation (4.6) where $\varepsilon_{s,t}$ is the most optimal local selection between an AR(1) and fGn model for the error term. For comparison, we repeated the analyses for the intervals 1900–1950 and 1900–1985. For the time period 1900–1950 we find the trend to be significantly positive for 30% and 38% of the local time series for the two models, respectively, and for 1900–1985 we find the same proportion to be 43% and 52%. This difference demonstrates that, when spatial correlation is ignored, the warming trend has increased significantly, even locally, for the past 30 years, well above what could be ascribed to random noise.

Another benefit of our methodology is that we compute the posterior marginal distributions of all hyperparameters in our models, allowing us to observe how the estimated Hurst exponent vary locally. This is illustrated in figure 4.3 which indicates that ocean data exhibits a significantly higher degree of memory compared to land data. Our model also suggests

that the Hurst exponent is lower for the area around the El Niño Southern Oscillation (ENSO) than the surrounding area. This constitute another difference between our results and that of Løvstletten and Rypdal (2016), whom suggested an exceptionally high degree of memory in the same area.

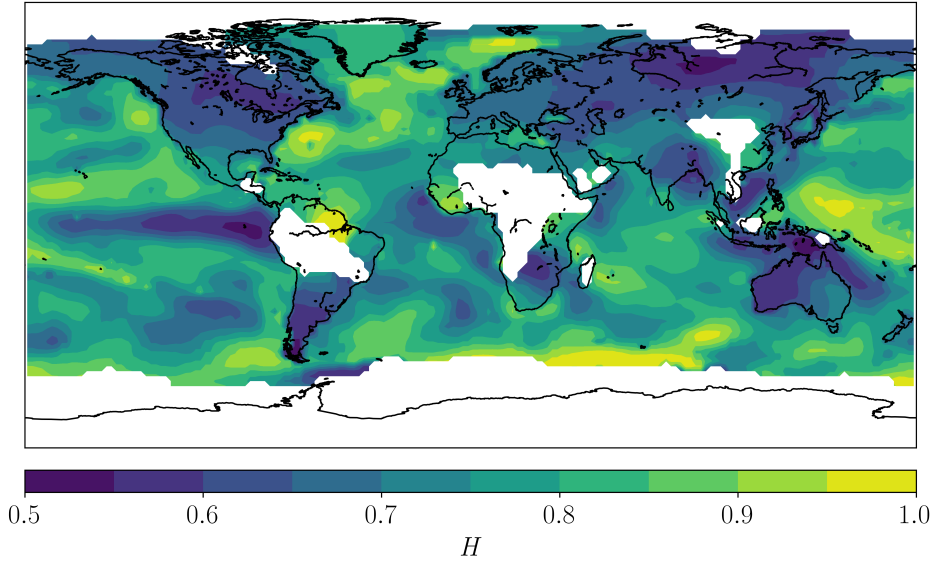


FIGURE 4.3. The posterior marginal mean estimate of the Hurst exponent obtained from fitting the lGm corresponding to η_2 to local time series data from 1900–2015.

4.6 Future work: Spatio-temporal modeling

Geographically close observations are often correlated, as is seen when temperatures are measured at locations in close proximity to one another. Incorporating spatial correlation into a model is therefore important in order to properly describe behaviour expressed in spatio-temporal data, such as the GISTEMP v4 temperature data set analysed in section 4.5. Applications of spatio-temporal models which exhibit LRD in time are not limited to climate science, but are found in numerous fields. Examples include analysis of wind speed data (Haslett and Raftery, 1989), analysis of vegetation variation (Jiang et al., 2014) and urban traffic volume modeling (Vlahogianni et al., 2007). However, easily applicable methods to perform Bayesian analysis of spatio-temporal data exhibiting temporal LRD appear to be limited.

A possible future extension of the methodology presented in this thesis is therefore to develop a spatio-temporal latent model component which incorporates temporal LRD within the latent Gaussian modeling framework. This allows the use of R-INLA to perform Bayesian inference. Currently R-INLA supports several spatio-temporal latent model components, see e.g. Cameletti et al. (2013) and Blangiardo et al. (2013) for an example. However, no spatio-temporal models that incorporate temporal LRD are currently included.

As modeling of spatio-temporal data often involves a high number of latent variables it is important that the latent Gaussian field is a GMRF. In this project we have shown that temporal LRD can be represented by an approximate GMRF using the mapping found in equation (3.4). A computationally efficient model for spatial correlation is obtained by exploiting an explicit link between a continuous Gaussian random field and an approximate GMRF presented in Lindgren et al. (2011). Specifically, this assumes the spatial correlation to be expressed by a Matérn acf

$$\rho_s(k) = \frac{1}{\Gamma(\nu)2^{\nu-1}}(\kappa d)^\nu K_\nu(\kappa d).$$

Here, $k = \|\mathbf{s}_i - \mathbf{s}_j\|$ denotes the Euclidean distance between the two spatial points, κ is a scaling parameter, ν defines the smoothness of the process and K_ν denotes the modified Bessel function of the second kind of order $\nu > 0$. This process is referred to as a Matérn field and represents any exact solution to the stochastic partial differential equation (SPDE)

$$(\kappa^2 - \Delta)^{\alpha/2}x(\mathbf{u}) = \mathcal{W}(\mathbf{u}), \quad (4.9)$$

where $\mathbf{u} \in \mathbb{R}^d$, $\alpha = \nu + d/2$, $\kappa > 0$, $\nu > 0$ and $(\kappa^2 - \Delta)^{\alpha/2}$ is a pseudodifferential operator (Whittle, 1954; Whittle, 1963). \mathcal{W} is a spatial Gaussian white noise process with unit variance and Δ is the Laplacian operator. According to Whittle (1954), the most natural choice for the smoothing parameter in two dimensions is $\nu = 1$, implying that $\alpha = 2$.

The idea behind the SPDE approach is to represent the GRF as a set of non-intersecting triangles. Mesh nodes are placed at the observed locations $\mathbf{s} = (\mathbf{s}_1, \dots, \mathbf{s}_{n_s})^\top$ and additional nodes are placed in order to properly represent the enclosing area. Triangles are drawn between these nodes to create an approximate discrete representation of the continuous Matérn field

$$x(\mathbf{s}) = \sum_{i=1}^{n_m} \psi_i(\mathbf{s})\omega_i,$$

using piecewise linear basis functions $\{\psi_i(\mathbf{s})\}$ chosen such that $\psi_i = 1$ for vertex i and 0 for any other vertex. n_m is the number of mesh nodes and $\{\omega_i\}$ are Gaussian weights which determine the height of each triangle. Doing so

establishes a link between the Matérn field and an approximate GRF with a neighbourhood structure which grants the Markov property. The SPDE model is included in R-INLA as one of the default latent model components for spatial modeling. See e.g. Bakka et al. (2019), Huang et al. (2017) and Hambly and Søjmark (2018) for examples of applications, and Krainski et al. (2018), Blangiardo and Cameletti (2015) and Bakka et al. (2018) for details and a review on spatial modeling with R-INLA.

Spatio-temporal latent Gaussian models are prone to having a very high dimension. Even if we wish to fit a spatio-temporal model to only a subset of the GISTEMP v4 data set the number of variables could be overwhelming. For the area illustrated in figure 4.4, covering the six European countries of Germany, Slovakia, Austria, Hungary, Poland and the Czech Republic, there are 30 temporal points, using a rather sparse mesh of $n_m = 78$ vertices. Assuming the approximate temporal component is represented by $m = 4$ AR(1) processes and $n_t = 116$, the number of latent variables corresponding to the latent Gaussian field would be $(m + 1)n_t n_m = 45240$ nodes.

Different methods of simplifications are often necessary to overcome the associated computational complexity. One major simplification is to assume the spatio-temporal latent model component to be separable, i.e. its acf can be expressed as the product of one pure temporal acf and one pure spatial acf. This implies that the precision matrix of the latent Gaussian field \mathbf{Q} is equal to the Kronecker product of the precision matrix of one temporal and one spatial model,

$$\mathbf{Q} = \mathbf{Q}_t \otimes \mathbf{Q}_s.$$

Here \mathbf{Q}_t is the precision matrix corresponding to the AR(1) mixture approximation and \mathbf{Q}_s is the precision matrix of the spatial process specified according to the SPDE approach. For details on the entries of \mathbf{Q}_t and \mathbf{Q}_s , see Sørbye et al. (2019) and Lindgren et al. (2011), respectively.

Although convenient, separable spatio-temporal models are often found to be too simplistic in practice, see e.g. Cressie and Huang (1999). A separable spatio-temporal model will assume identical temporal correlation for each local time series. However, in analysing climatic data temporal memory vary considerably depending on the geographical location, as illustrated in figure 4.3. We are therefore limited to analysing spatial domains that are homogeneous in terms of temporal memory. This often implies local time series that are in close proximity to one another which are often very similar. Hence, data that can be adequately fitted by a separable spatio-temporal model can often be described almost as well just by fitting pure temporal models to each local time series independently.

A more interesting and applicable aim would therefore be to create a non-separable spatio-temporal latent model component, see e.g. Cressie and Huang (1999) or Gneiting (2002) for examples of valid non-separable

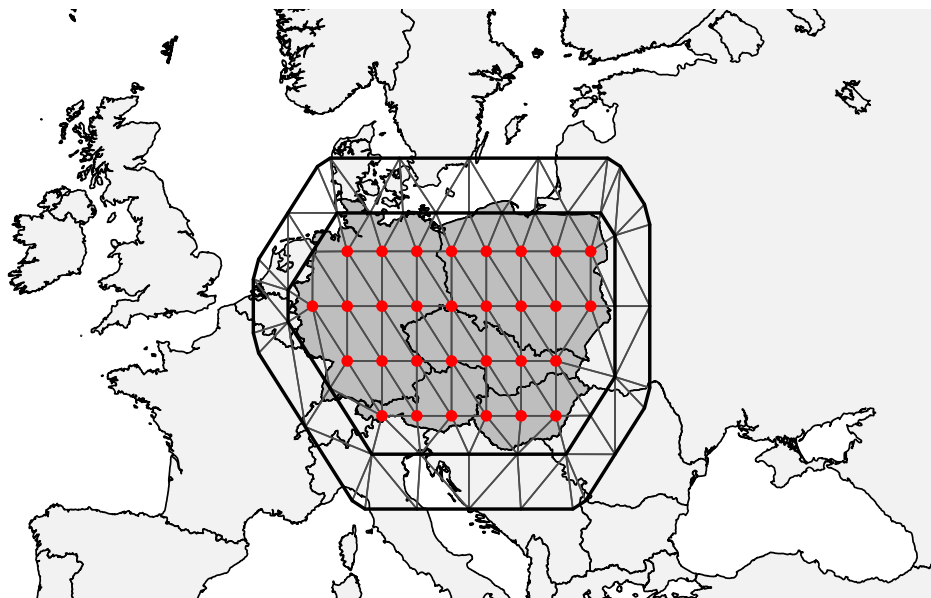


FIGURE 4.4. The GISTEMP v4 local temperature time series locations and spatial mesh. The map is made using the `maps` package for R which is based on the very old database `worldHires`. Hence why some of the borders are outdated.

space-time covariance functions. Although non-separable spatio-temporal modeling is considerably more difficult than separable modeling it is possible to perform it in R-INLA, but it is currently rather limited. It is, however, a topic of ongoing research within the R-INLA community, and new models are currently in development. See Krainski (2018) for a recent overview of non-separable spatio-temporal modeling in R-INLA. We were unable to finish this work in time for it to be included in this thesis, but we hope to complete it in the near future.

Concluding remarks

Models exhibiting long-range dependence are useful in describing the persistent correlation found in climatic time series that cannot be expressed using the more computationally advantageous SRD processes. We have found that if the weights and first-lag autocorrelation parameters are chosen carefully using numerical optimization then a weighted sum of AR(1) processes can represent LRD processes with remarkable accuracy. Using only four AR(1) processes one is able to produce an aggregate process that accurately replicates the LRD correlation structure of an fGn. The resulting approximation inherits the computational properties of the AR(1) processes, most notably a sparse precision matrix. Moreover, we demonstrate that the given approximation fits into the flexible class of latent Gaussian models, allowing for the efficient computational framework of R-INLA to be employed. Moreover, it allows us to introduce model components that incorporate seasonal variation, linear trends and spatial correlation. The computational advantage of using this approximate fGn model is substantial and allows Bayesian inference to be obtained in linear time and memory using INLA.

Using this approximation we are able to define a computationally efficient model for both local and global climatic time series data in terms of an IGM which incorporates knowledge of radiative forcing in order to better describe the climatic system. This model has been applied to several problems in climate science, including the estimation of climate sensitivity measures, temperature predictions to possible future scenarios and analysis of local time series data. Since the model is of non-standard form it is not supported by latent model components already specified in the R-INLA package and thus has to be created using `rgeneric`. We have therefore made the methodology available in the user-friendly `INLA.climate` package, allowing applied climate scientists that may not be familiar with R-INLA to adopt our model.

The methodology presented in this project is limited to stationary and persistent LRD processes with Hurst exponent $0.5 < H < 1$. This excludes applications with anti-persistence found in fields such as electricity pricing (Weron and Przybyłowicz, 2000; Simonsen, 2003) and finance (Kyaw et al., 2006; Huang et al., 2012), as well as non-stationary processes with $H > 1$

which are known to occur in analysing tree-ring width (Telesca and Lovallo, 2010).

Although we have so far only applied this methodology for fractional Gaussian noise and, to some extent, the ARFIMA(0, d , 0) process it could theoretically be used to approximate any stationary and persistent Gaussian LRD process whose memory structure is governed by a single parameter. However, this does imply that the more general ARFIMA(p , d , q) models, which allow for both short and long memory to both be incorporated simultaneously, is not supported. Being compatible with the class of latent Gaussian models allows for short memory to be incorporated as separate latent model components instead. However, this does not capture the interaction between short and long memory present in the ARFIMA(p , d , q) models. Although it would certainly be interesting to investigate the possibility of extending this methodology to general ARFIMA(p , d , q) processes it is considered beyond the scope of this project.

APPENDIX A

The `INLA.climate` package

Having to implement the GMST model described in chapter 4 includes specifying the model using the `rgeneric` framework. This is a somewhat technical procedure which might discourage users with limited experience with R-INLA from adopting our model. We have therefore created an R-package called `INLA.climate` which manages all the technical parts of the INLA model specification and provides a convenient and user-friendly interface. The package includes functions that execute the INLA analysis and presents all results in a readable format. The package and all source code therein has been made publicly available at the GitHub repository `eirikmn/INLA.climate`.

To increase speed I have written the most computationally expensive parts of the code in C. These include the specification of the graph, precision matrix and the mean vector corresponding to the forced temperature response. Any questions or issues regarding this package can be directed to `eirikmn91@gmail.com`. As the package is still in an early phase changes are likely to be made. The accompanying documentation gives an updated description of the functions included in the package.

A.1 Installation

The software is available for the programming environment R of version 3.5 and above, and should work on Windows, Linux and Mac operating systems. However, testing has been done primarily on Mac. If the `devtools` package is already installed it can be downloaded directly from the R console using the command

```
devtools::install_github("eirikmn/INLA.climate")
```

Alternatively, the package can be downloaded directly from the GitHub repository at `www.github.com/eirikmn/INLA.climate`. For this package to work one must have the testing version of the INLA package already installed. This can be downloaded and installed by the following command:

```
install.packages("INLA", repos=c(getOption("repos"),  
  INLA="https://inla.r-inla-download.org/R/testing"), dep=TRUE)
```

A.2 How to use the package

A.2.1 Loading data

The `INLA.climate` package contains various temperature and forcing data sets. This include the HadCRUT4 temperature data, the forcing data from Hansen et al. (2011) and temperature and forcing data associated with 19 different ESMs from the CMIP5 ensemble. The forcing data from the ESMs are adjusted such that the 18-year moving averages equal that of the Hansen forcing. The package does of course work when using other data sets as well. Data can be loaded in R by the `data` function. For example, the GISS-E2-R data set can be loaded by `data("GISS_E2_R")`. See the package documentation for more information about the data sets.

A.2.2 Selecting noise model

The noise model to be used in the INLA fitting procedure is specified in the `model` input variable. In this paper the noise model has mostly been assumed to be fractional Gaussian noise. This is the default choice in `INLA.climate`, but other options include the ARFIMA(0, d , 0) model and an aggregate AR(1) model. The fGn process is selected by `model="fgn"`, the ARFIMA(0, d , 0) process is selected by `model="arfima"` and the aggregate AR(1) process is selected by `model="ar1"`.

The input variable `m` determines how many AR(1) components are used to form an aggregate process. If $m = 1$ the noise model equals a single AR(1) component of weight $w = 1$. For the LRD noise models the weights and first-lag autocorrelation parameters are linked with the Hurst exponent H for the fGn, or $d = H - 1/2$ for the ARFIMA(0, d , 0) model, according to equation (3.4). For the AR(1) aggregate noise model however, they are instead treated as free hyperparameters. Increasing m for `model="ar1"` will therefore increase the number of hyperparameters and as a result considerably increase the runtime of INLA as well. For m AR(1) components the total number of hyperparameters in the model is $2m + 2$. Furthermore, the AR(1) aggregation differs from the LRD models also in how the transient climate response (TCR) and the forced temperature response μ is computed, as the Green's function is now a sum of exponentials

$$g(t) = \sum_{i=1}^m w_i e^{-t/\tau_i},$$

where w_i and $\tau_i = 1/(1 - \phi_i)$ denote the weight and time scale hyperparameters. For $m > 1$ these hyperparameters are found by Monte Carlo simulations.

A.2.3 Performing INLA analysis

The primary function of `INLA.climate` is called `inla.climate`. This function performs the INLA fit and can also provide estimations for the transient climate response (TCR) and the forced temperature response μ . The full function header is:

```
inla.climate(data, forcing,
  Qco2 = NULL, compute.mu = NULL, stepLength = 0.01,
  restart.inla = FALSE, m = 4, model = "fgn",
  print.progress = FALSE,
  inla.options = list(),
  tcr.options = list(),
  mu.options = list(),
  ar1.options = list() )
```

The header lists the input arguments of the `inla.climate` function. However, only the arrays `data` and `forcing` are required to run the function. These represent the temperature and forcing data. The other input arguments allow the user to specify the settings of the INLA fitting procedure, the fGn approximation and the Monte Carlo sampling schemes, if any. While most of these settings are specified within the list objects `inla.options`, `tcr.options`, `mu.options` and `ar1.options`, the most relevant ones are included in the function header explicitly. These describe the step length used in the INLA numerical scheme (`stepLength`), whether or not the INLA procedure should restart the numerical procedure at the found optima for increased accuracy (`restart.inla`), the number of AR(1) processes used to approximate the noise model (`m`), which noise model should be used (`model`) and whether or not the operations performed should be printed to the screen (`print.progress`).

For the more experienced R-INLA user, there are many other possible options for the INLA program. These can be specified in the `inla.options` list. The list objects `tcr.options`, `mu.options` and `ar1.options` are used to specify the settings of the Monte Carlo sampling scheme of the TCR, μ and the weights and first-lag autocorrelation hyperparameters associated with an aggregate AR(1) process if `model="ar1"`. The elements of `tcr.options` and `mu.options` list objects match the input arguments of the `inla.climate.tcr` and the `inla.climate.mu` functions which will be explained more thoroughly in the following subsections.

The `inla.climate` function returns an object of class `inla.climate`. This is a list object which contains all information obtained from the INLA fit. The arguments of this object include `hyperparam` which contains the

posterior marginal distributions and summary statistics of all model parameters. Another argument is `latent.field` which contains summary statistics of all latent variables, including those that correspond to the underlying AR(1) components. Time consumption (`time`) and model information criterias, such as the deviance information criteria (`dic`) and the log marginal-likelihood (`log.mlikelihood`), are also included in the `inla.climate` object. The return object from the `inla` function is also included as argument `inla.result`. If the TCR or μ is computed the relevant information is included in the `TCR` and `mu` arguments respectively.

Important information and summary statistics can be extracted from the return object and presented in a readable format using the `summary` function, and graphical results such as the posterior marginal density functions and TCR histogram can be displayed using the `plot` function. Below is an example of using the `inla.climate` function to fit the model to temperature and forcing generated by the GISS_E2_R earth system model (Schmidt et al., 2014).

```
data("GISS_E2_R")

result = inla.climate(GISS_E2_R$Temperature,
                     GISS_E2_R$Forcing)

summary(result)
plot(result)
```

A.2.4 Estimating the transient climate response

Inference about the transient climate response is obtained using Monte Carlo simulations. This procedure can be performed using the `inla.climate.tcr` function

```
inla.climate.tcr(result, Qco2, nsamples = 100000,
                 seed = 1234, print.progress = FALSE, model = "fgn")
```

Here, the two obligatory input variables are `result`, the return object obtained from the `inla.climate` function required here in order to sample from the joint hyperparameter posterior distribution, and `Qco2` which is the slope coefficient imposed on the forcing when assuming a gradual CO₂-doubling. `nsamples` denote the number of samples to be generated, and `seed` is the seed used for the random number generator. `print.progress` specify whether or not progress should be printed to the screen. The `model` input variable declare which noise model is assumed for the GMST model. If set equal to `"fgn"` or `"arfima"`, the TCR will be computed assuming a

scale-invariant response, while for `model="ar1"` it will be computed assuming a sum of exponentials response. In this case, the number of exponentials, m , is determined automatically from the number of hyperparameters in the `result` object.

The `inla.climate.tcr` function returns a list object of the same class as the `inla.climate` function where the results of the Monte Carlo sampling scheme is merged with the `result` input object. The information relevant to the TCR estimation procedure is included in the `tcr` argument of the return object.

Alternatively, the TCR can be computed directly in the `inla.climate` function by specifying a value for `Qco2` in the list of input arguments. The number of samples and the seed value is then specified through the `tcr.options` list. Below is an example of both approaches.

```
data("GISS_E2_R")

result = inla.climate(GISS_E2_R$Temperature,
                     GISS_E2_R$Forcing)

result.tcr1 = inla.climate.tcr(result, 3.8)

result.tcr2 = inla.climate(GISS_E2_R$Temperature,
                          GISS_E2_R$Forcing, Qco2 = 3.8)

summary(result.tcr1)
plot(result.tcr2)
```

A.2.5 Estimating the forced temperature response

As for the TCR, inference about the forced temperature response μ is obtained using Monte Carlo simulations. This can be accomplished using the `inla.climate.mu` function

```
inla.climate.mu(result, forcing, quick = FALSE,
                T0.corr = 0, nsamples = 100000, seed = 1234,
                print.progress = FALSE, model = "fgn")
```

Again, `result` is the return object from the `inla.climate` function. We also need the `forcing` data array describing the known radiative forcing. The `T0.corr` variable denotes the temperature shift. If this is equal to the intercept term T_0 in equation (4.2) the results will be aligned with the temperature observations. Similar to the TCR, the `model` input variable determines which noise model is in use and whether or not to use a scale-invariant response of a sum of exponential response.

Since this function produces and stores full Bayesian inference of all marginal variables of the mean vector instead of a single composite variable this sampling scheme will be far more costly than that of the TCR. Memory consumption is particularly demanding as the number of samples (`nsamples`) can be quite high. If the user is only concerned with the posterior marginal means or standard deviations it is possible to specify that the function should not store the individual samples by setting `quick = TRUE`.

The function returns a list object of the same class as the `inla.climate` function where the results of the Monte Carlo sampling scheme is merged with the `result` input object. The information relevant for the known forcing response is included in the `mu` argument of the return object.

The mean vector can also be computed directly from the `inla.climate` function by setting the `compute.mu` input variable equal to 2 or "full" for a complete analysis, or 1 or "quick" for the faster and less memory intensive approach. The number of samples, seed value and the temperature shift value T_0 is specified through the `mu.options` list. The example below shows both approaches.

```
data("GISS_E2_R")

result = inla.climate(GISS_E2_R$Temperature,
                     GISS_E2_R$Forcing)

T0 = mean(GISS_E2_R$Temperature[1:20])

result.mu1 = inla.climate.mu(result, GISS_E2_R$Forcing,
                             quick = FALSE,
                             T0.corr = T0)

result.mu2 = inla.climate(GISS_E2_R$Temperature,
                          GISS_E2_R$Forcing,
                          compute.mu = "full")

summary(result.mu1)
plot(result.mu2)
```

A.3 Troubleshooting

The most recurring problem with this package is that the numerical optimization algorithm within the INLA program fails to find a reasonable solution or crashes altogether. This can often be solved by tuning the `stepLength` input parameter. If the INLA program finds a solution, but you suspect

A.3 – Troubleshooting

it may have been trapped in a local solution and not a global one adding `restart.inla` might also help. For an updated list of ongoing problems with the package see www.github.com/eirikmn/INLA.climate/issues. If you encounter an issue with the package or have suggestions for future implementation please send me an email at eirikmn91@gmail.com.

Bibliography

- Baillie, R. T. (1996). Long memory processes and fractional integration in econometrics. *Journal of Econometrics*, 73(1), 5–59. DOI: 10.1016/0304-4076(95)01732-1.
- Baillie, R. and S.-K. Chung (2002). Modeling and forecasting from trend-stationary long memory models with applications to climatology. *International Journal of Forecasting*, 18, 215–226. DOI: 10.1016/S0169-2070(01)\linebreak00154-6.
- Bakka, H., H. Rue, G.-A. Fuglstad, A. Riebler, D. Bolin, J. Illian, E. Krainski, D. Simpson and F. Lindgren (2018). Spatial modeling with R-INLA: A review. *WIREs Computational Statistics*, 10(6), e1443. DOI: 10.1002/wics.1443.
- Bakka, H., J. Vanhatalo, J. B. Illian, D. Simpson and H. Rue (2019). Non-stationary Gaussian models with physical barriers. *Spatial Statistics*, 29, 268–288. DOI: 10.1016/j.spasta.2019.01.002.
- Beran, J. (1994). *Statistics for Long-Memory Processes*. 1st ed. Chapman & Hall/CRC, New York, NY, USA. ISBN: 0412049015.
- Beran, J., Y. Feng, S. Ghosh and R. Kulik (2013). *Long-Memory Processes - Probabilistic Properties and Statistical Methods*. Springer, Heidelberg, Germany. ISBN: 3642355110.
- Bhattacharya, R. N., V. K. Gupta and E. Waymire (1983). The Hurst effect under trends. *Journal of Applied Probability*, 20(3), 649–662. DOI: 10.2307/3213900.
- Blangiardo, M. and M. Cameletti (2015). *Spatial and Spatio-temporal Bayesian models with R-INLA*. John Wiley & Sons, West Sussex, UK. ISBN: 978-1-118-32655-8.
- Blangiardo, M., M. Cameletti, G. Baio and H. Rue (2013). Spatial and spatio-temporal models with R-INLA. *Spatial and Spatio-temporal Epidemiology*, 4, 33–49. DOI: 10.1016/j.sste.2012.12.001.
- Box, G. E. P., G. M. Jenkins, G. C. Reinsel and G. M. Ljung (2016). *Time Series Analysis, Forecasting and Control*. 5th ed. John Wiley & Sons, Hoboken, NJ, USA. ISBN: 978-1-118-67502-1. DOI: 10.2307/2284112.

BIBLIOGRAPHY

- Cameletti, M., F. Lindgren, D. Simpson and H. Rue (2013). Spatio-temporal modeling of particulate matter concentration through the SPDE approach. *AStA Advances in Statistical Analysis*, 97(2), 109–131. DOI: 10.1007/s10182-012-0196-3.
- Clarke, L., J. Edmonds, H. Jacoby, H. Pitcher, J. Reilly and R. Richels (2007). *Scenarios of Greenhouse Gas Emissions and Atmospheric Concentrations*. sub-report 2.1A. Sub-report 2.1A of Synthesis and Assessment Product 2.1 by the U.S. Climate Change Science Program and the Subcommittee on Global Change Research. Department of Energy, Office of Biological & Environmental Research, Washington DC. US department of Energy Publications.
- Cressie, N. and H.-C. Huang (1999). Classes of Nonseparable, Spatio-Temporal Stationary Covariance Functions. *Journal of the American Statistical Association*, 94(448), 1330–1339. DOI: 10.1080/01621459.1999.10473885.
- Diebold, F. X. and A. Inoue (2001). Long memory and regime switching. *Journal of Econometrics*, 105(1). Forecasting and empirical methods in finance and macroeconomics, 131–159. DOI: 10.1016/S0304-4076(01)00073-2.
- Durbin, J. (1960). The fitting of time-series models. *Review of the International Statistical Institute*, 28(3), 233–244. DOI: 10.2307/1401322.
- Feller, W. (1951). The Asymptotic Distribution of the Range of Sums of Independent Random Variables. *The Annals of Mathematical Statistics*, 22(3), 427–432.
- Forster, P. M., T. Andrews, P. Good, J. M. Gregory, L. S. Jackson and M. Zelinka (2013). Evaluating adjusted forcing and model spread for historical and future scenarios in the CMIP5 generation of climate models. *Journal of Geophysical Research: Atmospheres*, 118(3), 1139–1150. DOI: 10.1002/jgrd.50174.
- Franzke, C. (2010). Long-Range Dependence and Climate Noise Characteristics of Antarctic Temperature Data. *Journal of Climate*, 23(22), 6074–6081. DOI: 10.1175/2010JCLI3654.1.
- (2012). Nonlinear Trends, Long-Range Dependence, and Climate Noise Properties of Surface Temperature. *Journal of Climate*, 25(12), 4172–4183. DOI: 10.1175/JCLI-D-11-00293.1.
- Franzke, C., S. M. Osprey, P. Davini and N. W. Watkins (2015). A Dynamical Systems Explanation of the Hurst Effect and Atmospheric Low-Frequency Variability. *Scientific Reports*, 5, 9068. DOI: 10.1038/srep09068.
- Fredriksen, H.-B. and K. Rypdal (2016). Spectral characteristics of instrumental and climate model surface temperatures. *Journal of Climate*, 29(4), 1253–1268. DOI: 10.1175/JCLI-D-15-0457.1.

BIBLIOGRAPHY

- Fredriksen, H.-B. and M. Rypdal (2017). Long-Range Persistence in Global Surface Temperatures Explained by Linear Multibox Energy Balance Models. *Journal of Climate*, 30(18). DOI: 10.1175/JCLI-D-16-0877.1.
- Fuglstad, G.-A., I. Hem, A. Knight, H. Rue and A. Riebler (2019). Intuitive Joint Priors for Variance Parameters. *Bayesian Analysis*. DOI: 10.1214/19-BA1185.
- Fujino, J., R. Nair, M. Kainuma, T. Masui and Y. Matsuoka (2006). Multi-gas Mitigation Analysis on Stabilization Scenarios Using Aim Global Model. *The Energy Journal*, 27, 343–353. DOI: 10.5547/ISSN0195-6574-EJ-Vo1SI2006-NoSI3-17.
- Gamerman, D. and H. Lopes (2006). *Markov chain Monte Carlo: Stochastic simulation for Bayesian inference*. 2nd ed. Chapman & Hall/CRC, New York, NY, USA. DOI: 10.1201/9781482296426.
- GISTEMP Team (2018). *GISS Surface Temperature Analysis (GISTEMP)*. Version 4. NASA Goddard Institute for Space Studies. Dataset accessed 2018-08-29 at <https://data.giss.nasa.gov/gistemp>.
- Gneiting, T. (2002). Nonseparable, stationary covariance functions for space-time data. *Journal of the American Statistical Association*, 97(458), 590–600. DOI: 10.1198/016214502760047113.
- Golub, G. and C. V. Loan (1996). *Matrix Computations*. 3rd ed. Johns Hopkins University Press, Baltimore, MD, USA, p. 784. ISBN: 1421407949.
- Granger, C. W. J. (1978). New Classes of Time Series Models. *Journal of the Royal Statistical Society, Series D*, 27(3/4), 237–253. DOI: 10.2307/2988186.
- (1980). Long memory relationships and the aggregation of dynamic models. *Journal of Econometrics*, 14(2), 227–238. DOI: 10.1016/0304-4076(80)90092-5.
- Granger, C. W. J. and M. J. Morris (1976). Time Series Modelling and Interpretation. *Journal of the Royal Statistical Society, Series B*, 139(2), 246–257. DOI: 10.2307/2345178.
- Granger, C. and R. Joyeux (1980). An introduction to long-memory time series models and fractional differencing. *Journal of Time Series Analysis*, 1(1), 15–29. DOI: 10.1111/j.1467-9892.1980.tb00297.x.
- Graves, T., R. B. Gramacy, C. L. E. Franzke and N. W. Watkins (2015). Efficient Bayesian inference for natural time series using ARFIMA processes. *Nonlinear Processes in Geophysics*, 22(6), 679–700. DOI: 10.5194/npg-22-679-2015.
- Graves, T., R. Gramacy, N. Watkins and C. Franzke (2017). A brief history of long memory: Hurst, Mandelbrot and the road to ARFIMA, 1951-1980. *Entropy*, 19(9), 437. DOI: 10.3390/e19090437.

BIBLIOGRAPHY

- Gregory, J., W. Ingram, M. Palmer, G. Jones, P. Stott, R. Thorpe, J. Lowe, T. Johns and K. Williams (2004). A new method for diagnosing radiative forcing and climate sensitivity. *Geophysical Research Letters*, 31(3), L03205. DOI: 10.1029/2003GL018747.
- Guegán, D. (2005). How can we Define the Concept of Long Memory? An Econometric Survey. *Econometric Reviews*, 24(2), 113–149. DOI: 10.1081/ETC-200067887.
- Haldrup, N. and J. E. V. Valdés (2017). Long memory, fractional integration and cross-sectional aggregation. *Journal of Econometrics*, 199(1), 1–11. DOI: 10.1016/j.jeconom.2017.03.001.
- Hambly, B. and A. Søjmark (2018). An SPDE Model for Systemic Risk with Endogenous Contagion. *Finance and Stochastics*, 535–594. DOI: 10.1007/s00780-019-00396-1.
- Hansen, J., M. Sato, P. Kharecha and K. von Schuckmann (2011). Earth’s energy imbalance and implications. *Atmospheric Chemistry and Physics*, 11(24), 13421–13449. DOI: 10.5194/acp-11-13421-2011.
- Haslett, J. and A. E. Raftery (1989). Space-Time Modelling with Long-Memory Dependence: Assessing Ireland’s Wind Power Resource. *Journal of the Royal Statistical Society, Series C*, 38(1), 1–50. DOI: 10.2307/2347679.
- Hijioka, Y., Y. Matsuoka, H. Nishimoto, T. Masui and M. Kainuma (2008). Global GHG emissions scenarios under GHG concentration stabilization targets. *Journal of Global Environmental Engineering*, 13, 97–108.
- Hosking, J. R. M. (1981). Fractional Differencing. *Biometrika*, 68(1), 165–176. DOI: 10.2307/2335817.
- Huang, J., P. Shang and X. Zhao (2012). Multifractal diffusion entropy analysis on stock volatility in financial markets. *Physica A: Statistical Mechanics and its Applications*, 391(22), 5739–5745. DOI: 10.1016/j.physa.2012.06.039.
- Huang, J., B. P. Malone, B. Minasny, A. B. McBratney and J. Triantafyllis (2017). Evaluating a Bayesian modelling approach (INLA-SPDE) for environmental mapping. *Science of The Total Environment*, 609, 621–632. DOI: 10.1016/j.scitotenv.2017.07.201.
- Hurst, H. E. (1951). Long-term storage capacity of reservoirs. *Transactions of American Society of Civil Engineers*, 116, 770–799.
- Huybers, P. and W. Curry (2006). Links between annual, Milankovitch and continuum temperature variability. *Nature*, 441, 329–332. DOI: 10.1038/nature04745.
- IPCC (2013). Summary for Policymakers. *Climate Change 2013: The Physical Science Basis. Contribution of Working Group I to the Fifth Assessment Report of the Intergovernmental Panel on Climate Change*. Ed. by T. Stocker, D. Qin, G.-K. Plattner, M. Tignor, S. Allen, J. Boschung,

BIBLIOGRAPHY

- A. Nauels, Y. Xia, V. Bex and P. Midgley. Cambridge, United Kingdom and New York, NY, USA: Cambridge University Press, New York, NY, USA. Chap. SPM, pp. 1–30. ISBN: 978-1-107-66182-0.
- Jiang, W., L. Yuan, W. Wang, R. Cao, Y. Zhang and W. Shen (2014). Spatio-temporal analysis of vegetation variation in the Yellow River Basin. *Ecological Indicators*, 51, 117–126. DOI: 10.1016/j.ecolind.2014.07.031.
- Kolmogorov, A. N. (1940). Wiener'sche Spiralen und einige andere interessante Kurven im Hilbertschen Raum. (German) [Wiener's spiral and some other interesting curves in Hilbert space]. *Proceedings of the USSR Academy of Sciences*, 26(2), 115–118.
- (1941). Dissipation of energy in a locally isotropic turbulence. *Proceedings of the USSR Academy of Sciences*, 32, 16–18.
- Koutsoyiannis, D. (2003). Climate change, the Hurst phenomenon, and hydrological statistics. *Hydrological Sciences Journal*, 48(1), 3–24. DOI: 10.1623/hysj.48.1.3.43481.
- Krainski, E. T. (2018). Statistical analysis of space-time data: New models and applications. PhD thesis. Norwegian University of Science and Technology, Trondheim.
- Krainski, E., V. Gómez Rubio, H. Bakka, A. Lenzi, D. Castro-Camilo, D. Simpson, F. Lindgren and H. Rue (2018). *Advanced Spatial Modeling with Stochastic Partial Differential Equations Using R and INLA*. 1st ed. Chapman & Hall/CRC, New York, NY, USA, p. 298. DOI: 10.1201/9780429031892.
- Kyaw, N. A., C. A. Los and S. Zong (2006). Persistence characteristics of Latin American financial markets. *Journal of Multinational Financial Management*, 16(3), 269–290. DOI: 10.1016/j.mulfin.2005.08.001.
- Lenssen, N., G. Schmidt, J. Hansen, M. Menne, A. Persin, R. Ruedy and D. Zyss (2019). Improvements in the GISTEMP uncertainty model. *Journal of Geophysical Research: Atmosphere*, 124(12), 6307–6326. DOI: 10.1029/2018JD029522.
- Levinson, N. (1947). The Wiener (Root Mean Square) error criterion in filter design and prediction. *Journal of Mathematics and Physics*, 25(1-4), 261–278. DOI: 10.1002/sapm1946251261.
- Lindgren, F., H. Rue and J. Lindström (2011). An explicit link between Gaussian fields and Gaussian Markov random fields: The stochastic partial differential equation approach. *Journal of the Royal Statistical Society, Series B*, 73(4), 423–498. DOI: 10.1111/j.1467-9868.2011.00777.x.
- Lovejoy, S. and D. Schertzer (2013). *The Weather and Climate: Emergent Laws and Multifractal Cascades*. Cambridge University Press, Cambridge, UK, p. 505. ISBN: 1107018986. DOI: 10.1017/CB09781139093811.

BIBLIOGRAPHY

- Løvsletten, O. and M. Rypdal (2016). Statistics of Regional Surface Temperatures after 1900: Long-Range versus Short-Range Dependence and Significance of Warming Trends. *Journal of Climate*, 29(11), 4057–4068. DOI: 10.1175/JCLI-D-15-0437.1.
- Makarava, N., S. Benmehdi and M. Holschneider (2011). Bayesian estimation of self-similarity exponent. *Physical Review E*, 84(2 Pt 1), 021109.
- Mandelbrot, B. and J. van Ness (1968). Fractional Brownian motions, fractional noises and applications. *SIAM Review*, 18(4), 1088–1107. DOI: 10.1137/1010093.
- Mandelbrot, B. and J. R. Wallis (1968). Noah, Joseph, and Operational Hydrology. *Water Resources Research*, 4(5), 909–918. DOI: 10.1029/WR004i005p00909.
- Myrvoll-Nilsen, E. (2016). Computationally efficient Bayesian approximation of fractional Gaussian noise using AR1 processes. MA thesis. Norwegian University of Science and Technology, Trondheim.
- Myrvoll-Nilsen, E., H.-B. Fredriksen, S. H. Sørbye and M. Rypdal (2019a). Warming trends and long-range dependent climate variability since year 1900: a Bayesian approach. *Frontiers in Earth Science*, 7, 214. DOI: 10.3389/feart.2019.00214.
- Myrvoll-Nilsen, E., S. H. Sørbye, H.-B. Fredriksen, H. Rue and M. Rypdal (2019b). Statistical estimation of global surface temperature response to forcing under the assumption of temporal scaling. *Earth System Dynamics Discussions*, 2019. Preprint, 1–28. DOI: 10.5194/esd-2019-66.
- Peng, C.-K., S. V. Buldyrev, S. Havlin, M. Simons, H. E. Stanley and A. L. Goldberger (1994). Mosaic organization of DNA nucleotides. *Physical Review E*, 49(2), 1685–1689. DOI: 10.1103/PhysRevE.49.1685.
- Purczyński, J. and P. Włodarski (2006). On fast generation of fractional Gaussian noise. *Computational Statistics & Data Analysis*, 50(10), 2537–2551. DOI: 10.1016/j.csda.2005.04.021.
- Rao, S. and K. Riahi (2006). The Role of Non-CO2 Greenhouse Gases in Climate Change Mitigation: Long-term Scenarios for the 21st Century. *The Energy Journal*, 27, 177–200.
- Riahi, K., A. Grübler and N. Nakicenovic (2007). Scenarios of long-term socio-economic and environmental development under climate stabilization. *Technological Forecasting and Social Change*, 74(7). Greenhouse Gases - Integrated Assessment, 887–935. DOI: 10.1016/j.techfore.2006.05.026.
- Robert, C. and G. Casella (1999). *Monte Carlo Statistical Methods*. 1st ed. Springer-Verlag, New York, NY, USA. ISBN: 978-1-4757-3071-5.
- Rodriguez-Iturbe, I., J. M. Mejia and D. R. Dawdy (1972). Streamflow Simulation: 1. A new look at Markovian Models, fractional Gaussian

BIBLIOGRAPHY

- noise, and Crossing Theory. *Water Resources Research*, 8(4), 921–930. DOI: 10.1029/WR008i004p00921.
- Rue, H. and L. Held (2005). *Gaussian Markov Random Fields: Theory And Applications (Monographs on Statistics and Applied Probability)*. 1st ed. Chapman & Hall/CRC, New York, NY, USA, p. 280. ISBN: 1584884320.
- Rue, H., S. Martino and N. Chopin (2009). Approximate Bayesian inference for latent Gaussian models by using integrated nested Laplace approximations. *Journal of the Royal Statistical Society, Series B*, 71(2), 319–392. DOI: 10.1111/j.1467-9868.2008.00700.x.
- Rue, H. (2001). Fast sampling of Gaussian Markov random fields. *Journal of the Royal Statistical Society, Series B*, 63(2), 325–338. DOI: 10.1111/1467-9868.00288.
- Rybski, D., A. Bunde, S. Havlin and H. von Storch (2006). Long-term persistence in climate and the detection problem. *Geophysical Research Letters*, 33(6), L06718–L06718. DOI: 10.1029/2005GL025591.
- Rypdal, K., L. Østvand and M. Rypdal (2013). Long-Range memory in Earth’s surface temperature on time scales from months to centuries. *Journal of Geophysical Research: Atmospheres*, 118, 7046–7062. DOI: 10.1002/jgrd.50399.
- Rypdal, M. and K. Rypdal (2016). Late Quaternary temperature variability described as abrupt transitions on a $1/f$ noise background. *Earth System Dynamics*, 7(1), 281–293. DOI: 10.5194/esd-7-281-2016.
- Rypdal, M., H.-B. Fredriksen, E. Myrvoll-Nilsen, K. Rypdal and S. H. Sørbye (2018). Emergent Scale Invariance and Climate Sensitivity. *Climate*, 6(4). DOI: 10.3390/cli6040093.
- Schmidt, G. A., M. Kelley, L. Nazarenko, R. Ruedy, G. L. Russell, I. Aleinov, M. Bauer, S. E. Bauer, M. K. Bhat, R. Bleck, V. Canuto, Y.-H. Chen, Y. Cheng, T. L. Clune, A. Del Genio, R. de Fainchtein, G. Faluvegi, J. E. Hansen, R. J. Healy, N. Y. Kiang, D. Koch, A. A. Lacis, A. N. LeGrande, J. Lerner, K. K. Lo, E. E. Matthews, S. Menon, R. L. Miller, V. Oinas, A. O. Oloso, J. P. Perlwitz, M. J. Puma, W. M. Putman, D. Rind, A. Romanou, M. Sato, D. T. Shindell, S. Sun, R. A. Syed, N. Tausnev, K. Tsigaridis, N. Unger, A. Voulgarakis, M.-S. Yao and J. Zhang (2014). Configuration and assessment of the GISS ModelE2 contributions to the CMIP5 archive. *Journal of Advances in Modeling Earth Systems*, 6(1), 141–184. DOI: 10.1002/2013MS000265.
- Simonsen, I. (2003). Measuring anti-correlations in the nordic electricity spot market by wavelets. *Physica A: Statistical Mechanics and its Applications*, 322, 597–606. DOI: 10.1016/S0378-4371(02)01938-6.

BIBLIOGRAPHY

- Simpson, D., H. Rue, A. Riebler, T. G. Martins and S. H. Sørbye (2017). Penalising model component complexity: A principled, practical approach to constructing priors. *Statistical Science*, 32(1), 1–28. DOI: 10.1214/16-STS576.
- Smith, S. J. and T. Wigley (2006). Multi-Gas Forcing Stabilization with Minicam. *The Energy Journal*, 27, 373–391. DOI: 10.5547/ISSN0195-6574-EJ-VolSI2006-NoSI3-19.
- Sørbye, S. H., E. Myrvoll-Nilsen and H. Rue (2019). An approximate fractional Gaussian noise model with $\mathcal{O}(n)$ computational cost. *Statistics and Computing*, 29, 821–833. DOI: 10.1007/s11222-018-9843-1.
- Sørbye, S. H. and H. Rue (2017). Fractional Gaussian noise: Prior specification and model comparison. *Environmetrics*, 29(5-6), e2457. DOI: 10.1002/env.2457.
- Taqqu, M. S. (2003). Fractional Brownian motion and long-range dependence. *Theory and applications of long-range dependence*. Ed. by P. Doukhan, G. Oppenheim and M. S. Taqqu. Birkhäuser Boston, MA, USA, pp. 5–38.
- (2013). B. Mandelbrot and Fractional Brownian motion. *Statistical Science*, 28(1), 131–134. DOI: 10.1214/12-STS389.
- Taqqu, M. S., V. Teverovsky and W. Willinger (1995). Estimators for Long-Range Dependence: An Empirical Study. *Fractals*, 3(04), 785–798. DOI: 10.1142/S0218348X95000692.
- Telesca, L. and M. Lovallo (2010). Long-range dependence in tree-ring width time series of Austrocedrus Chilensis revealed by means of the detrended fluctuation analysis. *Physica A: Statistical Mechanics and its Applications*, 389(19), 4096–4104. DOI: 10.1016/j.physa.2010.05.031.
- Tousson, O. (1925). Mémoire sur l’Histoire du Nil. Mémoire de l’Institut d’Egypte.
- Trench, W. F. (1964). An algorithm for the inversion of finite Toeplitz matrices. *Journal of the Society for Industrial and Applied Mathematics*, 12(3), 515–522. DOI: 10.1137/0112045.
- Tudor, C. A. (2013). Fractional Brownian Motion and Related Processes. *Analysis of Variations for Self-similar Processes: A Stochastic Calculus Approach*. Springer International Publishing, Cham, Switzerland, pp. 3–25. ISBN: 978-3-319-00936-0. DOI: 10.1007/978-3-319-00936-0_1.
- Van Vuuren, D., B. Eickhout, P. Lucas and M. den Elzen (2006). Long-Term Multi-Gas Scenarios to Stabilise Radiative Forcing — Exploring Costs and Benefits Within an Integrated Assessment Framework. *The Energy Journal*, 27, 201–233. DOI: 10.2307/23297082.
- Van Vuuren, D. P., M. G. J. den Elzen, P. L. Lucas, B. Eickhout, B. J. Strengers, B. van Ruijven, S. Wonink and R. van Houdt (2007). Stabilizing greenhouse gas concentrations at low levels: an assessment of

BIBLIOGRAPHY

- reduction strategies and costs. *Climatic Change*, 81(2), 119–159. DOI: 10.1007/s10584-006-9172-9.
- Vlahogianni, E. I., M. G. Karlaftis and J. C. Golias (2007). Spatio-Temporal Short-Term Urban Traffic Volume Forecasting Using Genetically Optimized Modular Networks. *Computer-Aided Civil and Infrastructure Engineering*, 22(5), 317–325. DOI: 10.1111/j.1467-8667.2007.00488.x.
- Weron, R. and B. Przybyłowicz (2000). Hurst analysis of electricity price dynamics. *Physica A: Statistical Mechanics and its Applications*, 283(3), 462–468. DOI: 10.1016/S0378-4371(00)00231-4.
- Whittle, P. (1951). *Hypothesis testing in times series analysis*. Almqvist & Wiksells Boktryckeri AB, Uppsala, Sweden.
- (1954). On stationary processes in the plane. *Biometrika*, 41(3-4), 434–449. DOI: 10.1093/biomet/41.3-4.434.
- (1963). Stochastic processes in several dimensions. *Bulletin of the International Statistical Institute*, 40(2), 974–994.
- Wise, M., K. Calvin, A. Thomson, L. Clarke, B. Bond-Lamberty, R. Sands, S. J. Smith, A. Janetos and J. Edmonds (2009). Implications of Limiting CO₂ Concentrations for Land Use and Energy. *Science*, 324(5931), 1183–1186. DOI: 10.1126/science.1168475.

Paper I

An approximate fractional Gaussian noise model with $\mathcal{O}(n)$ computational cost

Statistics and Computing, **29**, 821–833, 2019.



An approximate fractional Gaussian noise model with $\mathcal{O}(n)$ computational cost

Sigrunn H. Sørbye¹ · Eirik Myrvoll-Nilsen¹ · Håvard Rue²

Received: 4 July 2018 / Accepted: 13 November 2018 / Published online: 16 November 2018
© Springer Science+Business Media, LLC, part of Springer Nature 2018

Abstract

Fractional Gaussian noise (fGn) is a stationary time series model with long-memory properties applied in various fields like econometrics, hydrology and climatology. The computational cost in fitting an fGn model of length n using a likelihood-based approach is $\mathcal{O}(n^2)$, exploiting the Toeplitz structure of the covariance matrix. In most realistic cases, we do not observe the fGn process directly but only through indirect Gaussian observations, so the Toeplitz structure is easily lost and the computational cost increases to $\mathcal{O}(n^3)$. This paper presents an approximate fGn model of $\mathcal{O}(n)$ computational cost, both with direct and indirect Gaussian observations, with or without conditioning. This is achieved by approximating fGn with a weighted sum of independent first-order autoregressive (AR) processes, fitting the parameters of the approximation to match the autocorrelation function of the fGn model. The resulting approximation is stationary despite being Markov and gives a remarkably accurate fit using only four AR components. Specifically, the given approximate fGn model is incorporated within the class of latent Gaussian models in which Bayesian inference is obtained using the methodology of integrated nested Laplace approximation. The performance of the approximate fGn model is demonstrated in simulations and two real data examples.

Keywords Autoregressive process · Gaussian Markov random field · Integrated nested Laplace approximation · Long-range dependence · Toeplitz matrix

1 Introduction

Many natural processes observed in either time or space exhibit a long-range dependency structure, here referred to as long memory. One way to characterize long memory is in terms of the autocorrelation function having a slower than exponential decay as a function of increasing temporal or geographical distance between observational points. In second-order stationary time series, long memory implies that the autocorrelations are not absolutely summable (McLeod and Hipel 1978). Long-memory behaviour has been observed within a vast variety of time series applications, like hydrology (Hurst 1951; Hosking 1984), geophysical time series (Mandelbrot and Wallis 1969b), network traffic modelling (Willinger et al. 1996), econometrics (Bail-

lie 1996; Cont 2005) and climate data analysis (Franzke 2012; Rypdal and Rypdal 2014). For comprehensive introductions to long-memory processes and their applications, see for example Doukhan et al. (2003) and Beran et al. (2013).

When introduced in Mandelbrot and Van Ness (1968), fractional Brownian motion (fBm) represented a first paradigmatic example of a long-memory model. The fBm is a time-continuous Gaussian process which generalizes ordinary Brownian motion to allow for dependent increments. A unique property of fBm is that it is exactly self-similar and its long-memory properties are characterized by the self-similarity parameter H , also named the Hurst exponent. Of specific interest is the discrete-time increment process of fBm, referred to as fractional Gaussian noise (fGn). This was the first stationary Gaussian process which could explain the famous Hurst phenomenon (Hurst 1951). Since its introduction, the fGn process has been applied in a variety of applications ranging from hydrology (Molz et al. 1997), analysis of functional magnetic resonance images (Maxim et al. 2005) and climate analysis (Rypdal and Rypdal 2014).

Inheriting the parsimonious parameterization of fBm, the autocorrelation function of fGn is fully specified as a function

✉ Sigrunn H. Sørbye
sigrunn.sorbye@uit.no

¹ Department of Mathematics and Statistics, UiT The Arctic University of Norway, 9037 Tromsø, Norway

² CEMSE Division, King Abdullah University of Science and Technology, Thuwal 23955-6900, Saudi Arabia

of H and the model has long memory when $1/2 < H < 1$. Exploiting the Toeplitz structure of the covariance matrix, the computational cost of likelihood-based inference in fitting an fGn process of length n is $\mathcal{O}(n^2)$, making use of the Durbin–Levinson or Trench algorithms (Levinson 1947; Durbin 1960; Trench 1964; Golub and Loan 1996; McLeod et al. 2007). However, the required Toeplitz structure is fragile to modifications of the Gaussian observational model and computations of conditional distributions. For example, the Toeplitz structure is destroyed if fGn is observed indirectly with Gaussian inhomogeneous noise, or has missing data. In these situations, the computational cost of likelihood-based inference would increase to $\mathcal{O}(n^3)$.

This paper presents an accurate and computationally efficient approximate fGn model of cost $\mathcal{O}(n)$, both with direct and indirect Gaussian observations, with or without additional conditioning. This allows for routinely use of fGn models with large n , with negligible loss of accuracy. The new approximate model uses a weighted sum of independent first-order autoregressive processes (AR(1)). The motivation is that aggregation of short-memory processes plays an important role to explain long-memory behaviour in time series (Beran et al. 2010) and an infinite weighted sum of AR(1) processes will give long memory (Granger 1980). In practice, the number of aggregated processes might need to be rather large to reflect the underlying long-memory parameter (Haldrup and Valdés 2017). However, the new approximate fGn model only needs a weighted sum of four AR(1) processes to be accurate. This is obtained by fitting the weights and the coefficients of the AR(1) processes to mimic the autocorrelation function of the exact fGn model, as a continuous function of H .

A key feature of the approximate fGn model is a high degree of conditional independence within the model. Specifically, the approximate model will be represented as a Gaussian Markov random field (GMRF), the computational properties of which are not destroyed by indirect Gaussian observations nor conditioning (Rue and Held 2005). The approximate model is also stationary, a desired property which is not common among GMRFs as they typically have boundary effects. Since the approximate model is a local GMRF, it also fits well within the framework of latent Gaussian models for which approximate Bayesian analysis is obtained with integrated nested Laplace approximations (INLA) (Rue et al. 2009) using the R-package R-INLA (<http://www.r-inla.org>). This provides a flexible modelling framework in which the approximate fGn model can be combined with for example time trends, linear and non-linear covariate effects and other random effects to build realistically complex models for observed time series. A different aspect is that an aggregated model of a few AR(1) components could actually represent a more plausible and interpretable model than the theoretical fGn process in real

data applications. Specifically, the approximate model can serve as a tool for automatic source separation in situations where the data at hand represent combined signals. Among others, this can be useful in climate data analysis in which a weighted sum of Ornstein–Uhlenbeck processes has been linked with multibox energy balance models (Fredriksen and Rypdal 2017).

A flexible alternative in modelling long-memory processes is to use the framework of autoregressive fractionally integrated moving average (ARFIMA) models (Granger and Joyeux 1980; Hosking 1981). These models represent a natural extension of the classical ARIMA models (Box and Jenkins 1980) and can be used to model both short- and long-range dependency structures simultaneously. If the order of the autoregressive (AR) and moving average (MA) parts are both 0, the resulting ARFIMA(0, d , 0) model has very similar properties to fGn when the long-memory parameter $d = H - 0.5$. Both of these models exhibit the same hyperbolic decay of the autocorrelation function. A conceptual distinction between these two models is that fGn can be considered as a discrete approximation to the fractional derivative of the time-continuous Brownian motion (Hosking 1981). In contrast, AFRIMA(0, d , 0) is obtained by fractional differencing of the ARIMA(0, 1, 0) model which is by definition discrete. This natural extension of ARIMA(0, 1, 0) can be seen as an advantage of ARFIMA(0, d , 0) models compared with fGn (Graves et al. 2017). On the other hand, many asymptotic relations of fGn processes also hold for finite samples (Taqqu et al. 1995) and fGn-based models are very popular due to their analytic tractability (Purczyński and Włodarski 2006).

This paper focuses on approximating fGn but as demonstrated in Sect. 3.4 the same method can be used to approximate ARFIMA(0, d , 0) models. We note that by using algorithms based on the fast Fourier transform, ARFIMA models can be fitted with $\mathcal{O}(n \log(n))$ computational cost when the process is observed directly (Jensen and Nielsen 2014). The fast Fourier transform can also be used to give a computationally efficient infinite sum approximation of fGn, reducing the computational cost of the Whittle estimator (Purczyński and Włodarski 2006). Chan and Palma (2006) gives a review of different likelihood-based methods to fit ARFIMA models. These include an approximate state-space algorithm using the Kalman filter, which can also be modified to analyse time series with missing data (Palma and Chan 1997). The approximation uses a truncated state-space approach, representing the ARFIMA model by a moving average process with $M \approx 30$ terms. The general cost of this algorithm is $\mathcal{O}(nM^3)$, including n updates and inversion of $M \times M$ matrices. Knorr-Held and Rue (2002) describe a general GMRF framework which includes state-space models for time series. They describe the relation between the Kalman filter and a Cholesky factor approach, stating that

the latter is both conceptually simpler and computationally more efficient as calculations are done only once for a band matrix of dimension nM .

The presented approach takes advantage of both the GMRF framework (Rue and Held 2005) and the Cholesky factorization (Rue 2001; Knorr-Held and Rue 2002) to provide the approximate fGn model using a truncation with only four terms. The plan of this paper is as follows. Section 2 reviews the computational cost in fitting the exact fGn model to direct and indirect Gaussian observations. Section 3 presents the new approximate fGn model and derives the computational cost and memory requirement for evaluating the log-likelihood. The performance of the approximate model is demonstrated by simulations in Sect. 4, also including a study of its predictive properties. In Sect. 5, we use the implicit source separation ability in decomposing the historical dataset of annual water level minima for the Nile river (Toussoun 1925; Beran 1994). Implementation within the class of latent Gaussian models is demonstrated by analysing a monthly mean surface air temperature series for Central England (Manley 1953, 1974; Parker et al. 1992). For comparison, we also include results using the approximate ARFIMA(0, d , 0) model for these two datasets. Concluding remarks are given in Sect. 6.

2 The computational cost of fGn

Let $\mathbf{x} = (x_1, \dots, x_n)^T$ be a zero-mean fGn process, $\mathbf{x} \sim \mathcal{N}_n(\mathbf{0}, \boldsymbol{\Sigma})$. The elements of the covariance matrix, $\Sigma_{ij} = \sigma^2 \gamma_x(k)$ where $k = |i - j|$, are defined by the autocorrelation function

$$\gamma_x(k) = \frac{1}{2} (|k - 1|^{2H} - 2|k|^{2H} + |k + 1|^{2H}), \quad k = 0, 1, \dots, n - 1.$$

This function has a hyperbolic decay, $\gamma_x(k) \sim H(2H - 1)k^{2(H-1)}$ as $k \rightarrow \infty$. The fGn process is persistent when $1/2 < H < 1$, while it reduces to white noise when $H = 1/2$. When $0 < H < 1/2$, the fGn model has anti-persistent properties, but we do not discuss this case here.

When fGn is observed directly, we estimate H by maximizing the log-likelihood function

$$\log(\pi(\mathbf{x})) = -\frac{n}{2} \log(2\pi) + \frac{1}{2} \log |\mathbf{Q}| - \frac{1}{2} \mathbf{x}^T \mathbf{Q} \mathbf{x},$$

where $\mathbf{Q} = \boldsymbol{\Sigma}^{-1}$ is the precision matrix of \mathbf{x} . Making use of the Toeplitz structure of $\boldsymbol{\Sigma}$, the likelihood is evaluated in $\mathcal{O}(n^2)$ flops using the Durbin–Levinson algorithm (Golub and Loan 1996, Algorithm 4.7.2). Also, the precision matrix \mathbf{Q} can be calculated in $\mathcal{O}(n^2)$ flops by the Trench algorithm (Golub and Loan 1996, Algorithm 4.7.3). In general, the Trench algorithm can be combined with the

Durbin–Levinson recursions (Golub and Loan 1996, Algorithm 5.7.1), to calculate the exact likelihood of general linear Gaussian time series models (McLeod et al. 2007).

A major drawback of relying on these algorithms for Toeplitz matrices is that the Toeplitz structure is easily destroyed if the time series is observed indirectly. Consider a simple regression setting in which an fGn process is observed with independent Gaussian random noise,

$$\mathbf{y} = \mathbf{x} + \boldsymbol{\epsilon}, \tag{1}$$

where $\boldsymbol{\epsilon} \sim \mathcal{N}_n(\mathbf{0}, \mathbf{D}^{-1})$ and \mathbf{D} is diagonal. The log-density of $\mathbf{x} \mid \mathbf{y}$ is

$$\log \pi(\mathbf{x} \mid \mathbf{y}) = \frac{1}{2} \log |\mathbf{Q} + \mathbf{D}| - \frac{1}{2} \mathbf{x}^T (\mathbf{Q} + \mathbf{D}) \mathbf{x} + \mathbf{y}^T \mathbf{D} \mathbf{x} + \text{constant}. \tag{2}$$

The conditional mean of \mathbf{x} is found by solving $(\mathbf{Q} + \mathbf{D})\boldsymbol{\mu}_{\mathbf{x} \mid \mathbf{y}} = \mathbf{D}\mathbf{y}$ with respect to $\boldsymbol{\mu}_{\mathbf{x} \mid \mathbf{y}}$, while the marginal variances equal $\text{diag}\{(\mathbf{Q} + \mathbf{D})^{-1}\}$. The Toeplitz structure of $\text{Cov}(\mathbf{y}) = \mathbf{Q}^{-1} + \mathbf{D}^{-1}$ is only retained when the noise term has homogeneous variance, i.e. $\mathbf{D}^{-1} \propto \mathbf{I}$. With non-homogenous observation variance or missing data, the computational cost in fitting (1) would require general algorithms of cost $\mathcal{O}(n^3)$. This makes analysis of many real data sets infeasible, or at best challenging.

The motivation for expressing the log-likelihood function in terms of the precision matrix \mathbf{Q} , is to prepare for an approximate GMRF representation of the fGn model. We have already noted that aggregation of an infinite number of short-memory processes can explain long-memory behaviour in time series. This implies that \mathbf{Q} is (or can be approximated with) a sparse band matrix, but with a larger dimension (still denoted by n) for a finite sum. Assume for a moment that such an approximation exists. We can then apply general numerical algorithms for sparse matrices which only depend on the nonzero structure of the matrix. This implies that the numerical cost in dealing with \mathbf{Q} or $\mathbf{Q} + \mathbf{D}$, is the same. Conditioning on subsets of \mathbf{x} implies nothing else than working with a submatrix of \mathbf{Q} or $\mathbf{Q} + \mathbf{D}$, and does not add to the computational costs; see (Rue and Held 2005, chap. 2) for details. Specifically, we can make use of the Cholesky decomposition, in which the relevant precision matrix $\mathbf{Q} + \mathbf{D}$ is factorized as $\mathbf{Q} + \mathbf{D} = \mathbf{L}\mathbf{L}^T$, where \mathbf{L} is a lower triangular matrix. The log-likelihood is then evaluated with negligible cost (Rue 2001), as the log-determinant is $\log |\mathbf{Q} + \mathbf{D}| = 2 \sum_{i=1}^n L_{ii}$. The conditional mean is found by solving $\mathbf{L}\mathbf{u} = \mathbf{D}\mathbf{y}$ and $\mathbf{L}^T \boldsymbol{\mu}_{\mathbf{x} \mid \mathbf{y}} = \mathbf{u}$. The numerical cost in finding the Cholesky decomposition depends on the nonzero structure of the matrix. For time series models the cost is $\mathcal{O}(n)$ (Rue and Held 2005). The explicit construction of such an approximation is discussed next.

3 An approximate fGn model

This section presents an approximate fGn model which is a weighted sum of a few independent AR(1) processes. We will fit the parameters of the approximation to match the autocorrelation structure of fGn up to a given finite lag. The resulting approximate model is a GMRF with a banded precision matrix of fixed bandwidth, which gives a computational cost of $\mathcal{O}(n)$.

3.1 Fitting the autocorrelation function

Define m independent AR(1) processes by

$$z_{j,t} = \phi_j z_{j,t-1} + v_{j,t}, \quad j = 1, \dots, m, \quad t = 1, \dots, n, \quad (3)$$

where $0 < \phi_j < 1$ denotes the first-lag autocorrelation coefficient of the j th AR(1) process. Further, let $\{v_{j,t}\}_{j=1}^m$ be independent zero-mean Gaussians, with variance $\sigma_{v,j}^2 = 1 - \phi_j^2$. Define the cross-sectional aggregation of the AR(1) processes,

$$\tilde{x}_m = \sigma \sum_{j=1}^m \sqrt{w_j} z^{(j)}, \quad (4)$$

where $z^{(j)} = (z_{j,1}, \dots, z_{j,n})^T$ and $\sum_{j=1}^m w_j = 1$. The finite-sample properties of a similar aggregation of AR(1) processes are studied in Haldrup and Valdés (2017), where $w_j = 1/m$, $\sigma_v^2 = 1$ and where the coefficients ϕ_j are Beta distributed. They conclude that “First of all, one should be aware that cross-sectional aggregation leading to long memory is an asymptotic feature that applies for the cross-sectional dimension tending to infinity. In finite samples and for moderate cross-sectional dimensions, the observed memory of the series can be rather different from the theoretical memory” (Haldrup and Valdés 2017, pp. 7–8).

The approximation presented here only needs a small value of the cross-sectional dimension m to be accurate. The key idea to our approach is to fit the weights $\mathbf{w} = \{w_j\}_{j=1}^m$ and the autocorrelation coefficients $\boldsymbol{\phi} = \{\phi_j\}_{j=1}^m$ in (4) to match the autocorrelation function of fGn, as a function of H . The autocorrelation function of (4) follows directly as

$$\gamma_{\tilde{x}_m}(k) = \sum_{j=1}^m w_j \phi_j^{|k|}, \quad k = 0, 1, \dots, n - 1.$$

Now, fix a value of $1/2 < H < 1$. We fit the weights and coefficients $(\mathbf{w}, \boldsymbol{\phi})_H$ by minimizing the weighted squared error

$$(\mathbf{w}, \boldsymbol{\phi})_H = \operatorname{argmin}_{(\mathbf{w}, \boldsymbol{\phi})} \sum_{k=1}^{k_{\max}} \frac{1}{k} (\gamma_{\tilde{x}_m}(k) - \gamma_x(k))^2, \quad (5)$$

where k_{\max} represents a user-specified upper limit (we use $k_{\max} = 1000$). The squared error is weighted by $1/k$ to ensure a good fit for the autocorrelation function close to lag 0, while less weight is given to tail behaviour as the autocorrelation function is decaying slowly.

By a quite huge calculation done only once, we find $(\mathbf{w}, \boldsymbol{\phi})_H$ for a fine grid of H -values. Spline interpolation is used for values of H in between, to represent the weights and coefficients as continuous functions of H . The interpolation and fitting are performed using reparameterized weights and coefficients to ensure uniqueness and improved numerical behaviour. These reparameterizations are defined as

$$w_j = \frac{e^{v_j}}{\sum_{i=1}^m e^{v_i}} \quad \text{and} \quad \phi_j = \frac{1}{1 + \sum_{i=1}^j e^{-u_i}},$$

where $j = 1, \dots, m$ and where $v_1 = 0$. The Hurst exponent is transformed as $H = 1/2 + 1/2 \exp(h)/(1 + \exp(h))$. This ensures a stable and unconstrained parameter space on \mathbb{R}^{2m-1} for fixed h , where $\phi_1 > \dots > \phi_m$. Note that the error of the fit tends to zero, when H goes to 1 or 1/2. The resulting coefficients and weights for $m = 3$ and $m = 4$ are displayed in Fig. 1. The fitted weights and coefficients are also available in R using the function `INLA::inla.fgn`.

3.2 A Gaussian Markov random field representation

We will now discuss the precision matrix for the approximate fGn model. We start with one AR(1) process (3) of length n , with unit variance and a tridiagonal precision matrix

$$\mathbf{R}(\phi_j) = \frac{1}{1 - \phi_j^2} \begin{pmatrix} 1 & -\phi_j & & & \\ -\phi_j & 1 + \phi_j^2 & -\phi_j & & \\ & \ddots & \ddots & \ddots & \\ & & -\phi_j & 1 + \phi_j^2 & -\phi_j \\ & & & -\phi_j & 1 \end{pmatrix}.$$

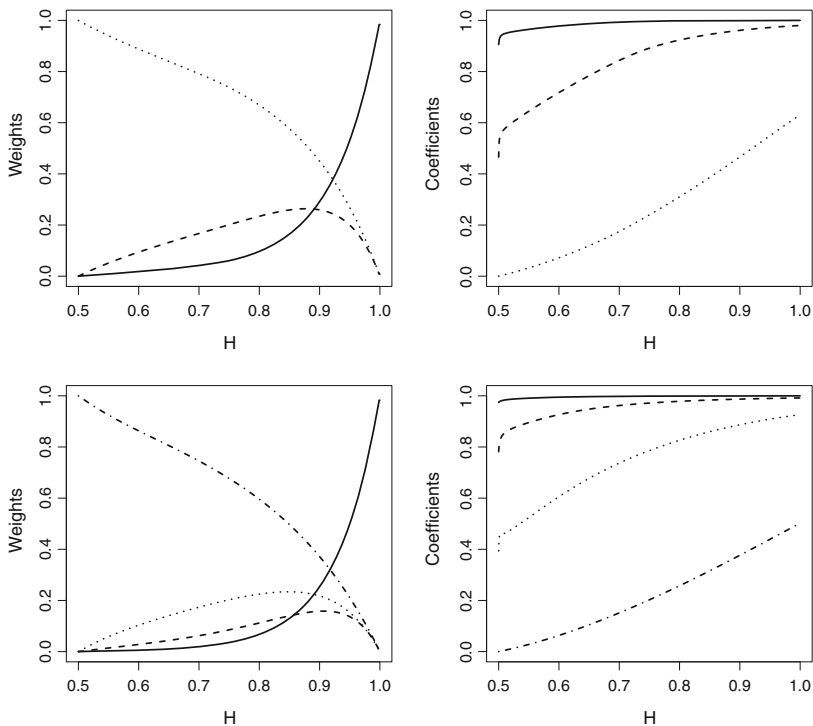
For the approximate fGn model, we have m such processes and their sum. Hence, we need the $(m + 1)n \times (m + 1)n$ precision matrix of the vector

$$(\tilde{x}_m^T, \mathbf{z}^{(1)T}, \dots, \mathbf{z}^{(m)T}). \quad (6)$$

To ensure a non-singular distribution, we will add a small Gaussian noise term to the sum, i.e. we let

$$\tilde{x}_m = \sigma \left(\sum_{j=1}^m \sqrt{w_j} z^{(j)} + \boldsymbol{\epsilon} \right), \quad (7)$$

Fig. 1 The optimized weights and coefficients of the approximation as a function of H . These are found by solving (5) using $m = 3$ (upper panels) and $m = 4$ (lower panels) components in the approximation



where the precision of ϵ is high, like $\kappa = \exp(15)$. The (upper part of the) precision matrix is found as

$$\begin{pmatrix} \kappa \mathbf{I} / \sigma^2 & -\sqrt{w_1} \kappa \mathbf{I} / \sigma & -\sqrt{w_2} \kappa \mathbf{I} / \sigma & \dots & -\sqrt{w_m} \kappa \mathbf{I} / \sigma \\ \mathbf{R}(\phi_1) + w_1 \kappa \mathbf{I} & \sqrt{w_1} w_2 \kappa \mathbf{I} & \dots & \sqrt{w_1} w_m \kappa \mathbf{I} & \\ & \mathbf{R}(\phi_2) + w_2 \kappa \mathbf{I} & \ddots & \ddots & \\ & & & \ddots & \sqrt{w_{m-1}} w_m \kappa \mathbf{I} \\ & & & & \mathbf{R}(\phi_m) + w_m \kappa \mathbf{I} \end{pmatrix}.$$

The nonzero structure is displayed in Fig. 2 (left panel) for $m = 3$ and $n = 10$. Even though the matrix is sparse, a more optimal structure can be achieved by grouping the $m + 1$ variables associated with each of the n time points,

$$\mathbf{v}^T = \left(\tilde{x}_{m1}, z_1^{(1)}, \dots, z_1^{(m)}, \tilde{x}_{m2}, z_2^{(1)}, \dots, z_2^{(m)}, \dots, \tilde{x}_{mn}, z_n^{(1)}, z_n^{(2)}, \dots, z_n^{(m)} \right).$$

The benefit of this reordering is that the corresponding precision matrix \mathbf{Q}_v is a band matrix, see Fig. 2 (middle panel). Doing the Cholesky decomposition, $\mathbf{Q}_v = \mathbf{L}_v \mathbf{L}_v^T$, the lower triangular matrix \mathbf{L}_v will inherit the lower bandwidth of \mathbf{Q}_v (Rue 2001; Golub and Loan 1996, thm. 4.3.1), see Fig. 2 (right panel). This leads to the following key result concern-

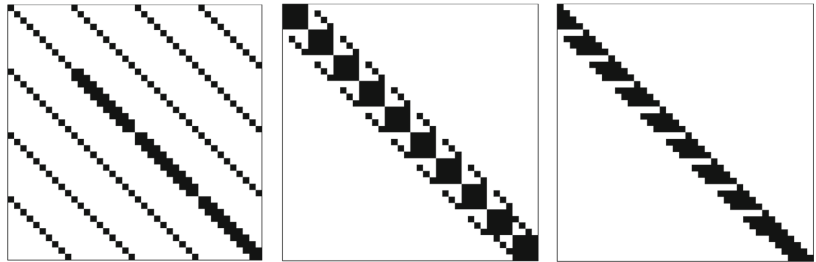
ing the computational cost of the approximate model, with a trivial proof.

Theorem 1 *The number of flops needed for Cholesky decomposition of \mathbf{Q}_v is $n(m + 1)^3$. The memory requirement for the Cholesky triangle is $n(m + 1)(m + 2)$ reals.*

Proof \mathbf{Q}_v is a band matrix with dimension $d = n(m + 1)$ and bandwidth $b = m + 1$. The computational cost of the Cholesky factorization, $\mathbf{Q}_v = \mathbf{L}_v \mathbf{L}_v^T$ is $db^2 = n(m + 1)^3$, and the memory requirement needed is $d(b + 1) = n(m + 1)(m + 2)$ (Golub and Loan 1996, sec. 4.3.5). \square

The computational cost and memory requirement of the Cholesky decomposition do not change if the approximate fGn model is observed indirectly, like in the regression model (1). Also, the computational cost is much smaller than using the Kalman recursions for a truncated ARFIMA process. Notice that it is possible to construct a GMRF approximation which has an even lower computational cost by using the cumulative sums of $\sigma \sum_{j=1}^m \sqrt{w_j} \mathbf{z}^{(j)}$ to form a sparse $mn \times mn$ precision matrix, with the same bandwidth. However, this approach does not allow for automatic source separation in situations where the fGn can be seen to represent combined signals. This feature of the approximate model is demonstrated in Sect. 5.1.

Fig. 2 The structure of the precision matrix of the vector in (6) (right panel), the structure of the precision matrix of the reordered vector in (8) (middle panel) and the resulting structure of the lower triangular matrix in the Cholesky decomposition (right panel). The matrices are illustrated for the case $m = 3$ and $n = 10$



3.3 Choosing the number of AR(1) components in the approximation

The choice of m in (7) reflects a trade-off between computational efficiency and approximation error. This implies that m should be as small as possible but still large enough to give a reasonably accurate approximation of the autocorrelation function of fGn. Figure 3 illustrates the autocorrelation function of fGn compared with the approximate model when $m = 3$ and $m = 4$, using $k_{\max} = 1000$ in (5). We only show results for $H = 0.9$ as the differences between the curves will be less visible using smaller values of H .

We do notice that $m = 4$ gives an almost perfect match of the autocorrelation function up to k_{\max} . For larger lags, the autocorrelation function of the approximate fGn model will have an exponential decay; hence, we cannot match the hyperbolic decay of the exact fGn. As a consequence, k_{\max} can be seen as a trade-off between having a good fit for the first part of the autocorrelation function versus tail behaviour.

A different way to illustrate the difference between the approximate and exact fGn models is in terms of the Kullback–Leibler divergence. This is a measure of complexity between probability distributions, which here measures the information lost when the approximate fGn model is used instead of the exact fGn model. Figure 4 displays the square root of the Kullback–Leibler divergence for $n = 500$ and $n = 2000$, as a function of H . We notice that $m = 4$ clearly gives an improvement over $m = 3$, in particular for larger values of H . The loss in information when $n = 2000$ compared to $n = 500$ is small, despite the fact that the autocorrelation function is fitted only up to lag $k_{\max} = 1000$.

3.4 A note on ARFIMA models

The presented approximation is especially suitable in fitting a parsimoniously parameterized model like fGn. The fact that the autocorrelation function of fGn is specified by only one parameter can be seen both as a modelling benefit but also as a limitation. An ARFIMA(p, d, q) model can be used to model both short- and long-memory dependency structures, both simultaneously and separately. The parameters p and q give the orders of the short-memory autoregressive and mov-

ing average parts of the model. The long-memory property is prescribed by the parameter d , giving the order of the fractional differencing of the underlying autoregressive moving average model.

The method of matching autocorrelation functions can easily be used to provide an approximation of ARFIMA($0, d, 0$). Figure 5 displays the exact and approximated autocorrelation functions when $d = 0.3$ and $d = 0.4$. As illustrated, the approximation method is very accurate also in this case. This is not surprising as the ARFIMA($0, d, 0$) model has very similar properties to fGn when $d = H - 0.5$. Extensions of the given approximation idea to the case of estimating all parameters of ARFIMA(p, d, q) models represent an interesting future project, but we have considered this to be beyond the scope of this paper. We also note that ARFIMA models have been criticized as having an atypical long-range dependency property, offering “*no meaningful diversity beyond fGn*” (Veitch et al. 2013, p. 2). Even though the use of fGn processes or ARFIMA($0, d, 0$) might seem limited, we gain flexibility by incorporating the given GMRF approximation within the general class of latent Gaussian models (Rue et al. 2009). This gives a user-friendly framework in which an fGn component can be combined with other explanatory effects in modelling real time series.

4 Simulation results

To evaluate the properties of the approximate fGn model, we now study the loss of accuracy when using the approximate versus the exact fGn model, for estimation and prediction. The results will demonstrate an impressive performance for both the estimation and prediction exercises, using the approximate fGn model with $m = 4$.

4.1 Maximum likelihood estimation of H

We first study the loss of accuracy using the approximate versus the exact fGn model in maximum likelihood estimation of H . We fit the approximate model using $m = 3$ and $m = 4$, to simulated fGn series of length $n = 500$, with $N = 1000$ replications. The error is evaluated in terms of the root mean

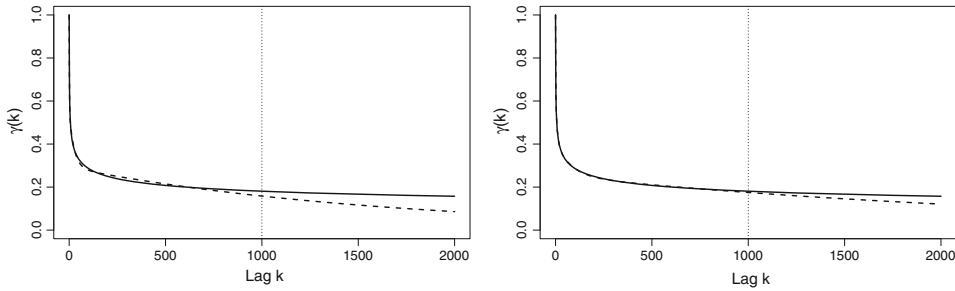


Fig. 3 The exact autocorrelation function (solid) when $H = 0.9$, versus the autocorrelation function of the approximate model (dashed), using $m = 3$ (left panel) and $m = 4$ (right panel). The autocorrelations of the approximate and exact models are matched up to lag $k_{\max} = 1000$

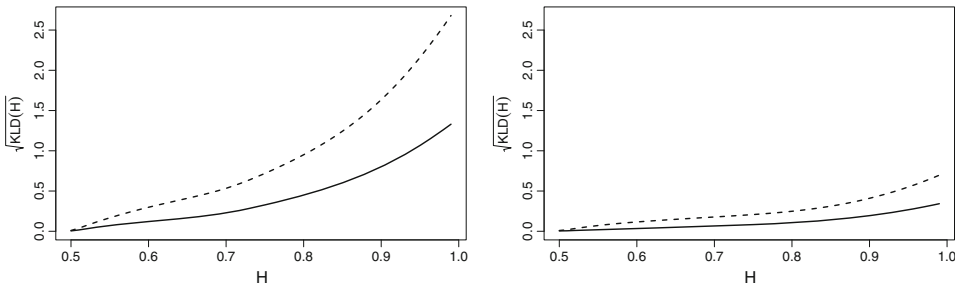


Fig. 4 The square root of the Kullback–Leibler divergence as a function of H for time series of length $n = 500$ (solid) and $n = 2000$ (dashed), using the approximate fGn model with $m = 3$ (left panel) and $m = 4$ (right panel)

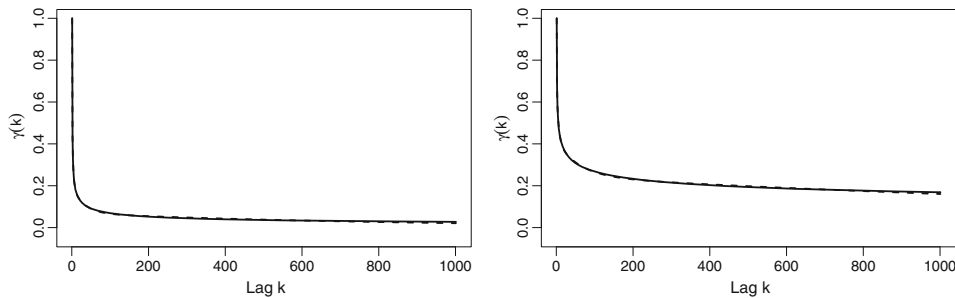


Fig. 5 The exact (solid) and approximated (dashed) autocorrelation function for ARFIMA(0, d ,0), where $d = 0.3$ (left) and $d = 0.4$ (right)

squared error (RMSE) and the mean absolute error (MAE) of $\tilde{H}_i - \hat{H}_i$, where \tilde{H}_i and \hat{H}_i denote the estimates using the approximate versus the exact fGn, for the i th replication.

The results are summarized in Table 1 in which the true Hurst exponent ranges from 0.60 to 0.95. Using $m = 3$, the Hurst exponent is underestimated and the error is seen to increase with H , at least up to 0.90. The situation really improves for $m = 4$, in which the error is small for all values of H . The standard deviation estimates found from the empir-

ical Fisher information, are more similar than the estimates themselves (results not shown).

Figure 6 displays scatterplots of the maximum likelihood estimates for the approximate model with $m = 3$ and 4, versus the estimates using the exact model, when $H = 0.7, 0.8$ and 0.9. The inaccuracy for $m = 3$ is clearly visible and increases with increasing values of H , while $m = 4$ shows very good performance. We have noticed that the same general remarks also hold when we increase the length of the

Table 1 Maximum likelihood estimation of H in simulations. The columns show the average of the maximum likelihood estimates of H using the exact versus the approximate models with $m = 3$ and $m = 4$, the corresponding root mean squared error and the absolute mean error

H	Average MLE of H			RMSE(\tilde{H})		MAE(\tilde{H})	
	Exact	$m = 3$	$m = 4$	$m = 3$	$m = 4$	$m = 3$	$m = 4$
0.60	0.5998	0.5998	0.5998	0.0019	0.0007	0.0015	0.0006
0.65	0.6481	0.6478	0.6480	0.0026	0.0008	0.0021	0.0006
0.70	0.7004	0.6997	0.7003	0.0033	0.0008	0.0026	0.0006
0.75	0.7488	0.7472	0.7487	0.0032	0.0007	0.0025	0.0006
0.80	0.7998	0.7974	0.7996	0.0031	0.0006	0.0026	0.0005
0.85	0.8503	0.8471	0.8500	0.0035	0.0004	0.0032	0.0004
0.90	0.8999	0.8965	0.8997	0.0035	0.0003	0.0034	0.0003
0.95	0.9500	0.9475	0.9499	0.0025	0.0002	0.0025	0.0001

The generated fGn processes are of length $n = 500$ with $N = 1000$ replications

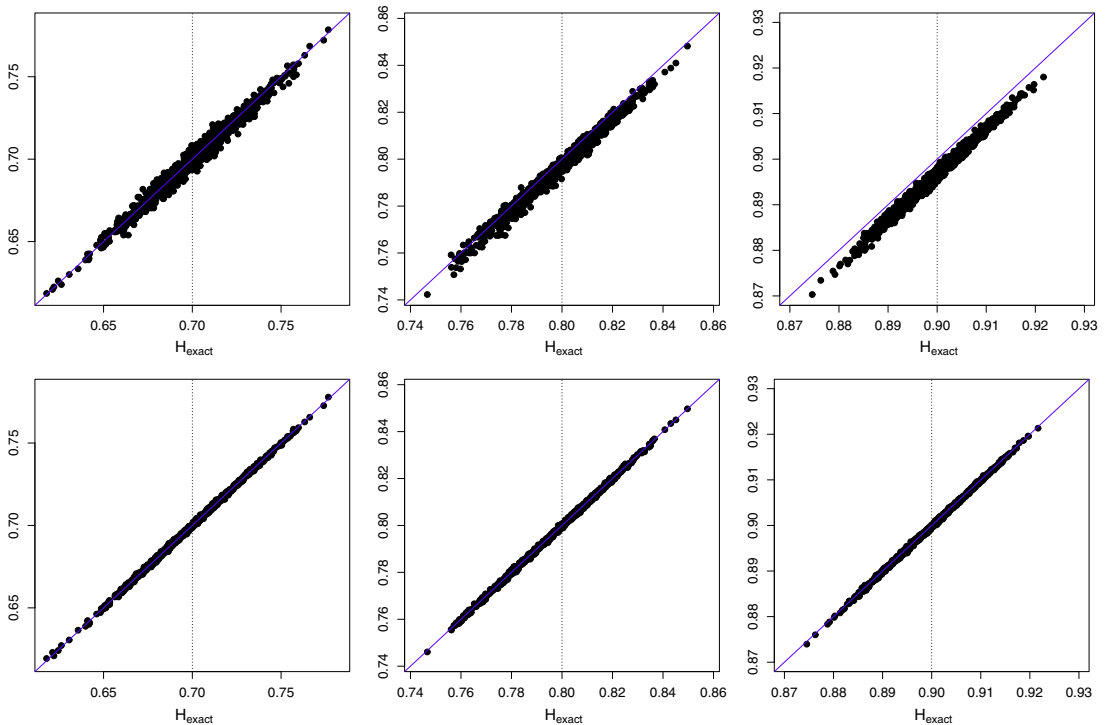


Fig. 6 The maximum likelihood estimates of H for $N = 1000$ replications using the approximate fGn model with $m = 3$ (upper panels) and $m = 4$ (lower panels), versus the exact fGn. The true H values are $H = 0.7$ (left), $H = 0.8$ (middle) and $H = 0.9$ (right) and the generated series have length $n = 500$

series to $n = 2000$. The series then contain more information about H , and the error due to using $k_{\max} = 1000$ is negligible. In conclusion, we do get a very low loss of accuracy using the approximate model with $m = 4$. This is impressive, especially as it applies for all reasonable values of H in the long-memory range.

4.2 Predictive properties

This section investigates the effect of the approximation error when we observe an fGn process of length n with fixed H , and then want to predict future time points. The approximate model is implemented with $m = 4$. To evaluate the properties of the predictions, we consider the empirical mean of the

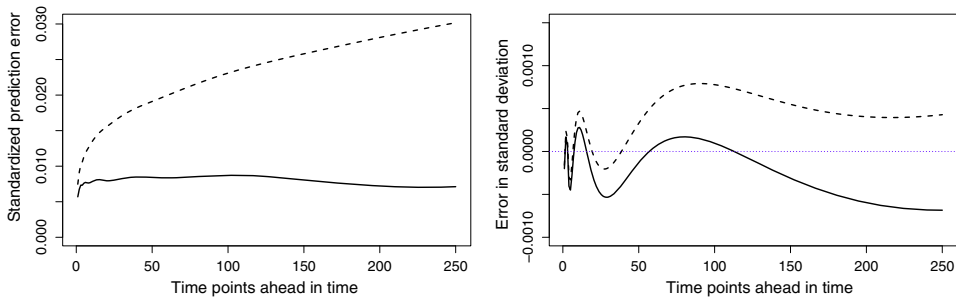


Fig. 7 The prediction error for mean (8), predicting up to 250 points ahead, when $H = 0.8$ (left panel). The similar error in the predictive standard deviation (9) (right panel). The observed time series is either of length $n = 500$ (solid) or $n = 2000$ (dashed)

standardized absolute prediction error,

$$\text{err}_\mu(p) = \frac{1}{N} \sum_{i=1}^N \frac{|\tilde{\mu}_{p,i} - \mu_{p,i}|}{\sigma_p}, \tag{8}$$

where N is the number of replications. $\tilde{\mu}_{p,i}$ is the conditional expectation for p time points ahead from the i th replication using the approximate fGn model. Correspondingly, $\mu_{p,i}$ is the conditional expectation using the exact fGn model, while σ_p is the conditional standard deviation. To measure the error in the conditional standard deviation, we use

$$\text{err}_\sigma(p) = \frac{\tilde{\sigma}_p}{\sigma_p} - 1, \tag{9}$$

which does not depend on the replication.

The left panel of Fig. 7 illustrates the empirical prediction error in (8) for $p = 1, \dots, 250$ time points ahead, following either $n = 500$ or $n = 2000$ observations. The right panel shows the corresponding error in the prediction standard deviation (9). We only report results for $H = 0.8$ as other values of the Hurst exponent give similar results. We notice that the mean prediction error increases slightly when $n = 2000$ compared to $n = 500$, which is explained by the increased error for lags larger than $k_{\max} = 1000$. Otherwise, both errors are relatively small and also quite stable with p .

5 Real data applications: source separation and Bayesian inference

This section demonstrates two different aspects of the approximate fGn model in real data applications. First, the approximate model can be used as a tool for source separation of a combined signal, for example representing underlying cycles or variations for different time scales. This will be illustrated in analysing the Nile river dataset (available

in R as `longmemo::NileMin`). These data give annual water level minima for the period 622–1284, measured at the Roda Nilometer near Cairo. Second, the approximate model can easily be combined with other model components within the general framework of latent Gaussian models and fitted efficiently using R-INLA. This is demonstrated in analysing the Hadley Centre Central England Temperature series (HadCET), available at <http://www.metoffice.gov.uk/hadobs>. These data give mean monthly measurements of surface air temperatures for Central England in the period 1659–2016. The two datasets are illustrated in Fig. 8.

5.1 Signal separation for the Nile river annual minima

The Nile river dataset is a widely studied time series (Mandelbrot and Wallis 1969b; Beran 1994; Eltahir 1996) often used as an example of a real fGn process (Koutsoyiannis 2002; Benmehdi et al. 2011). Analysis of this dataset led to the discovery of the Hurst phenomenon (Hurst 1951). For hydrological time series, this phenomenon has been explained as the tendency of having irregular clusters of wet and dry periods and can be related to characteristics of the fluctuations of the series at different temporal scales (Koutsoyiannis 2002).

We can easily fit the exact fGn model to this dataset as the process is observed directly, and the length of the series is only $n = 663$. In this case, the maximum likelihood estimate for the Hurst exponent is $\hat{H} = 0.831$. Using the approximate fGn model with $m = 4$, we get $\hat{H} = 0.829$. This illustrates that the approximate and exact models give very similar estimates. A value of $H \approx 0.83$ also corresponds well with results reported in literature (Mandelbrot and Wallis 1969a; Benmehdi et al. 2011). Beran and Terrin (1996) states that both a fractional Gaussian noise with $H \approx 0.83$ and an ARFIMA(0, d , 0) model with $d = 0.4$ fits well for this dataset. Graves et al. (2015) analyse the given dataset fitting an ARFIMA(0, d , 0) model using an MCMC-approach.

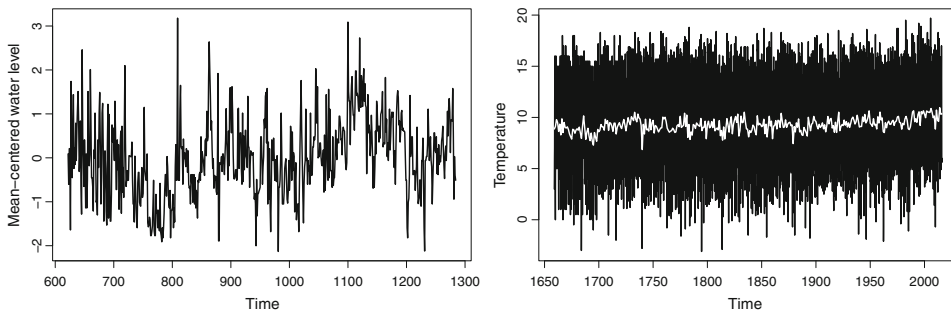


Fig. 8 Mean-centred annual minimum water level of the Nile river (left panel). Monthly mean surface air temperatures for Central England, also including the annual mean temperatures in white (right panel)

They get a posterior estimate of $d = 0.402$ with a 95% credible interval equal to $(0.336, 0.482)$. Our results using the approximated ARFIMA(0, d , 0) model are very similar giving $d = 0.399$ with a 95% credible interval equal to $(0.350, 0.438)$.

An advantage of the approximate versus the exact model is that the decomposition given by the mixture of AR(1) can be used as a source separation tool. Figure 9 illustrates the four estimated weighted AR(1) components in fitting model (5). The estimated autocorrelation coefficients for these components equal $\phi = (0.999, 0.982, 0.847, 0.291)$, while the weights are $w = (0.099, 0.129, 0.232, 0.540)$. The estimated standard deviation is $\hat{\sigma} = 0.888$.

As illustrated in Fig. 1, the first autocorrelation coefficient will always be quite close to 1. This gives a slowly varying trend, which in this case basically represents the mean. The second component also reflects a slowly varying signal, which can be interpreted to represent cycles of the water level fluctuations of about 200–250 years. The third component seems to reflect shorter cycles of length 30–100 years. These cycles are seen to appear more irregularly, and we also notice the tendency of having clusters of years with high and low water levels, respectively. The fourth component, which has the smallest autocorrelation coefficient and the largest weight, can be interpreted as weakly correlated annual noise.

Kondrashov et al. (2005) study oscillatory modes of Nile River records using empirical orthogonal functions. Fitting a nonlinear data-adaptive trend to the data for the period 622–1470, they detect a 256-year cycle. This is in correspondence with our result. They also find shorter cycles including quasi-quadrennial and quasi-biennial cycles, in addition to periodicities of 64, 19, 12 and 7 years. A disadvantage of using the approximate fGn model as a source separation tool is that the number of modes is fixed to be equal to the number of AR(1) components used in the approximation. An advantage is that the resulting components do have a quite clear

interpretation as these can be linked directly to the weights and autocorrelation coefficients of the approximation.

5.2 Full Bayesian analysis of a temperature series

The HadCET series is the longest existing instrumental record of monthly temperatures in the world. The observations started in January 1659 and have been updated monthly. The observed temperatures do have uncertainties (Parker and Horton 2005) and has been revised several times (Manley 1953, 1974; Parker et al. 1992). Especially, the measurements up to 1699 have a precision of 0.5 °C, while the precision is 0.1 °C thereafter (Graves et al. 2015). We analyse temperatures up to December 2016, which gives a total of $n = 4296$ observations.

We assume that the mean of the given temperatures can be modelled by

$$E(y_t) = \beta_0 + \beta_1 t + s_t + x_t, \quad t = 1, \dots, 4296,$$

where y_t is the temperature in month t . The given linear predictor includes an intercept β_0 , a linear trend β_1 and a seasonal effect s_t of periodicity $q = 12$ which captures monthly variations. This seasonal effect is modelled as an intrinsic GMRF of rank $n - q + 1$, having precision parameter τ_s (Rue and Held 2005, p. 122) and scaled to have a generalized variance equal to 1 (Sørbye and Rue 2014). The term x_t denotes the approximate fGn model with $m = 4$, having precision parameter τ_x .

The parameters β_0 and β_1 are assigned vague Gaussian priors, $\beta_i \sim N(0, 10^3)$, while we use penalized complexity priors (PC priors) (Simpson et al. 2017) for all hyperparameters. This implies a type II Gumbel distribution for the precision parameters τ_s and τ_x , scaled using the probability statement $P(\tau^{-1/2} > 1) = 0.01$. The PC prior for H (Sørbye and Rue 2017) is scaled by assuming the tail probability $P(H > 0.9) = 0.1$. The resulting analysis has proven

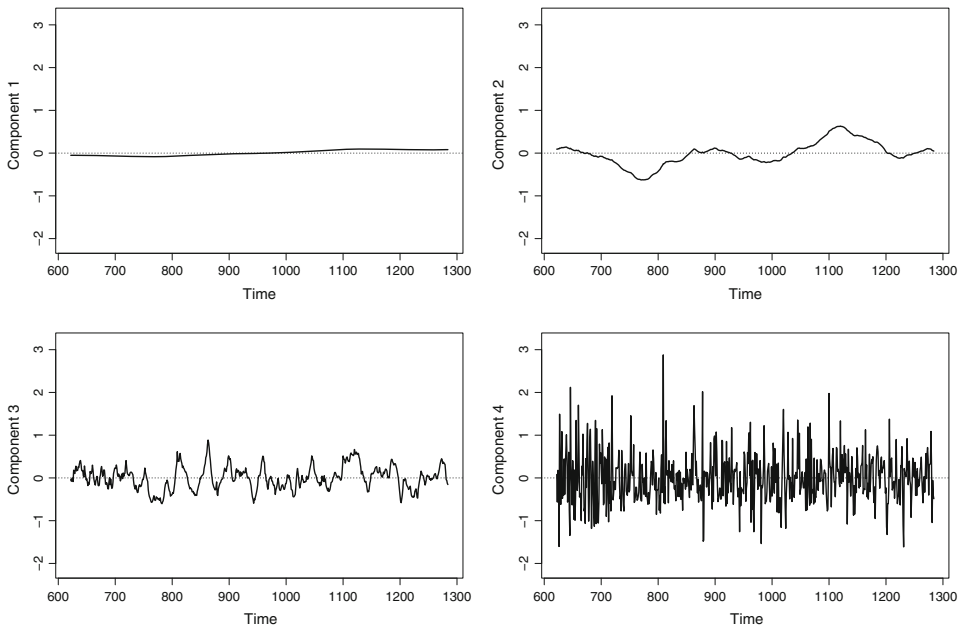


Fig. 9 The estimated weighted AR(1) components for mean-centred annual minimum water levels of the Nile river, using the approximate fGn model with $m = 4$

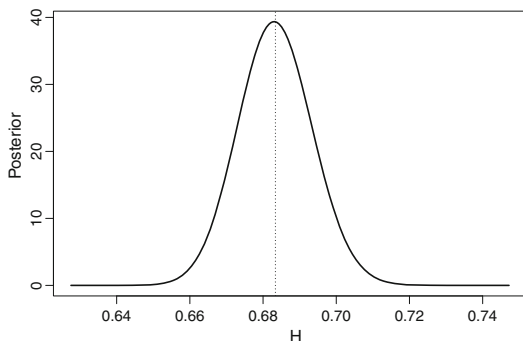


Fig. 10 Analysing the HadCET series: the marginal posterior $\pi(H | y)$

to be robust to prior choices. Among others, this has been investigated by using $\text{Gamma}(1, 5 \times 10^{-5})$ priors for the precision parameters (default in INLA) and the common choice of using a uniform prior for H (Benmehdi et al. 2011). We do prefer to use PC priors as these represent a principle-based choice of priors (Simpson et al. 2017) which also facilitates interpretation of hyperprior parameters (Sørbye et al. 2018).

Analysis of the given model using an exact fGn term is infeasible in terms of computational cost and memory

usage. A MacBook Pro with 16GB of RAM crashes due to memory shortage when analysing exact fGn processes of length $n > 2500$. Using the approximate fGn term with $m = 4$, the full Bayesian analysis takes about 14 seconds. The inference gives a significantly positive trend with posterior mean $\hat{\beta}_1 = 2.4 \times 10^{-4}$ with 95% credible interval $(1.2 \times 10^{-4}, 3.7 \times 10^{-4})$. This corresponds to an increased temperature of approximately 0.29 ± 0.15 °C per century. This is in correspondence with the result in Gil-Alana (2003) who estimated an increase of about 0.23 °C per century using the same dataset up to the year of 2001.

The marginal posterior for H is illustrated in Fig. 10. The posterior mean is $\hat{H} = 0.683$ with a 95% equi-tailed credible interval equal to (0.664, 0.704). We have also fitted the model where x_t is the approximated ARFIMA(0, d , 0) model giving a posterior mean estimate of d equal to 0.229 with 95% credible interval equal to (0.205, 0.253). These results are quite similar to Graves et al. (2015) who fitted the ARFIMA(0, d , 0) model to a deseasonalized version of the temperatures, giving a posterior mean of $d = 0.209$ with a 95% credible interval equal to (0.186, 0.235). However, in fitting the model to the whole series they assume mean stationarity. In analysing the series for four different time periods, Graves et al. (2015) report a significantly higher value of the long-memory parameter ($d = 0.277$) for the

first time period (1659 – 1744) compared to the other time periods. We also observed this, both in fitting the fGn process ($H = 0.740$) and the ARFIMA(0, d , 0) model ($d = 0.288$). The higher value of the long-memory parameter in this case might be explained by a lack of resolution for the first time period (Graves et al. 2015).

6 Concluding remarks

In this paper, we obtain a remarkably accurate approximation of fGn using a weighted sum of only four AR(1) components. The resulting approximate fGn model has a small loss of accuracy for the whole long-memory range of H . The key idea to obtain this is to ensure that the approximate model captures the most essential part of the autocorrelation structure of the exact fGn model. This is achieved by appropriate weighting, matching the autocorrelation structure up to a specified maximum lag. The same idea can be used to approximate other models, like ARFIMA(0, d , 0).

By construction, the autocorrelation function of the approximate model has an exponential decay for lags larger than the specified maximum lag. This implies that the approximate model does not satisfy formal definitions of long-memory processes. However, this trade-off is needed to make analysis of realistically complex models computationally feasible. The great benefit of the resulting approximation is that it has a GMRF structure. This is crucial, especially as computations can be performed equally efficient in unconditional and conditional scenarios.

An approximate model can never reflect the properties of the exact model perfectly, but neither does a theoretical model in explaining an observed data set. In theory, the fGn model corresponds to an aggregation of an infinite number of AR(1) components which indicates that the model is difficult to interpret in practice. The given decomposition of just a few AR(1) terms might provide a more realistic model. As an example, we have provided a decomposition of the Nile river data, which reflects fluctuations and cycles for different temporal scales. Such a decomposition could also be valuable in analysing other time series. For example, long memory in temperature series has been related to an aggregation of a few simple underlying geophysical processes (Fredriksen and Rypdal 2017).

Implementation of the approximate fGn model in R-INLA provides an easy-to-use tool to analyse models with fGn structure. As demonstrated in the temperature example, we can easily combine the fGn model component with other terms in an additive linear predictor, for example nonlinear effects of covariates, random error terms and random effects including both temporally and/or spatially structured components. Also, the mean function of the approximate fGn model can be modified to include climate forcing and additional

hyperparameters to provide realistic models for temperature series. Among others, this makes it possible to estimate equilibrium climate sensitivity in a computationally efficient way (Rypdal et al. 2018). Further modifications include extensions to spatio-temporal analysis. Especially, we do see a potential in incorporating fGn model components in the analysis of spatial time series combining the given approximate model with the methodology in Lindgren et al. (2011).

References

- Baillie, R.T.: Long memory processes and fractional integration in econometrics. *J. Econ.* **73**, 5–59 (1996)
- Benmehdi, S., Makarava, N., Menhamidouche, N., Holschneider, M.: Bayesian estimation of the self-similarity exponent of the Nile River fluctuation. *Nonlinear Process. Geophys.* **18**, 441–446 (2011)
- Beran, J.: *Statistics for Long-Memory Processes*, 1st edn. Chapman & Hall, New York (1994)
- Beran, J., Terrin, N.: Testing for a change of the long-memory parameter. *Biometrika* **83**, 627–638 (1996)
- Beran, J., Schütznner, M., Ghosh, S.: From short to long memory: aggregation and estimation. *Comput. Stat. Data Anal.* **54**, 2432–2442 (2010)
- Beran, J., Feng, Y., Ghosh, S., Kulik, R.: *Long-Memory Processes—Probabilistic Properties and Statistical Methods*. Springer, Heidelberg (2013)
- Box, G.E.P., Jenkins, G.M.: *Time Series Analysis, Forecasting and Control*. Holden-Day, San Francisco (1980)
- Chan, N.H., Palma, W.: Estimation of long-memory time series models: a survey of different likelihood-based methods. *Adv. Econ.* **20**, 89–121 (2006)
- Cont, R.: Long range dependence in financial markets. In: Lévy-Véhel, J., Buton, E. (eds.) *Fractals in Engineering*, pp. 159–180. Springer, London (2005)
- Doukhan, P., Oppenheim, G., Taqqu, M.: *Theory and Applications of Long-Range Dependence*. Birkhauser, Boston (2003)
- Durbin, J.: The fitting of time-series models. *Rev. Inst. Int. Stat.* **28**, 233–244 (1960)
- Eltahir, E.A.B.: El Niño and the natural variability in the flow of the Nile River. *Water Resour. Res.* **32**, 131–137 (1996)
- Franzke, C.: Nonlinear trends, long-range dependence, and climate noise properties of surface temperature. *J. Clim.* **25**, 4172–4182 (2012)
- Fredriksen, H.B., Rypdal, M.: Long-range persistence in global surface temperatures explained by linear multibox energy balance models. *J. Clim.* **30**, 7157–7168 (2017)
- Gil-Alana, L.A.: An application of fractional integration to a long temperature series. *Int. J. Climatol.* **23**, 1699–1710 (2003)
- Golub, G., Loan, C.V.: *Matrix Computations*, 3rd edn. Johns Hopkins University Press, Baltimore (1996)
- Granger, C.W.J.: Long memory relationships and the aggregation of dynamic models. *J. Econ.* **14**, 227–238 (1980)
- Granger, C.W.J., Joyeux, R.: An introduction to long-memory time series models and fractional differencing. *J. Time Ser. Anal.* **1**, 15–29 (1980)
- Graves, T., Gramacy, R.B., Franzke, C.L.E., Watkins, N.W.: Efficient Bayesian inference for natural time series using ARFIMA processes. *Nonlinear Process. Geophys.* **22**, 679–700 (2015)
- Graves, T., Gramacy, R., Watkins, N., Franzke, C.: A brief history of long memory: Hurst, Mandelbrot and the road to ARFIMA, 1951–1980. *Entropy* **19**, 1–21 (2017)

- Haldrup, N., Valdés, J.E.V.: Long memory, fractional integration and cross-sectional aggregation. *J. Econ.* **199**, 1–11 (2017)
- Hosking, J.R.M.: Fractional differencing. *Biometrika* **68**, 165–176 (1981)
- Hosking, J.R.M.: Modeling persistence in hydrological time series using fractional differencing. *Water Resour. Res.* **20**, 1898–1908 (1984)
- Hurst, H.E.: Long-term storage capacities of reservoirs. *Trans. Am. Soc. Civ. Eng.* **116**, 770–799 (1951)
- Jensen, A.N., Nielsen, M.Ø.: A fast fractional difference algorithm. *J. Time Ser. Anal.* **35**, 428–436 (2014)
- Knorr-Held, L., Rue, H.: On block updating in Markov random field models for disease mapping. *Scand. J. Stat.* **29**, 597–614 (2002)
- Kondrashov, D., Feliks, Y., Ghil, M.: Oscillatory modes of the extended Nile River records (a.d. 622–1922). *Geophys. Res. Lett.* **32**, 1–4 (2005)
- Koutsoyiannis, D.: The Hurst phenomenon and fractional Gaussian noise made easy. *Hydrol. Sci. J.* **47**, 573–595 (2002)
- Levinson, N.: The Wiener (root mean square) error criterion in filter design and prediction. *J. Math. Phys.* **25**, 261–278 (1947)
- Lindgren, F., Rue, H., Lindström, J.: An explicit link between Gaussian fields and Gaussian Markov random fields: the stochastic partial differential equation approach (with discussion). *J. R. Stat. Soc. B* **73**, 423–498 (2011)
- Mandelbrot, B.B., Van Ness, J.W.: Fractional Brownian motions, fractional noises and applications. *SIAM Rev.* **10**, 422–437 (1968)
- Mandelbrot, B.B., Wallis, J.R.: Computer experiments with fractional Gaussian noises. *Water Resour. Res.* **5**, 228–267 (1969a)
- Mandelbrot, B.B., Wallis, J.R.: Global dependence in geophysical records. *Water Resour. Res.* **5**, 321–340 (1969b)
- Manley, G.: The mean temperature of central England, 1698–1952. *Q. J. R. Meteorol. Soc.* **79**, 242–261 (1953)
- Manley, G.: Central England temperatures: monthly means 1659–1973. *Q. J. R. Meteorol. Soc.* **100**, 389–405 (1974)
- Maxim, V., Sendur, L., Fadili, J., Suckling, J., Gould, R., Howard, R., Bullmore, E.: Fractional Gaussian noise, functional MRI and Alzheimer’s disease. *NeuroImage* **25**, 141–158 (2005)
- McLeod, A.I., Hipel, K.W.: Preservation of the rescaled adjusted range: 1. A reassessment of the Hurst phenomenon. *Water Resour. Res.* **14**, 491–508 (1978)
- McLeod, A.I., Yu, H., Krougly, Z.L.: Algorithms for linear time series analysis: With R Package. *J. Stat. Softw.* **23**, 1–26 (2007)
- Molz, F.J., Liu, H.H., Szulga, J.: Fractional Brownian motion and fractional Gaussian noise in subsurface hydrology: a review, presentation of fundamental properties, and extensions. *Water Resour. Res.* **33**, 2273–2286 (1997)
- Palma, W., Chan, N.H.: Estimation and forecasting of long-memory processes with missing values. *J. Forecast.* **16**, 395–410 (1997)
- Parker, D.E., Horton, E.B.: Uncertainties in the central England temperature series since 1878 and some changes to the maximum and minimum series. *Int. J. Climatol.* **25**, 1173–1188 (2005)
- Parker, D.E., Legg, T.P., Folland, C.K.: A new daily central England temperature series, 1772–1991. *Int. J. Climatol.* **12**, 317–342 (1992)
- Purczyński, J., Włodarski, P.: On fast generation of fractional Gaussian noise. *Comput. Stat. Data Anal.* **50**, 2537–2551 (2006)
- Rue, H.: Fast sampling of Gaussian Markov random fields. *J. R. Stat. Soc. B* **63**, 325–338 (2001)
- Rue, H., Held, L.: *Gaussian Markov Random Fields: Theory and Applications*. Chapman & Hall/CRC, London (2005)
- Rue, H., Martino, S., Chopin, N.: Approximate Bayesian inference for latent Gaussian models using integrated nested Laplace approximations (with discussion). *J. R. Stat. Soc. B* **71**, 319–392 (2009)
- Rypdal, M., Rypdal, K.: Long-memory effects in linear response models of Earth’s temperature and implications for future global warming. *J. Clim.* **27**, 5240–5258 (2014)
- Rypdal, M., Fredriksen, H.B., Myrsvoll-Nilsen, E., Rypdal, K., Sørbye, S.H.: Emergent scale invariance and climate sensitivity. *Under Rev. Clim.* (2018). <https://doi.org/10.20944/preprints201810.0542.v1>
- Simpson, D., Rue, H., Riebler, A., Martins, T.G., Sørbye, S.H.: Penalising model component complexity: a principled, practical approach to constructing priors. *Stat. Sci.* **232**, 1–28 (2017)
- Sørbye, S.H., Rue, H.: Scaling intrinsic Gaussian Markov random field priors in spatial modelling. *Spat. Stat.* **8**, 39–51 (2014)
- Sørbye, S.H., Rue, H.: Fractional Gaussian noise: Prior specification and model comparison. *Environmetrics* (2017). <https://doi.org/10.1002/env.2457>
- Sørbye, S.H., Illian, J.B., Simpson, D.P., Burslem, D., Rue, H.: Careful prior specification avoids incautious inference for log-gaussian cox point processes. *J. R. Stat. Soc. C* (2018). <https://doi.org/10.1111/rssc.12321>
- Taqqu, M.S., Teverovsky, V., Willinger, W.: Estimators for long-range dependence: an empirical study. *Fractals* **3**, 785–798 (1995)
- Toussoun, O.: M’emoire sur l’histoire du Nil. M’emoires a l’Institut d’Egypte **18**, 366–404 (1925)
- Trench, W.F.: An algorithm for the inversion of finite Toeplitz matrices. *J. Soc. Ind. Appl. Math.* **12**, 515–522 (1964)
- Veitch, D., Gorst-Rasmussen, A., Gefferth, A.: Why FARIMA models are brittle. *Fractals* (2013). <https://doi.org/10.1142/S0218348X13500126>
- Willinger, W., Paxson, V., Taqqu, M.S.: Self-similarity and heavy tails: structural modeling of network traffic. In: Adler, R.J., Feldman, R.E., Taqqu, M.S. (eds.) *A Practical Guide to Heavy Tails: Statistical Techniques and Applications*, pp. 27–53. Birkhauser, Boston (1996)

Publisher’s Note Springer Nature remains neutral with regard to jurisdictional claims in published maps and institutional affiliations.

Paper II

Statistical estimation of global surface temperature response to forcing under the assumption of temporal scaling

Under review for *Earth System Dynamics*. The peer review process is public and can be found at Earth System Dynamics Discussions:
www.earth-syst-dynam-discuss.net/esd-2019-66/



Statistical estimation of global surface temperature response to forcing under the assumption of temporal scaling

Eirik Myrvoll-Nilsen¹, Sigrunn Holbek Sørbye¹, Hege-Beate Fredriksen¹, Håvard Rue², and Martin Rypdal¹

¹Department of Mathematics and Statistics, UiT The Arctic University of Norway, N-9037 Tromsø, Norway

²CEMSE Division, King Abdullah University of Science and Technology, Thuwal, Saudi Arabia

Correspondence: Eirik Myrvoll-Nilsen (eirik.myrvoll-nilsen@uit.no)

Abstract. Reliable quantification of the global mean surface temperature (GMST) response to radiative forcing is essential for assessing the risk of dangerous anthropogenic climate change. We present the statistical foundations for an observation-based approach, using a stochastic linear-response model that is consistent with the long-range temporal dependence observed in global temperature variability. We have incorporated the model in a latent Gaussian modeling framework, which allows for the use of integrated nested Laplace approximations (INLAs) to perform full Bayesian analysis. As examples of applications, we estimate the GMST response to forcing from historical data and compute temperature trajectories under the Representative Concentration Pathways (RCPs) for future greenhouse gas forcing. For historic runs in the Model Intercomparison Project Phase 5 (CMIP5) ensemble, we estimate response functions and demonstrate that one can infer the transient climate response (TCR) from the instrumental temperature record. We illustrate the effect of long-range dependence by comparing the results with those obtained from a 1-box energy balance model. The software developed to perform the given analyses is publicly available as the R-package `INLA.climate`.

1 Introduction

Despite decades of research and development of global circulation models (GCMs) and Earth system models (ESMs), the discrepancies between models remain substantial, even as we describe physical processes with increasing accuracy and resolution. Part of the model spread is associated with a lack of understanding of the shortwave cloud feedback (Qu et al., 2018). However, there are several other modeling choices and compromises that contribute to the uncertainty (Flato, 2011). As a consequence, several studies have focused on constraining model results on climate sensitivity on observational data, see e.g., the work of Annan and Hargreaves (2006), or the more recent studies of Cox et al. (2018) and Rypdal et al. (2018b, a). These studies focus on the equilibrium climate sensitivity (ECS) as an essential metric of the climate response, as have numerous paleoclimate studies (Hansen et al., 2013; von der Heydt and Ashwin, 2017; Köhler et al., 2017).

A simpler approach is to adopt a linear approximation, and to apply statistical methods to extract information on the climate response from data on global surface temperature and radiative forcing in the instrumental era. Under the assumption of a linear and stationary response, the global surface temperature anomaly ΔT can be expressed as a filtering of the global radiative



forcing F , mathematically expressed as

$$25 \quad \Delta T(t) = \int_{-\infty}^t G(t-s) (F(s) ds + \sigma dB(s)), \quad (1)$$

where $\sigma dB(t)$ represents a white-noise forcing that gives rise to internal climate variability, and G is the response function, or Green's function, characterizing the relation between forcing and the temperature anomaly. A model of this form can arise from the simplest energy-balance model, i.e. the equations

$$\frac{d\Delta Q}{dt} = -\lambda\Delta T + F \quad (2)$$

30 and $\Delta Q = C\Delta T$, where ΔQ is the change in the system's heat content corresponding to a temperature change ΔT , and C is a heat capacity (Rypdal, 2012). If a white-noise forcing term is included on the right-hand side of Eq. (2) it becomes a stochastic differential equation with a stationary solution on the form of Eq. (1), with $G(t) = C^{-1}e^{-t/\tau}$ and $\tau = C/\lambda$. The process has a natural decomposition into the response to the known forcing,

$$\Delta T_{\text{det}}(t) = \frac{1}{C} \int_{-\infty}^t e^{-(t-s)/\tau} F(s) ds \quad (3)$$

35 and a stochastic term

$$X(t) = \frac{\sigma}{C} \int_{-\infty}^t e^{-(t-s)/\tau} dB(s), \quad (4)$$

which for this particular model is an Ornstein-Uhlenbeck process. Rypdal and Rypdal (2014) show how the parameters of the two terms can be estimated simultaneously from time series of forcing and the GMST using the maximum likelihood (ML) method. They also demonstrate that the resulting process is inconsistent with observations. The stochastic term $X(t)$
40 does not exhibit the strong positive decadal-scale serial correlations that is observed in the GMST in the instrumental era, and secondly, the model's response to reconstructed forcing for the last millennium does not show sufficient low-frequency variability compared to Northern-hemisphere temperature reconstructions.

The inconsistency of the simple energy-balance model is due to the slow climate response associated with the energy exchange with the deep ocean. One can easily incorporate this effect within the framework of Eq. (1), by generalizing the
45 zero-dimensional (one-box) model to a two-box model that includes a layer representing the deep ocean (Geoffroy et al., 2013; Held et al., 2010; Caldeira and Myhrvold, 2013), or the more general m -box model discussed by Fredriksen and Rypdal (2017).

The generalization from the zero-dimensional (one-box) energy balance model to the two-box model, or the m -box models, means that the number of free parameters increases. Concerning statistical inference, this is problematic, and models are prone to over-fitting. Mathematically, the generalization of Eq. (2) is on the form

$$50 \quad \mathbf{C} \frac{d\Delta \mathbf{T}(t)}{dt} = \mathbf{K}\Delta \mathbf{T}(t) + \mathbf{F}(t), \quad (5)$$



where the diagonal elements of \mathbf{C} are the heat capacities of each box, and the matrix \mathbf{K} contains coefficients describing heat exchange between boxes and the feedback parameter λ .

The system in Eq. (5) is solved by bringing the matrix $\mathbf{C}^{-1}\mathbf{K}$ to diagonal form, and the surface temperature anomaly can be written as in Eq. (1) where $G(t)$ is the weighted sum of m exponential functions (Fredriksen and Rypdal, 2017):

$$55 \quad G(t) = \begin{cases} \sum_{k=1}^m w_k e^{-t/\tau_k}, & t \geq 0 \\ 0, & t < 0 \end{cases}, \quad (6)$$

The characteristic time scales $\tau_k = -1/\mu_k$ are defined from the eigenvalues μ_k of $\mathbf{C}^{-1}\mathbf{K}$ and w_k denotes the weight of the k th exponential function.

On the other hand, global temperature variability exhibits an emergent scaling symmetry. For instance, both the forced and the unforced global temperature variability have power spectral densities (PSDs) that are approximate power laws,

$$60 \quad S(f) \sim f^{-\beta} \quad (7)$$

for frequencies corresponding to time scales ranging from months to centuries (Rypdal and Rypdal, 2016; Rybski et al., 2006; Lovejoy and Schertzer, 2013; Huybers and Curry, 2005; Franzke, 2010; Fredriksen and Rypdal, 2016). The global temperature fluctuations are consistent with a fractional Gaussian noise (fGn), which can formally be defined by the integral analogous to Eq. (4), but with the exponential response function replaced with a scale-invariant response function

$$65 \quad G(t) = \left(\frac{t}{\gamma}\right)^{\beta/2-1} \xi. \quad (8)$$

Here, γ is a scale parameter with the dimension of time, and ξ is a variable needed in order for $G(t)$ to have the correct physical dimensions. The scaling exponent β (defined from the PSD in Eq. (7)) relates to the so-called Hurst exponent of the fGn via the formula $\beta = 2H - 1$. Based on this Rypdal and Rypdal (2014) proposed a fractional linear response model in the form of Eq. (1), in which the parsimonious expression in Eq. (8) replaces the linear combination of exponential functions in Eq. (6). The cost of the reduction in model complexity is that the fractional linear response model does not conserve energy, and in general, we cannot write the model as a system of differential equations as in Eq. (5). But on time scales up to approximately 10^3 years, the model provides an accurate description of both forced and unforced surface temperature fluctuations (Rypdal and Rypdal, 2014; Rypdal et al., 2015), and the millennial-scale climate sensitivity in the estimated fractional linear response model correlates strongly with ECS over the ensemble of models in the Coupled Model Intercomparison Project Phase 5 (CMIP5) (Rypdal et al., 2018a).

Since temporal scaling is an emergent property, we cannot deduce the parameters in the fractional linear response model from physical principles. This paper presents a statistical methodology that makes it possible to fit the model to observational data and estimate all model parameters. Parameter estimation is done within a Bayesian framework making use of the methodology of integrated nested Laplace approximation (INLA) for latent Gaussian models introduced in Rue et al. (2009). Barboza et al. (2019) use this framework to investigate model formulations and forcing components in paleoclimate reconstructions.



The INLA-methodology and inference for our statistical model, assuming the scale-invariant response function in Eq. (8), is described further in Section 2. This section explains how to compute the marginal posterior distributions of the model parameters. As the model has a non-standard form, this includes certain modifications of the INLA-methodology to ensure computational efficiency. We discuss applications in Section 3.

85 In Section 3.1 we fit the model to the temperature and forcing data set generated by the GISS-E2-R ESM. Here we show how to extract the GMST response to the known forcing using a Monte Carlo sampling approach. In Section 3.2, the model is used for temperature forecasting where the representative concentration pathway (RCP) trajectories describe the future CO₂ forcing. Section 3.3 describes how the transient climate response (TCR) can be estimated using our model. We obtain estimates for 19 temperature series and their associated adjusted forcing series.

90 We compare the resulting estimates of TCRs with the TCRs obtained directly from the respective ESMs, and with TCR estimates from historical HadCRUT4 temperature data set using different forcing data. The applications are incorporated in the R-package `INLA.climate`. This package also includes the option of using the exponential response function defined by Eq. (3) and Eq. (4). A discussion and final conclusions are given in Section 4.

2 Discrete-time modeling and statistical inference

95 Rypdal and Rypdal (2014) use an ML estimator to estimate the model parameters from the observational yearly time series of $\Delta \mathbf{T} = (\Delta T_1, \dots, \Delta T_n)$ of GMST, and the corresponding vector of radiative forcing $\mathbf{F} = (F_1, \dots, F_n)$. Here, we estimate parameters by adopting a Bayesian framework, making use of the INLA-methodology (Rue et al., 2009, 2017). This approach implies that parameters are treated as stochastic variables and assigned prior distributions. The information given by the priors is then combined with the likelihood of the observations and updated to give posterior distributions using Bayes' theorem.

100 In a discrete-time model, we assume that ΔT_t has a Gaussian distribution with a random mean expressed by the linear predictor

$$\eta_t = \sigma_f \sum_{s=1}^t (G_{ts}(H) F_s + F_0) + \varepsilon_t, \quad t = 1, \dots, n \quad (9)$$

where $\sigma_f = \gamma^{-\beta/2+1}$ while F_0 denotes a shift parameter which gives the initial forcing value. G_{ts} denotes a discretely indexed element of the function,

$$105 \quad G_{ts}(H) = \begin{cases} (t - s + \frac{1}{2})^{H-\frac{3}{2}}, & 1 \leq s \leq t \leq n \\ 0, & \text{otherwise} \end{cases} \quad (10)$$

Further, the vector $\varepsilon = (\varepsilon_1, \dots, \varepsilon_n)$ denotes a zero-mean fGn process, implying that the covariance between ε_t and ε_s is

$$\Sigma_{ts} = \frac{\sigma_\varepsilon^2}{2} (|t - s + 1|^{2H} + |t - s - 1|^{2H} - 2|t - s|^{2H}), \quad t, s = 1, \dots, n, \quad (11)$$



where $\sigma_\varepsilon = \sigma\sigma_f$. In vector notation, the predictor is then given by

$$\boldsymbol{\eta} = \boldsymbol{\mu} + \varepsilon \quad (12)$$

110 where

$$\boldsymbol{\mu} = \boldsymbol{\mu}(H, \sigma_f, F_0) = \sigma_f \mathbf{G}(H) (\mathbf{F} + F_0). \quad (13)$$

The covariance matrix of the predictor is $\boldsymbol{\Sigma} = \boldsymbol{\Sigma}(H, \sigma_\varepsilon)$ with the elements in Eq. (11). Notice that the matrix $\mathbf{G}(H)$ is lower triangular with elements given by Eq. (10). The given formulation implies that the vector $\boldsymbol{\mu}$ represents the GMST response to the known forcing \mathbf{F} while ε is the GMST response to the random forcing, i.e. the unforced climate variability.

115 The statistical regression formulation in Eq. (9) has a hierarchical structure in which the expected temperature anomalies are modelled in terms of the random predictor $\boldsymbol{\eta}$ with elements specified by Eq. (9). The predictor depends on additional model parameters $\boldsymbol{\theta} = (H, \sigma_\varepsilon, \sigma_f, F_0)$. This set-up implies that we need to assign priors, both to the predictor and to the model parameters. By assigning a Gaussian prior to $\boldsymbol{\eta}$, the resulting model becomes a latent Gaussian model, which can be analyzed using the INLA-methodology. In general, this class of models introduces a latent Gaussian field \mathbf{x} , which contains
 120 all the random components of a linear predictor, including the predictor itself. In our case, the latent field is equal to the linear predictor, $\mathbf{x} = \boldsymbol{\eta} = \boldsymbol{\mu} + \varepsilon$. However, inference for this model is not straightforward as the model parameter H appears in both of the terms $\boldsymbol{\mu}$ and ε . We choose to circumvent this problem by considering the sum $\boldsymbol{\mu} + \varepsilon$ as a single model component, i.e., as a fractional Gaussian noise process with mean vector $\boldsymbol{\mu}$ and covariance matrix $\boldsymbol{\Sigma}$. The dependence between two components implies that we will not get separate posterior estimates for $\boldsymbol{\mu}$ and ε , directly.

125 Using $p(\cdot)$ as a generic notation for probability density functions, we can summarize the three-stage hierarchical structure of latent Gaussian models, including distributional assumptions, as follows:

- The first stage specifies the likelihood of the model. The observed temperature anomaly ΔT_t is assigned a Gaussian distribution with negligible fixed variance and mean η_t . The observations are assumed to be conditionally independent given the latent field \mathbf{x} and parameters $\boldsymbol{\theta}$, i.e.

$$130 \quad p(\Delta \mathbf{T} | \mathbf{x}, \boldsymbol{\theta}) = \prod_{t=1}^n p(\Delta T_t | x_t, \boldsymbol{\theta}).$$

- The second stage specifies the prior distribution for the latent field. Given the parameters $\boldsymbol{\theta}$, the latent field \mathbf{x} is assigned a Gaussian prior distribution with mean vector $\boldsymbol{\mu}_x = \mathbb{E}[\mathbf{x} | \boldsymbol{\theta}]$ and precision matrix, $\mathbf{Q} = \mathbf{Q}(H, \sigma_\varepsilon)$, defined as the inverse covariance matrix, i.e.

$$p(\mathbf{x} | \boldsymbol{\theta}) = \sqrt{\frac{\det \mathbf{Q}}{(2\pi)^n}} \exp\left(-\frac{1}{2}(\mathbf{x} - \boldsymbol{\mu}_x)^T \mathbf{Q}(\mathbf{x} - \boldsymbol{\mu}_x)\right).$$

- 135 – The third stage specifies independent priors for the parameters:

$$p(\boldsymbol{\theta}) = p(H)p(\sigma_\varepsilon)p(\sigma_f)p(F_0).$$



The shift parameter F_0 is assigned a zero-mean Gaussian prior, while the other parameters are assigned penalised complexity (PC) priors (Simpson et al., 2017). The class of PC priors represents a recently developed framework to compute priors based on specific principles, including support to Occam’s razor. The PC prior of the two scaling parameters σ_f and σ_ϵ can be computed to equal the exponential distribution while the PC prior of H is computed numerically (Sørbye and Rue, 2018).

The joint posterior for all components of the latent field and all of the model parameters is then summarized by

$$p(\mathbf{x}, \boldsymbol{\theta} \mid \Delta \mathbf{T}) \propto \prod_{t=1}^n p(\Delta T_t \mid x_t, \boldsymbol{\theta}) p(\mathbf{x} \mid \boldsymbol{\theta}) p(\boldsymbol{\theta}).$$

Our main objective is to estimate the marginal posterior distribution for all components of the latent field

$$p(x_t \mid \Delta \mathbf{T}) = \int p(x_t \mid \boldsymbol{\theta}, \Delta \mathbf{T}) p(\boldsymbol{\theta} \mid \Delta \mathbf{T}) d\boldsymbol{\theta}, \quad t = 1, \dots, n \quad (14)$$

and the marginal posteriors for all the model parameters

$$p(\theta_j \mid \Delta \mathbf{T}) = \int p(\boldsymbol{\theta} \mid \Delta \mathbf{T}) d\boldsymbol{\theta}_{-j}, \quad j = 1, \dots, 4. \quad (15)$$

Here, the notation $\boldsymbol{\theta}_{-j}$ is used to denote the vector $\boldsymbol{\theta}$ excluding the j th parameter. The posterior distributions provide a complete description of the latent field components and the parameters in our model. From the marginals in Eq. (14)–Eq. (15) we can extract summary statistics such as the mean, variance, quantiles and credible intervals.

Traditionally, marginal posterior distributions have been approximated using Markov chain Monte Carlo methods (Robert and Casella, 1999). Such methods are simulation-based and can potentially be very time-consuming for hierarchical models. The INLA-methodology represents a computationally superior, but still accurate, alternative and is available using the R-package `R-INLA`. This package can be downloaded for free at www.r-inla.org. INLA provides a deterministic approach, approximating the posterior distributions in Eq. (14)–Eq. (15) using numerical optimization techniques, interpolations and numerical integration. Among others, this includes the use of the Laplace approximation (Tierney and Kadane, 1986) which is an old technique to compute high-dimensional integrals. Specifically, the joint posterior distribution for the model parameters in Eq. (15) is approximated by employing a Laplace approximation evaluated at the mode $\mathbf{x}^*(\boldsymbol{\theta})$:

$$p(\boldsymbol{\theta} \mid \Delta \mathbf{T}) \approx \frac{p(\mathbf{x}, \boldsymbol{\theta}, \Delta \mathbf{T})}{p_G(\mathbf{x} \mid \boldsymbol{\theta}, \Delta \mathbf{T})} \Bigg|_{\mathbf{x}=\mathbf{x}^*(\boldsymbol{\theta})}, \quad (16)$$

where $p_G(\mathbf{x} \mid \boldsymbol{\theta}, \Delta \mathbf{T})$ is a Gaussian approximation of

$$p(\mathbf{x} \mid \boldsymbol{\theta}, \Delta \mathbf{T}) \propto p(\mathbf{x} \mid \boldsymbol{\theta}) p(\Delta \mathbf{T} \mid \mathbf{x}, \boldsymbol{\theta}).$$

This approximation is usually very accurate as we know that $p(\mathbf{x} \mid \boldsymbol{\theta})$ is already Gaussian. The marginal for each model parameter is then obtained by assuming a normal distribution modified to allow for skewness,

$$p(\theta_j \mid \Delta \mathbf{T}) \approx \begin{cases} \mathcal{N}(0, \sigma_{j+}^2), & \theta_j > 0 \\ \mathcal{N}(0, \sigma_{j-}^2), & \theta_j \leq 0 \end{cases}.$$



165 The scaling parameters σ_{j+} and σ_{j-} are found using the approximate joint posterior distribution of Eq. (16), see Martins et al. (2013) for details. To compute Eq. (14), the Laplace approximation in Eq. (16) is combined with a simplified and computationally faster version of the Laplace approximation of $p(x_t | \theta, \Delta \mathbf{T})$. Finally, the integrand of Eq. (14) is evaluated for values of θ in a grid efficiently covering the parameter space for θ , see Rue et al. (2009) and Rue et al. (2017) for details.

A key assumption for the numerical approximations to be computationally efficient is that the latent Gaussian field \mathbf{x} has Markov properties, i.e. \mathbf{x} needs to be a Gaussian Markov random field having a sparse precision matrix \mathbf{Q} (Rue and Held, 2005). This is not the case for fGn as the long-range dependency structure of this process gives a dense precision matrix. We resolve this problem by approximating ε as a weighted sum of m independent first-order autoregressive (AR(1)) processes, i.e.

$$\tilde{\varepsilon} = \sum_{i=1}^m \sqrt{w_i} \tilde{\mathbf{x}}_i.$$

To capture the correlation structure between $\tilde{\varepsilon}$ and each of the AR(1) processes $\tilde{\mathbf{x}}_i$, the latent field must be extended to also include the underlying AR(1) processes, i.e. $\mathbf{x} = (\boldsymbol{\eta}, \boldsymbol{\mu} + \tilde{\varepsilon}, \tilde{\mathbf{x}}_1, \dots, \tilde{\mathbf{x}}_m)$. The weights $\{w_i\}_{i=1}^m$ and the first-lag autocorrelation coefficients of the AR(1) processes are selected such that the resulting autocorrelation function of $\tilde{\varepsilon}$ best approximates that of fGn. In addition to ensuring computational efficiency, this approximation also proves to be remarkably accurate. For further details about this approximation, see Sørbye et al. (2019) who also provide a discussion from a statistical perspective. For a physical interpretation of this approximation we refer to Fredriksen and Rypdal (2017).

180 Currently, there are no built-in model components in R-INLA which suit our specifications. This means that we have to construct one manually using `rgeneric`, a modeling tool that allows generic model components to be defined for INLA. To make this accessible to applied scientists we have developed an R-package called `INLA.climate` which includes functions that take care of the technical part of the fitting procedure and presents important information and summary statistics in a readable format. This package contains a versatile and user-friendly interface to fit the model in Eq. (9) and includes functions to replicate all results presented in this paper. The package is available at the GitHub repository www.github.com/eirikmn/INLA.climate. Detailed description of the package and its features is available in its accompanying documentation.

3 Applications

3.1 Estimating the forced temperature response

As explained in Section 2, our model formulation implies that the sum $\boldsymbol{\mu} + \varepsilon$ is viewed as one model component. Consequently, INLA will give an estimate for the posterior distribution of the sum, and not the marginal posterior distributions for each of the terms $\boldsymbol{\mu}$ and ε .

In this example, we illustrate how we can approximate the marginal posterior distribution for the temperature response attributed to the known forcing, $p(\mu_i | \Delta \mathbf{T})$, combining INLA with Monte Carlo sampling. We first fit our model to the GISS-E2-R temperature and the forcing data using INLA. This gives the estimated marginal posterior distributions for each of the model parameters $\theta = (H, \sigma_\varepsilon, \sigma_f, F_0)$, as shown in Fig. 1. Next, we use the `inla.hyperpar.sample` function from the

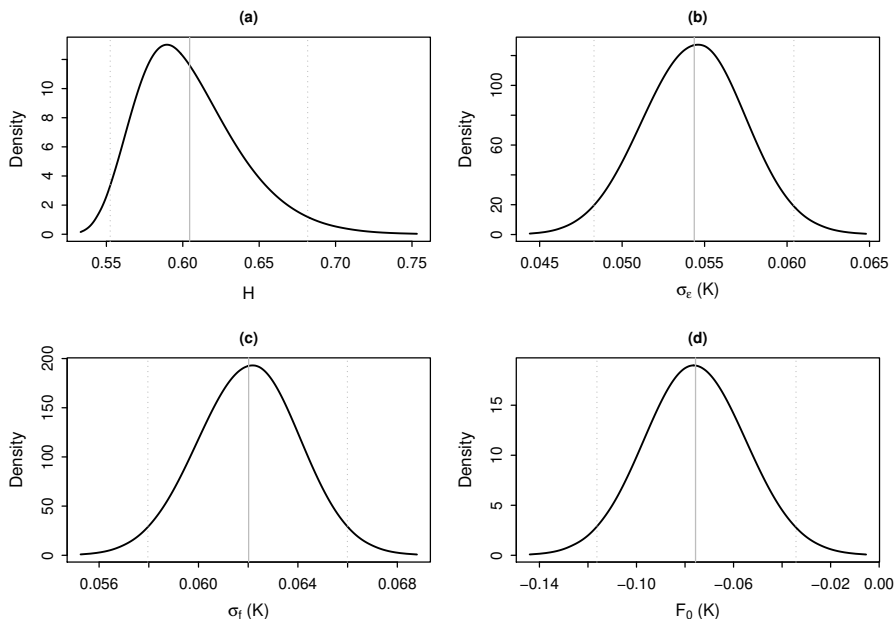


Figure 1. The marginal posterior distributions of the parameters, obtained using `INLA.climate` to fit our model to the GISS-E2-R temperature and forcing dataset. The vertical lines show the mean and 95 % credible intervals.

R-INLA package to draw 100,000 samples from the approximate joint posterior distribution of H, σ_f and F_0 . For each of these samples, we compute μ according to Eq. (13). The resulting samples give approximate marginal posterior distributions for each μ_i which can then be used to calculate summary statistics.

For comparison, we apply the same approach to estimate the given marginal posterior distributions under the assumption of an exponential response function in Eq. (3). In this case, the discretized unforced response described in Eq. (4) is an AR(1) process. For both the scale-invariant and exponential response functions, we can then compute the marginal posterior means and 95 % credible intervals for each μ_i . The results are shown in Fig. 2. The marginal posterior means are very similar. However, we observe significantly wider credible intervals for the model using an exponential response function. The larger uncertainty suggests that a smaller portion of the variance is explained by the unforced climate variability, leaving more of the variation to be explained by the response to the known forcing. Using the `INLA.climate` package, we obtain full inference in seconds on a personal computer. The code to run the example is as follows:

```
data("GISS_E2_R")
y = GISS_E2_R$Temperature
z = GISS_E2_R$Forcing
```



```
210 r.scaling = inla.climate(y,z,compute.mu="full")  
r.exponential = inla.climate(y,z,compute.mu="full",m=1,model="ar1")
```

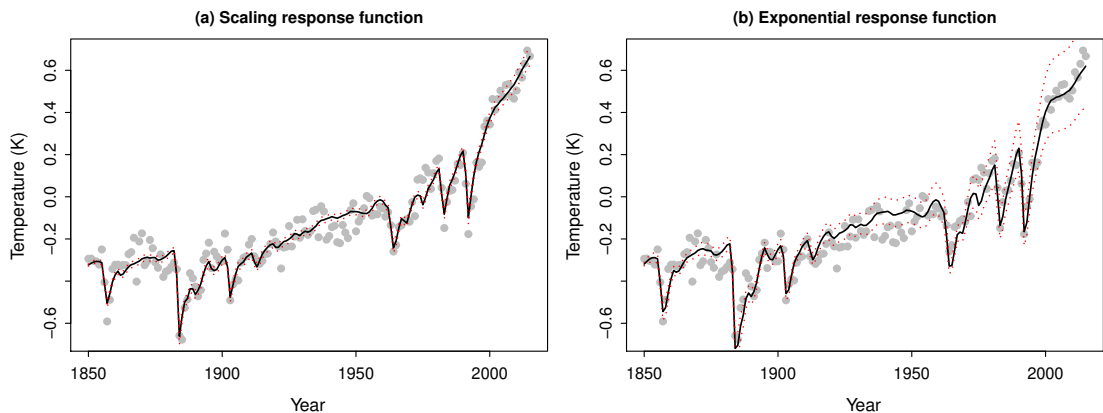


Figure 2. The marginal posterior mean and 95 % credible intervals of the temperature response to known forcing μ obtained by 100,000 Monte Carlo simulations compared to GISS-E2-R temperature data. Panel (a) shows the results under the scaling assumption, and panel (b) shows the results using an exponential response.

3.2 Temperature predictions for Representative Concentration Pathway trajectories

Once trained on historical temperature and forcing data, the response model can easily be used to obtain temperature predictions for different future forcing scenarios. Here, we present global temperature predictions for the years 2016 to 2100 based on the
215 HADCRUT4 temperature data and the greenhouse gas component of the Hansen forcing data for 1850 to 2015. For future forcing, we use the representative concentration pathways (RCPs), RCP2.6 (van Vuuren et al., 2007), RCP4.5 (Clarke et al., 2007; Smith and Wigley, 2006; Wise et al., 2009), RCP6 (Fujino et al., 2006; Hijioka et al., 2008) and RCP8.5 Riahi et al. (2007). These trajectories were first published in 2000 and cover the years 2000 to 2100. In our analyses, we use the RCP for the year 2016 to the year 2100 and adjust each of them so that the forcing in 2015 equals the greenhouse gas forcing in Hansen
220 data in 2015. The forcing scenarios are shown in Fig. 3.

Prediction is carried out using `INLA.climate` by appending the future scenario to the forcing of the past $\mathbf{F} = (\mathbf{F}_{\text{past}}, \mathbf{F}_{\text{future}})$. The package automatically replaces missing observations with NA values and give predictions for these based on the model fitted to the observed data.

As in the previous example, we compare the results using the scale-invariant versus an exponential response function.
225 Training and predictions only take seconds to carry out on a personal computer. Fig. 4 shows the marginal posterior means and 95 % credible intervals using a scaling response, and Fig. 5 show the same results using an exponential response. The figures

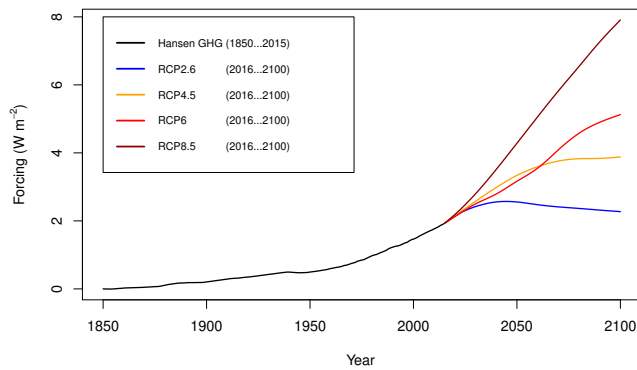


Figure 3. The greenhouse gas component of the Hansen forcing (black) followed by the RCP2.6 (blue), RCP4.5 (orange), RCP6 (red) and RCP8.5 (dark red) forcing scenarios.

also show comparisons with the AR5 projections listed in table SPM.2 in IPCC (2013b). We observe that the exponential response model fails to describe the persistence in the temperature response and underestimates the global warming increase projections. The predictions obtained using a scale-invariant response predict higher future temperatures.

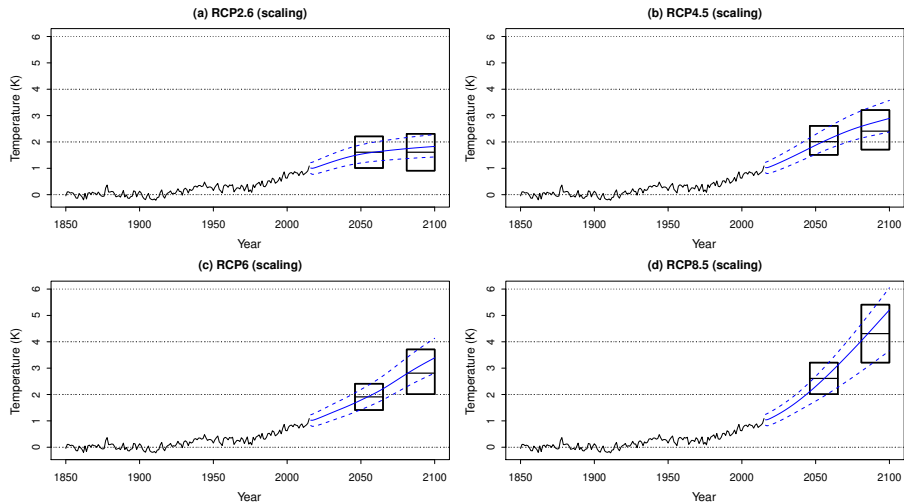


Figure 4. Panels (a)–(d) describe the marginal posterior means and 95 % credible intervals of the predicted temperature response to future forcing according to the RCP2.6, RCP4.5, RCP6 and RCP8.5 trajectories, respectively, using a scaling response function. These are compared to the AR5 projections (black boxes).

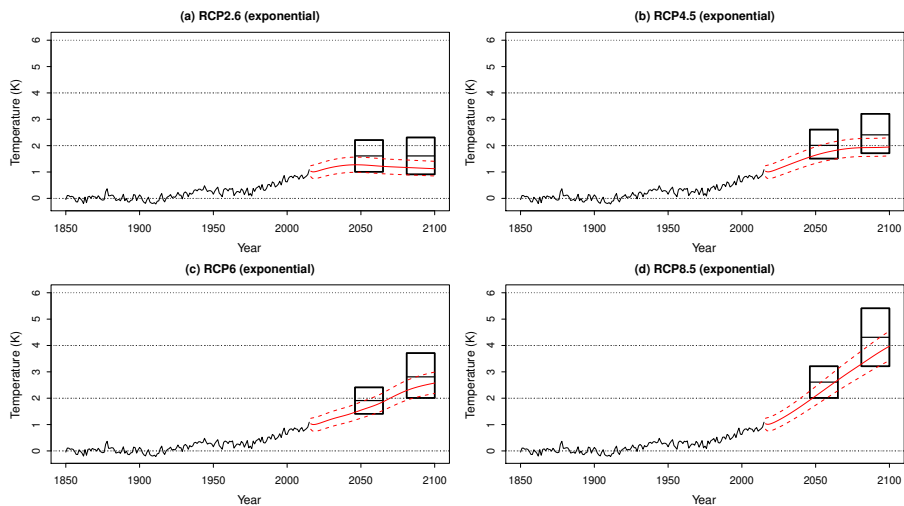


Figure 5. Panels (a)–(d) describe the marginal posterior means and 95 % credible intervals of the predicted temperature response to future forcing according to the RCP2.6, RCP4.5, RCP6 and RCP8.5 trajectories, respectively, using an exponential response function. These are compared to the AR5 projections (black boxes).



230 3.3 Estimating the transient climate response

As a final application, we describe how our suggested method can be used to estimate the TCR. The TCR is defined as the average temperature response between 60 and 80 years following a gradual CO₂-doubling, assuming a 1 % annual increase. In this scenario, the forcing increases linearly according to

$$f(s) = \frac{Q_{2 \times \text{CO}_2}}{70 \text{ yrs}} (s + F_0), \quad \text{for } s = 1, \dots, 80 \text{ yrs.}$$

235 Here, $Q_{2 \times \text{CO}_2}$ is a model-specific coefficient describing the forcing corresponding to a CO₂ doubling. We obtain these coefficients from Forster et al. (2013) for all ESMs analyzed in this paper.

The computation of TCR is carried out by inserting the forcing into Eq. (1) and performing the matrix multiplication

$$\mathbf{v} = \sigma_f \mathbf{G}(H) \mathbf{f}.$$

240 where $\mathbf{G}(H)$ is the 80×80 matrix with elements defined as in Eq. (10) and $\mathbf{f} = (f(1), \dots, f(80))^T$. This implies that TCR is computed by

$$\text{TCR} = \frac{1}{20 \text{ yrs}} \sum_{t=60 \text{ yrs}}^{80 \text{ yrs}} v_t. \quad (17)$$

As in Section 3.1, the approximate marginal posterior distribution for TCR is obtained by combining INLA with Monte Carlo sampling. We first generate samples from the joint posterior distribution of the model parameters $p(\boldsymbol{\theta} \mid \Delta \mathbf{T})$. For each of these samples, we calculate TCR, which then gives the approximate posterior distribution for TCR.

245 For our analyses, we use temperature data sets generated from 19 ESMs in the Coupled Model Intercomparison Project Phase 5 (CMIP5) ensemble, see Table 2. We obtain the forcing by combining the forcing data from Forster et al. (2013) and Hansen et al. (2010) such that the 18-yr moving averages of the two are equal. We use the instrumental HadCRUT dataset (Morice et al., 2012), which combines the land temperatures of the CRU dataset (Jones et al., 2012) with the sea surface temperatures of HadSST3 (Kennedy et al., 2011).

250 To assess the accuracy of the TCR estimations from Eq. (12) we compare the estimates from each of the 19 ESMs with the TCR obtained from the ESMs directly (Forster et al., 2013). Inference is obtained by producing one hundred thousand Monte Carlo simulations of the TCR. Summary statistics for our model are shown in Tables 3–4, which includes the marginal posterior means and 95 % credible intervals for the TCR and the model parameters used to compute it.

To assess the approach using the scale-invariant versus the exponential response function, we compare the posterior mean estimates with the values obtained directly from the ESMs. Specifically, we calculate the bias, the root mean square error (rmse) and the correlation between the posterior mean estimates and the TCR-values from the ESMs, see Table 1. We observe that the scale-invariant response performs better in all three cases. However, both approaches seem to indicate strong correlations, which is depicted more clearly in the scatter plots shown in Fig. 6. Using `INLA.climate` we obtained, for a typical analysis, inference in around 13 seconds using a scale-invariant response and 35 seconds using an exponential response.

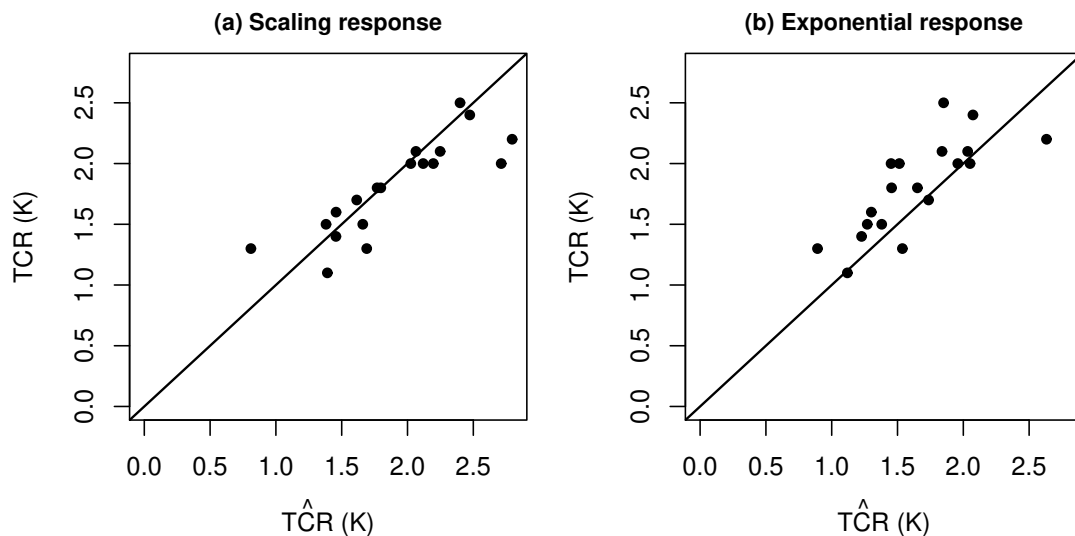


Figure 6. Scatter plot of the TCR obtained directly from the 19 ESMs against the corresponding marginal posterior mean estimates when using a scale-invariant response function (panel (a)) and an exponential response function (panel (b)).

260 To obtain estimates for the TCR of the HadCRUT4 data set we use the 19 different forcing data associated with the ESMs
enlisted in Table: 2 as well as the Hansen radiative forcing which we will assign ID number 0. The Monte Carlo simulations are
carried out separately for each forcing data set, using one hundred thousand samples and forcing slope coefficient $Q_{2\times\text{CO}_2} =$
 3.8 W m^{-2} (IPCC, 2013a). This is again performed using both a scale-invariant response and an exponential response. For
the scale-invariant response, the posterior means and credibility intervals of the TCR and the parameters used to compute the
265 TCR for each ESM are shown in Tables 5–6. The marginal posterior mean estimates and 95 % credible intervals for the TCR
using both approaches are illustrated in Fig. 7 where we observe wider credible intervals when using an exponential response
function. We obtain an estimated posterior distribution for the TCR across all models by aggregating all TCR samples obtained
from each analysis, totaling two million simulations. The posterior density is obtained from the Monte Carlo samples using the
density function in R. The resulting density function is depicted in Fig. 8, where it is compared with a histogram describing
270 the TCRs obtained directly from the ESMs. We observe a mean of 1.53 K and 1.46 K, and standard deviation of 0.33 K and
0.46 K when using a scale-invariant and an exponential response function, respectively. Both estimates fall in the lower half of
the range of TCRs.

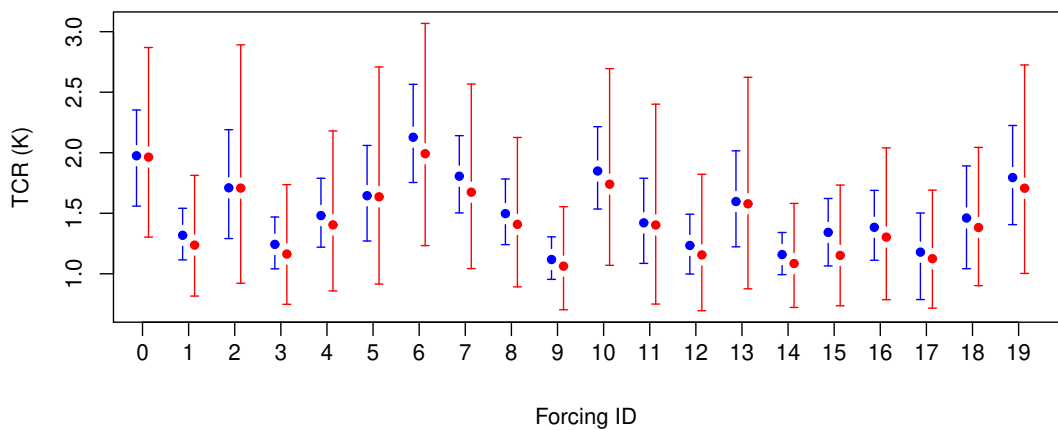


Figure 7. The posterior mean estimates and 95 % credible intervals of the historical TCR for all forcing data sets using a the scale-invariant response function (blue) and the exponential response function (red). ID number 0 denotes the Hansen forcing.

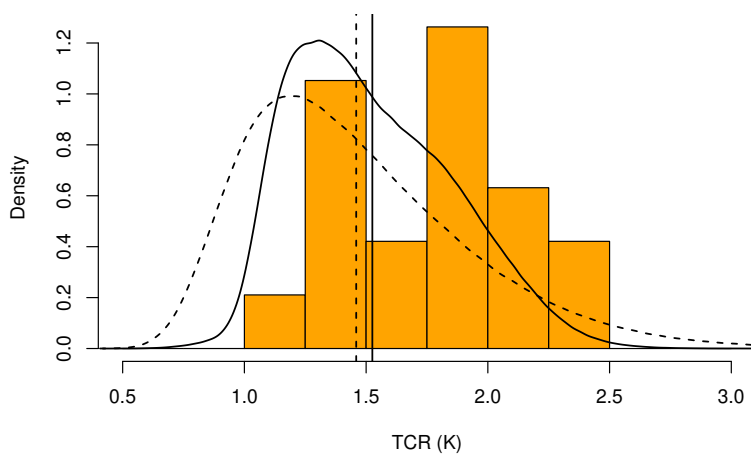


Figure 8. Histogram of the TCR obtained from the different ESMs with the posterior density function estimated from the Monte Carlo simulations using both an exponential (dashed) and scaling response (solid). The vertical lines describes the means of the two approaches.



4 Conclusions

This paper presents a Bayesian formulation to analyse a linear temperature response model to radiative forcing, incorporating
275 long-range temporal dependence using a scale-invariant response function. Computational efficiency is achieved by incorporat-
ing the model within the R-INLA framework and adopting the approximation introduced in Sørbye et al. (2019). The benefits
of this methodology are three-fold. First, the model is both accessible and adaptable to more advanced models that require
more trends and effects. Second, the approximations ensure low costs in both computational complexity and memory, even for
long time series. Third, the method yields full Bayesian inference, giving a full description of the behavior of the time variables
280 and model parameters.

In addition to providing parameter estimates, the model has been used to produce temperature predictions as responses to
the four RCP forcing trajectories used to describe future radiative forcing. For comparison, we have also included prediction
results using the simple 1-box model having an exponential response function. We observe that the exponential response models
underestimate the predicted temperature compared to the projections made by the IPCC. On the other hand, the scale-invariant
285 response models tend to overestimate future temperatures but are overall more accurate than using an exponential response
function.

We further demonstrate that the model can be used to estimate the transient climate response in instrumental data. Our best
estimate is that the TCR is 1.53 K with a standard deviation of 0.33 K. This estimate falls right in the middle of the range put
forward in the IPCC report (0.8 – 2.5 K) and the accuracy is consistent with the TCR obtained directly from the ESMs. The
290 presented model has also been seen to give coherent estimates for the equilibrium climate sensitivity, compared with running
ESMs (Rypdal et al., 2018a).

Accurate linear response models for global temperature are essential alternatives to ESMs in studies where one needs to
explore a large number of emission scenarios, and the modeling framework presented here can easily be included in integrated
assessment models. Moreover, since the models are invertible, they can efficiently compute forcing scenarios corresponding to
295 given future scenarios for global temperatures. Hence, in combination with linear models for the CO₂ response to emissions,
they can be used to obtain observation-based estimates of the remaining carbon budget in scenarios where we reach the goals
of the Paris agreement.

In combination with dedicated ESM experiments, the methods presented in this paper can also be used to estimate global
and regional climate sensitivity as a function of background state and time scale. One can use such estimates to study the effect
300 of non-linear responses across time scales and to obtain insight into how sensitivities and fluctuations change in the vicinity of
climate tipping points.

Code and data availability. The code and data sets used for this paper is available through the R-package, `INLA.climate`, which can be
downloaded from: github.com/eirikmn/INLA.climate.



Author contributions. All authors conceived and designed the study; H.-B.F. collected data and constructed the modified forcing data. E.M.-
305 N. implemented the model, performed all of the analyses and developed the R-package `INLA.climate`. H.R provided some technical
support related to R-INLA. E.M.-N., S.H.S and M.R. discussed the results and wrote the paper.

Competing interests. The authors declare that they have no conflict of interest

Acknowledgements. The authors thank K. Rypdal for useful discussions. This project has received funding from the European Union's
Horizon 2020 research and innovation programme under grant agreement No. 820970.



310 References

- Annan, J. D. and Hargreaves, J. C.: Using multiple observationally-based constraints to estimate climate sensitivity, *Geophys. Res. Lett.*, 33, L06704, 2006.
- Barboza, L. A., Emile-Geay, J., Li, B., and He, W.: Efficient Reconstructions of Common Era Climate via Integrated Nested Laplace Approximations, *J. Agr. Biol. Envir. St.*, 24, 535–554, 2019.
- 315 Bentsen, M., Bethke, I., Debernard, J. B., Iversen, T., Kirkevåg, A., Seland, Ø., Drange, H., Roelandt, C., Seierstad, I. A., Hoose, C., and Kristjánsson, J. E.: The Norwegian Earth System Model, NorESM1-M - Part 1: Description and basic evaluation of the physical climate, *Geosci. Model Dev.*, 6, 687–720, 2013.
- Bi, D., Dix, M., Marsland, S., O’Farrell, S., Rashid, H., Uotila, P., H., Kowalczyk, E., G., Sullivan, A., Y., H., Franklin, C., S., V., W., Zhou, K., Fiedler, R., Collier, M., and Puri, K.: The ACCESS coupled model: Description, control climate and evaluation, *Aust. Meteorol. Ocean*, 63, 41–64, 2012.
- 320 Caldeira, K. and Myhrvold, N. P.: Projections of the pace of warming following an abrupt increase in atmospheric carbon dioxide concentration, *Environ. Res. Lett.*, 8, 034039, 2013.
- Chylek, P., Li, J., Dubey, M. K., Wang, M., and Lesins, G.: Observed and model simulated 20th century Arctic temperature variability: Canadian Earth System Model CanESM2, *Atmos. Chem. Phys. Discuss*, 11, 22893–22907, 2011.
- 325 Clarke, L., Edmonds, J., Jacoby, H., Pitcher, H., Reilly, J., and Richels, R.: Scenarios of Greenhouse Gas Emissions and Atmospheric Concentrations, sub-report 2.1A of Synthesis and Assessment Product 2.1 by the U.S. Climate Change Science Program and the Subcommittee on Global Change Research. Department of Energy, Office of Biological Environmental Research, 2007.
- Collins, W. J., Bellouin, N., Doutriaux-Boucher, M., Gedney, N., Halloran, P., Hinton, T., Hughes, J., Jones, C. D., Joshi, M., Liddicoat, S., Martin, G., O’Connor, F., Rae, J., Senior, C., Sitch, S., Totterdell, I., Wiltshire, A., and Woodward, S.: Development and evaluation of an
- 330 Earth-System model - HadGEM2, *Geosci. Model Dev.*, 4, 1051–1075, 2011.
- Cox, P. M., Huntingford, C., and Williamson, M.: Emergent constraint on equilibrium climate sensitivity from global temperature variability, *Nature*, 553, 319–322, 2018.
- Donner, L. J., Wyman, B. L., Hemler, R. S., Horowitz, L. W., Ming, Y., Zhao, M., Golaz, J.-C., Ginoux, P., Lin, S.-J., Schwarzkopf, M. D., Austin, J., Alaka, G., Cooke, W. F., Delworth, T. L., Freidenreich, S. M., Gordon, C. T., Griffies, S. M., Held, I. M., Hurlin, W. J., Klein,
- 335 S. A., Knutson, T. R., Langenhorst, A. R., Lee, H.-C., Lin, Y., Magi, B. I., Malyshev, S. L., Milly, P. C. D., Naik, V., Nath, M. J., Pincus, R., Ploshay, J. J., Ramaswamy, V., Seman, C. J., Shevliakova, E., Sirutis, J. J., Stern, W. F., Stouffer, R. J., Wilson, R. J., Winton, M., Wittenberg, A. T., and Zeng, F.: The Dynamical Core, Physical Parameterizations, and Basic Simulation Characteristics of the Atmospheric Component AM3 of the GFDL Global Coupled Model CM3, *J. Climate*, 24, 3484–3519, 2011.
- Dufresne, J.-L., Foujols, M.-A., Denvil, S., Caubel, A., Marti, O., Aumont, O., Balkanski, Y., Bekki, S., Bellenger, H., Benschila, R., Bony, S., Bopp, L., Braconnot, P., Brockmann, P., Cadule, P., Cheruy, F., Codron, F., Cozic, A., Cugnet, D., de Noblet, N., Duvel, J.-P., Ethé, C., Fairhead, L., Fichefet, T., Flavoni, S., Friedlingstein, P., Grandpeix, J.-Y., Guez, L., Guilyardi, E., Hauglustaine, D., Hourdin, F., Idelkadi,
- 340 A., Ghattas, J., Joussaume, S., Kageyama, M., Krinner, G., Labetoulle, S., Lahellec, A., Lefebvre, M.-P., Lefevre, F., Levy, C., Li, Z. X., Lloyd, J., Lott, F., Madec, G., Mancip, M., Marchand, M., Masson, S., Meurdesoif, Y., Mignot, J., Musat, I., Parouty, S., Polcher, J., Rio, C., Schulz, M., Swingedouw, D., Szopa, S., Talandier, C., Terray, P., Viovy, N., and Vuichard, N.: Climate change projections using the
- 345 IPSL-CM5 Earth System Model: from CMIP3 to CMIP5, *Clim. Dynam.*, 40, 2123–2165, 2013.



- Dunne, J. P., John, J. G., Adcroft, A. J., Griffies, S. M., Hallberg, R. W., Shevliakova, E., Stouffer, R. J., Cooke, W., Dunne, K. A., Harrison, M. J., Krasting, J. P., Malyshev, S. L., Milly, P. C. D., Philipps, P. J., Sentman, L. T., Samuels, B. L., Spelman, M. J., Winton, M., Wittenberg, A. T., and Zadeh, N.: GFDL's ESM2 Global Coupled Climate–Carbon Earth System Models. Part I: Physical Formulation and Baseline Simulation Characteristics, *J. Climate*, 25, 6646–6665, 2012.
- 350 Dunne, J. P., John, J. G., Shevliakova, E., Stouffer, R. J., Krasting, J. P., Malyshev, S. L., Milly, P. C. D., Sentman, L. T., Adcroft, A. J., Cooke, W., Dunne, K. A., Griffies, S. M., Hallberg, R. W., Harrison, M. J., Levy, H., Wittenberg, A. T., Phillips, P. J., and Zadeh, N.: GFDL's ESM2 Global Coupled Climate–Carbon Earth System Models. Part II: Carbon System Formulation and Baseline Simulation Characteristics, *J. Climate*, 26, 2247–2267, 2013.
- Flato, G. M.: Earth system models: an overview, *WIREs Clim. Change*, 2, 783–800, 2011.
- 355 Forster, P. M., Andrews, T., Good, P., Gregory, J. M., Jackson, L. S., and Zelinka, M.: Evaluating adjusted forcing and model spread for historical and future scenarios in the CMIP5 generation of climate models, *J. Geophys. Res.-Atmos.*, 118, 1139–1150, 2013.
- Franzke, C.: Long-Range Dependence and Climate Noise Characteristics of Antarctic Temperature Data, *J. Climate*, 23, 6074–6081, 2010.
- Fredriksen, H.-B. and Rypdal, K.: Spectral characteristics of instrumental and climate model surface temperatures, *J. Climate*, 29, 1253–1268, 2016.
- 360 Fredriksen, H.-B. and Rypdal, M.: Long-Range Persistence in Global Surface Temperatures Explained by Linear Multibox Energy Balance Models, *J. Climate*, 30, 7157–7168, 2017.
- Fujino, J., Nair, R., Kainuma, M., Masui, T., and Matsuoka, Y.: Multi-gas Mitigation Analysis on Stabilization Scenarios Using Aim Global Model, *Energy J.*, 27, 343–353, 2006.
- Gent, P. R., Danabasoglu, G., Donner, L. J., Holland, M. M., Hunke, E. C., Jayne, S. R., Lawrence, D. M., Neale, R. B., Rasch, P. J., 365 Vertenstein, M., Worley, P. H., Yang, Z.-L., and Zhang, M.: The Community Climate System Model Version 4, *J. Climate*, 24, 4973–4991, 2011.
- Geoffroy, O., Saint-Martin, D., Olivié, D. J. L., Voldoire, A., Bellon, G., and Tytéca, S.: Transient climate response in a two-layer energy-balance model. Part I: Analytical solution and parameter calibration using CMIP5 AOGCM experiments, *J. Climate*, 26, 1841–1857, 2013.
- 370 Giorgetta, M. A., Jungclaus, J., Reick, C. H., Legutke, S., Bader, J., Böttinger, M., Brovkin, V., Crueger, T., Esch, M., Fieg, K., Glushak, K., Gayler, V., Haak, H., Hollweg, H.-D., Ilyina, T., Kinne, S., Kornblueh, L., Matei, D., Mauritsen, T., Mikolajewicz, U., Mueller, W., Notz, D., Pithan, F., Raddatz, T., Rast, S., Redler, R., Roeckner, E., Schmidt, H., Schnur, R., Segschneider, J., Six, K. D., Stockhause, M., Timmreck, C., Wegner, J., Widmann, H., Wieners, K.-H., Claussen, M., Marotzke, J., and Stevens, B.: Climate and carbon cycle changes from 1850 to 2100 in MPI-ESM simulations for the Coupled Model Intercomparison Project phase 5, *H. Adv. Model. Earth Sy.*, 375 5, 572–597, 2013.
- Hansen, J., Ruedy, R., Sato, M., and Lo, K.: Global surface temperature change, *Rev. Geophys.*, 48, RG4004, 2010.
- Hansen, J., Sato, M., Russell, G., and Kharecha, P.: Climate sensitivity, sea level and atmospheric carbon dioxide, *Philos. Trans. Royal Soc. A*, 371, 20120294, 2013.
- 380 Held, I. M., Winton, M., Takahashi, K., Delworth, T., Zeng, F., and Vallis, G. K.: Probing the fast and slow components of global warming by returning abruptly to preindustrial forcing, *J. Climate*, 23, 2418–2427, 2010.
- Hijioka, Y., Matsuoka, Y., Nishimoto, H., Masui, T., and Kainuma, M.: Global GHG emissions scenarios under GHG concentration stabilization targets., *J. Glob. Environ. Eng.*, 13, 97–108, 2008.
- Huybers, P. and Curry, W.: Links between annual, Milankovitch and continuum temperature variability, *Nature*, 441, 329–332, 2005.



- IPCC: Climate Change 2013: The Physical Science Basis. Contribution of Working Group I to the Fifth Assessment Report of the Intergovernmental Panel on Climate Change, Cambridge University Press, Cambridge, United Kingdom and New York, NY, USA, 2013a.
- IPCC: Summary for Policymakers, book section SPM, p. 1–30, Cambridge University Press, Cambridge, United Kingdom and New York, NY, USA, 2013b.
- Iversen, T., Bentsen, M., Bethke, I., Debernard, J. B., Kirkevåg, A., Seland, Ø., Drange, H., Kristjansson, J. E., Medhaug, I., Sand, M., and Seierstad, I. A.: The Norwegian Earth System Model, NorESM1-M –Part 2: Climate response and scenario projections, *Geosci. Model Dev.*, 6, 389–415, 2013.
- Jeffrey, S. J., Rotstayn, L. D., Collier, M. A., Dravitzki, S. M., Hamalainen, C., Moeseneder, C., Wong, K. K., and Syktus, J.: Australia's CMIP5 submission using the CSIRO-Mk3.6 model, *Aust. Meteorol. Ocean.*, 63, 1–13, 2013.
- Jones, P., Lister, D., Osborn, T., Harpham, C., and Salmon, M., M. C.: Hemispheric and large-scale land-surface air temperature variations: An extensive revision and an update to 2010, *J. Geophys. Res.*, 117, D05 127, 2012.
- Kennedy, J., N.A., R., Smith, R., Parker, D., and Saunby, M.: Reassessing biases and other uncertainties in sea surfacetemperature observations measured in situ since 1850:2. Biases and homogenization, *J. Geophys. Res.*, 116, D14 104, 2011.
- Köhler, P., Stap, L. B., von der Heydt, A. S., de Boer, B., van de Wal, R. S. W., and Bloch-Johnson, J.: A State-Dependent Quantification of Climate Sensitivity Based on Paleodata of the Last 2.1 Million Years, *Paleoceanography*, 32, 1102–1114, 2017.
- Lovejoy, S. and Schertzer, D.: *The Weather and Climate: Emergent Laws and Multifractal Cascades*, Cambridge University Press, 2013.
- Martin, G. M., Bellouin, N., Collins, W. J., Culverwell, I. D., Halloran, P. R., Hardiman, S. C., Hinton, T. J., Jones, C. D., McDonald, R. E., McLaren, A. J., O'Connor, F. M., Roberts, M. J., Rodriguez, J. M., Woodward, S., Best, M. J., Brooks, M. E., Brown, A. R., Butchart, N., Dearden, C., Derbyshire, S. H., Dharssi, I., Doutriaux-Boucher, M., Edwards, J. M., Falloon, P. D., Gedney, N., Gray, L. J., Hewitt, H. T., Hobson, M., Huddleston, M. R., Hughes, J., Ineson, S., Ingram, W. J., James, P. M., Johns, T. C., Johnson, C. E., Jones, A., Jones, C. P., Joshi, M. M., Keen, A. B., Liddicoat, S., Lock, A. P., Maidens, A. V., Manners, J. C., Milton, S. F., Rae, J. G. L., Ridley, J. K., Sellar, A., Senior, C. A., Totterdell, I. J., Verhoef, A., Vidale, P. L., and Wiltshire, A.: The HadGEM2 family of Met Office Unified Model climate configurations, *Geosci. Model Dev.*, 4, 723–757, 2011.
- Martins, T. G., Simpson, D., Lindgren, F., and Rue, H.: Bayesian computing with INLA: New features, *Comput. Stat. Data Anal.*, 67, 68–83, 2013.
- Morice, C., Kennedy, J., Rayner, N., and Jones, P.: Quantifying uncertainties in global and regional temperature change using an ensemble of observational estimates: The Hadcrut4 data set, *J. Geophys. Res.*, 117, D08 101, 2012.
- Qu, X., Hall, A., and DeAngelis, A. M.: On the Emergent Constraints of Climate Sensitivity, *J. Climate*, 31, 863–875, 2018.
- Riahi, K., Grübler, A., and Nakicenovic, N.: Scenarios of long-term socio-economic and environmental development under climate stabilization, *Technol Forecast Soc Change*, 74, 887–935, *greenhouse Gases - Integrated Assessment*, 2007.
- Robert, C. and Casella, G.: *Monte Carlo Statistical Methods*, Springer-Verlag New York, 1 edn., 1999.
- Rotstayn, L. D., Jeffrey, S. J., Collier, M. A., Dravitzki, S. M., Hirst, A. C., Syktus, J. I., and Wong, K. K.: Aerosol- and greenhouse gas-induced changes in summer rainfall and circulation in the Australasian region: a study using single-forcing climate simulations, *Atmospheric Chemistry and Physics*, 12, 6377–6404, 2012.
- Rue, H. and Held, L.: *Gaussian Markov Random Fields: Theory And Applications (Monographs on Statistics and Applied Probability)*, London: Chapman and Hall-CRC Press, 2005.
- Rue, H., Martino, S., and Chopin, N.: Approximate Bayesian inference for latent Gaussian models using integrated nested Laplace approximations (with discussion), *J R Stat Soc Series B*, 71, 319–392, 2009.



- Rue, H., Riebler, A., Sørbye, S. H., Illian, J. B., Simpson, D. P., and Lindgren, F. K.: Bayesian Computing with INLA: A Review, *Annu. Rev. Stat. Appl.*, 4, 395–421, 2017.
- Rybski, D., Bunde, A., Havlin, S., and von Storch, H.: Long-term persistence in climate and the detection problem, *Geophys. Res. Lett.*, 33, L06718–L06718, 2006.
- 425 Rypdal, K.: Global temperature response to radiative forcing: Solar cycle versus volcanic eruptions, *J. Geophys. Res.*, 117, D06115, 2012.
- Rypdal, K., Rypdal, M., and Fredriksen, H.-B.: Spatiotemporal long-range persistence in earth’s temperature field: Analysis of stochastic-diffusive energy balance models, *J. Climate*, 28, 8379–8395, 2015.
- Rypdal, M. and Rypdal, K.: Long-Memory Effects in Linear Response Models of Earth’s Temperature and Implications for Future Global
430 Warming, *J. Climate*, 27, 5240–5258, 2014.
- Rypdal, M. and Rypdal, K.: Late Quaternary temperature variability described as abrupt transitions on a $1/f$ noise background, *Earth Syst. Dynam.*, 7, 281–293, 2016.
- Rypdal, M., Fredriksen, H.-B., Myrsvoll-Nilsen, E., Rypdal, K., and Sørbye, S. H.: Emergent Scale Invariance and Climate Sensitivity, *Climate*, 6, 2018a.
- 435 Rypdal, M., Fredriksen, H.-B., Rypdal, K., and Steene, R. J.: Emergent constraints on climate sensitivity, *Nature*, 563, E4–E5, 2018b.
- Simpson, D., Rue, H., Riebler, A., Martins, T. G., and Sørbye, S. H.: Penalising Model Component Complexity: A Principled, Practical Approach to Constructing Priors, *Stat. Sci.*, 32, 1–28, 2017.
- Smith, S. J. and Wigley, T.: Multi-Gas Forcing Stabilization with Minicam, *Energy J.*, 27, 373–391, 2006.
- Sørbye, S. and Rue, H.: Fractional Gaussian noise: Prior specification and model comparison, *Environmetrics*, 29, 2018.
- 440 Sørbye, S. H., Myrsvoll-Nilsen, E., and Rue, H.: An approximate fractional Gaussian noise model with $\mathcal{O}(n)$ computational cost, *Stat. Comput.*, 29, 821–833, 2019.
- Tierney, L. and Kadane, J. B.: Accurate Approximations for Posterior Moments and Marginal Densities, *J. Am. Stat. Assoc.*, 81, 82–86, 1986.
- van Vuuren, D. P., den Elzen, M. G. J., Lucas, P. L., Eickhout, B., Strengers, B. J., van Ruijven, B., Wonink, S., and van Houdt, R.: Stabilizing
445 greenhouse gas concentrations at low levels: an assessment of reduction strategies and costs, *Clim. Change*, 81, 119–159, 2007.
- Voltaire, A., Sanchez-Gomez, E., Salas y Méliá, D., Decharme, B., Cassou, C., Sénési, S., Valcke, S., Beau, I., Alias, A., Chevallier, M., Déqué, M., Deshayes, J., Douville, H., Fernandez, E., Madec, G., Maïsonnave, E., Moine, M.-P., Planton, S., Saint-Martin, D., Szopa, S., Tyteca, S., Alkama, R., Belamari, S., Braun, A., Coquart, L., and Chauvin, F.: The CNRM-CM5.1 global climate model: description and basic evaluation, *Clim. Dynam.*, 40, 2091–2121, 2013.
- 450 Volodin, E. M., Dianskii, N. A., and Gusev, A. V.: Simulating present-day climate with the INMCM4.0 coupled model of the atmospheric and oceanic general circulations, *Izv., Atmos. Ocean Physics*, 46, 414–431, 2010.
- von der Heydt, A. S. and Ashwin, P.: State dependence of climate sensitivity: attractor constraints and palaeoclimate regimes, *Dyn. Stat. Clim. Syst.*, 1, 1–21, 2017.
- Watanabe, M., Suzuki, T., Oishi, R., Komuro, Y., Watanabe, S., Emori, S., Takemura, T., Chikira, M., Ogura, T., Sekiguchi, M., Takata,
455 K., Yamazaki, D., Yokohata, T., Nozawa, T., Hasumi, H., Tatebe, H., and Kimoto, M.: Improved Climate Simulation by MIROC5: Mean States, Variability, and Climate Sensitivity, *J. Climate*, 23, 6312–6335, 2010.
- Watanabe, S., Hajima, T., Sudo, K., Nagashima, T., Takemura, T., Okajima, H., Nozawa, T., Kawase, H., Abe, M., Yokohata, T., Ise, T., Sato, H., Kato, E., Takata, K., Emori, S., and Kawamiya, M.: MIROC-ESM 2010: model description and basic results of CMIP5-20c3m experiments, *Geosci. Model Dev.*, 4, 845–872, 2011.



- 460 Wise, M., Calvin, K., Thomson, A., Clarke, L., Bond-Lamberty, B., Sands, R., Smith, S. J., Janetos, A., and Edmonds, J.: Implications of Limiting CO₂ Concentrations for Land Use and Energy, *Science*, 324, 1183–1186, 2009.
- Wu, T., Song, L., Li, W., Wang, Z., Zhang, H., Xin, X., Zhang, Y., Zhang, L., Li, J., Wu, F., Liu, Y., Zhang, F., Shi, X., Chu, M., Zhang, J., Fang, Y., Wang, F., Lu, Y., Liu, X., Wei, M., Liu, Q., Zhou, W., Dong, M., Zhao, Q., Ji, J., Li, L., and Zhou, M.: An overview of BCC climate system model development and application for climate change studies, *J. Meteorolog. Res.*, 28, 34–56, 2014.
- 465 Yukimoto, S., Adachi, Y., Hosaka, M., Sakami, T., Yoshimura, H., Hirabara, M., Tanaka, T. Y., Shindo, E., Tsujino, H., Deushi, M., Mizuta, R., Yabu, S., Obata, A., Nakano, H., Koshiro, T., Ose, T., and Kitoh, A.: A New Global Climate Model of the Meteorological Research Institute: MRI-CGCM3 –Model Description and Basic Performance–, *J. Meteorolog. Soc. Jpn. Ser. II*, 90A, 23–64, 2012.



Response	bias	rmse	correlation
Scale-invariant	0.09	0.28	0.85
Exponential	-0.18	0.31	0.78

Table 1. Bias, root mean square error and correlation obtained when comparing the marginal posterior mean estimates of the TCR with the TCR obtained directly from the ESMs. These are computed using both a scale-invariant and an exponential response function.



ID	Earth System Model	Reference(s)	Time interval	TCR (K)	$Q_{2\times\text{CO}_2}$ (W m^{-2})
1	GISS-E2-R	(Hansen et al., 2010)	[1850,2015]	1.5	3.8
2	HadGEM2-ES	(Collins et al., 2011; Martin et al., 2011)	[1860,2015]	2.5	2.9
3	IPSL-CM5A-LR	(Dufresne et al., 2013)	[1850,2015]	2.0	3.1
4	NorEMS1-M	(Bentsen et al., 2013; Iversen et al., 2013)	[1850,2015]	1.4	3.1
5	ACCESS1.0	(Bi et al., 2012)	[1850,2015]	2.0	3.0
6	MIROC-ESM	(Watanabe et al., 2011)	[1850,2015]	2.2	4.3
7	MIROC5	(Watanabe et al., 2010)	[1850,2015]	1.5	4.1
8	CanESM2	(Chylek et al., 2011)	[1850,2015]	2.4	3.8
9	CCSM4	(Gent et al., 2011)	[1850,2015]	1.8	3.6
10	CNRMCM5	(Voldoire et al., 2013)	[1850,2015]	2.1	3.7
11	GFDL-CM3	(Donner et al., 2011)	[1860,2015]	2.0	3.0
12	GFDL-ESM2G	(Dunne et al., 2012, 2013)	[1861,2015]	1.1	3.1
13	CSIRO-MK3-6-0	(Rotstayn et al., 2012; Jeffrey et al., 2013)	[1850,2015]	1.8	2.6
14	BCC_CSM 1.1	(Wu et al., 2014)	[1850,2015]	1.7	3.2
15	BCC_CSM 1.1(m)	(Wu et al., 2014)	[1850,2015]	2.1	3.6
16	GFDL-ESM2M	(Dunne et al., 2012, 2013)	[1860,2015]	1.3	3.4
17	INM-CM4	(Volodin et al., 2010)	[1850,2015]	1.3	3.0
18	MPI-ESM-LR	(Giorgetta et al., 2013)	[1850,2015]	2.0	4.1
19	MRI-CGCM3	(Yukimoto et al., 2012)	[1850,2015]	1.6	3.2

Table 2. The earth system models used in this paper. The table includes ID-number, references, time interval, TCR obtained directly from the ESM, and slope coefficient for the forcing corresponding to a CO₂-doubling.



ID	H	σ_ϵ (K)	σ_f (K)	F_0 (W m^{-2})	$T\hat{C}R$ (K)
1	0.605	0.054	0.062	-0.076	1.381
	(0.553,0.682)	(0.048,0.06)	(0.058,0.066)	(-0.117,-0.034)	(1.309,1.463)
2	0.977	0.355	0.08	0.085	2.4
	(0.948,0.996)	(0.209,0.667)	(0.062,0.099)	(-0.068,0.234)	(1.853,2.964)
3	0.898	0.158	0.077	-0.024	2.118
	(0.829,0.955)	(0.121,0.211)	(0.065,0.089)	(-0.164,0.116)	(1.825,2.43)
4	0.838	0.122	0.059	0.06	1.457
	(0.758,0.912)	(0.1,0.15)	(0.047,0.071)	(-0.074,0.194)	(1.201,1.74)
5	0.899	0.129	0.076	0.086	2.026
	(0.835,0.954)	(0.1,0.172)	(0.063,0.089)	(-0.02,0.194)	(1.706,2.375)
6	0.867	0.124	0.077	0.177	2.798
	(0.794,0.933)	(0.1,0.158)	(0.066,0.089)	(0.056,0.295)	(2.408,3.215)
7	0.892	0.207	0.047	0.032	1.66
	(0.807,0.961)	(0.154,0.29)	(0.033,0.063)	(-0.167,0.232)	(1.2,2.192)
8	0.793	0.155	0.087	-0.003	2.473
	(0.708,0.879)	(0.131,0.183)	(0.073,0.101)	(-0.117,0.111)	(2.148,2.82)
9	0.74	0.122	0.07	0.006	1.769
	(0.652,0.831)	(0.106,0.141)	(0.06,0.082)	(-0.109,0.114)	(1.599,1.969)

Table 3. This table contains marginal posterior means and 95 % credible intervals for the model parameters and the transient climate response, obtained from fitting our model to temperature data from the first 9 ESMs.



ID	H	σ_ϵ (K)	σ_f (K)	F_0 (W m^{-2})	$T\hat{C}R$ (K)
10	0.797 (0.724,0.869)	0.123 (0.105,0.144)	0.08 (0.069,0.093)	0.098 (-0.009,0.204)	2.25 (1.907,2.626)
11	0.815 (0.733,0.892)	0.138 (0.115,0.166)	0.094 (0.081,0.108)	0.074 (-0.016,0.164)	2.197 (1.876,2.547)
12	0.876 (0.797,0.942)	0.16 (0.124,0.21)	0.052 (0.042,0.063)	0.119 (-0.06,0.294)	1.392 (1.099,1.71)
13	0.904 (0.836,0.963)	0.165 (0.125,0.229)	0.077 (0.061,0.094)	0.137 (0.001,0.267)	1.799 (1.423,2.209)
14	0.882 (0.857,0.906)	0.127 (0.112,0.142)	0.057 (0.051,0.066)	0.309 (0.102,0.457)	1.616 (1.448,1.868)
15	0.805 (0.71,0.87)	0.108 (0.083,0.13)	0.076 (0.07,0.083)	0.231 (0.076,0.434)	2.067 (1.8,2.314)
16	0.743 (0.655,0.832)	0.155 (0.134,0.179)	0.071 (0.058,0.086)	0.029 (-0.106,0.167)	1.69 (1.413,1.989)
17	0.914 (0.849,0.967)	0.121 (0.09,0.17)	0.03 (0.022,0.037)	0.085 (-0.121,0.292)	0.811 (0.638,1.003)
18	0.979 (0.973,0.985)	0.302 (0.259,0.365)	0.064 (0.054,0.074)	-0.135 (-0.324,0.056)	2.71 (2.274,3.125)
19	0.792 (0.707,0.873)	0.1 (0.084,0.118)	0.061 (0.049,0.074)	0.013 (-0.104,0.135)	1.457 (1.194,1.747)

Table 4. This table contains marginal posterior means and 95 % credible intervals for the model parameters and the transient climate response, obtained from fitting our model to temperature data from the last 10 ESMs.



	H	σ_e (K)	σ_f (W m^{-2})	F_0 (K)	$T\hat{C}R$ (K)
0	0.776 (0.704,0.858)	0.121 (0.106,0.137)	0.072 (0.057,0.085)	-0.096 (-0.215,0.038)	1.975 (1.559,2.353)
1	0.804 (0.725,0.882)	0.115 (0.098,0.137)	0.046 (0.037,0.055)	-0.012 (-0.172,0.148)	1.318 (1.115,1.541)
2	0.938 (0.886,0.979)	0.207 (0.147,0.31)	0.062 (0.047,0.079)	0.218 (0.047,0.382)	1.71 (1.291,2.19)
3	0.822 (0.744,0.895)	0.12 (0.1,0.144)	0.051 (0.042,0.062)	0.026 (-0.126,0.178)	1.243 (1.041,1.469)
4	0.859 (0.787,0.931)	0.133 (0.109,0.167)	0.058 (0.046,0.07)	0.124 (-0.024,0.27)	1.481 (1.22,1.789)
5	0.925 (0.868,0.972)	0.183 (0.135,0.263)	0.059 (0.045,0.074)	0.207 (0.04,0.369)	1.645 (1.271,2.06)
6	0.854 (0.778,0.92)	0.13 (0.105,0.162)	0.06 (0.048,0.073)	0.159 (0.011,0.304)	2.128 (1.754,2.565)
7	0.84 (0.766,0.91)	0.125 (0.104,0.153)	0.055 (0.045,0.066)	0.127 (-0.021,0.275)	1.806 (1.503,2.141)
8	0.843 (0.769,0.912)	0.127 (0.104,0.155)	0.049 (0.039,0.059)	0.084 (-0.08,0.246)	1.497 (1.241,1.783)
9	0.806 (0.728,0.889)	0.116 (0.099,0.138)	0.041 (0.033,0.049)	0.037 (-0.13,0.204)	1.118 (0.954,1.305)

Table 5. This table contains marginal posterior means and 95 % credible intervals for the model parameters and the transient climate response, obtained from fitting our model to the HadCRUT dataset using forcing data from Hansen et al. (2010) (denoted by ID 0) and from the first 9 ESMs.



	H	σ_e (K)	σ_f (W m^{-2})	F_0 (K)	$T\hat{C}R$ (K)
10	0.843 (0.768,0.913)	0.126 (0.104,0.155)	0.061 (0.05,0.074)	0.146 (0.006,0.283)	1.849 (1.535,2.215)
11	0.929 (0.871,0.975)	0.193 (0.139,0.283)	0.05 (0.038,0.063)	0.262 (0.07,0.439)	1.421 (1.086,1.789)
12	0.872 (0.801,0.938)	0.143 (0.114,0.184)	0.047 (0.037,0.057)	0.181 (0.003,0.357)	1.234 (0.998,1.492)
13	0.932 (0.878,0.975)	0.192 (0.139,0.28)	0.065 (0.05,0.082)	0.178 (0.019,0.334)	1.597 (1.223,2.016)
14	0.788 (0.707,0.869)	0.111 (0.095,0.131)	0.049 (0.04,0.058)	0.03 (-0.114,0.173)	1.159 (0.993,1.341)
15	0.934 (0.911,0.954)	0.193 (0.164,0.226)	0.039 (0.031,0.047)	-0.254 (-0.414,-0.048)	1.342 (1.065,1.622)
16	0.865 (0.792,0.932)	0.14 (0.112,0.177)	0.049 (0.038,0.06)	0.042 (-0.134,0.218)	1.384 (1.112,1.689)
17	0.847 (0.785,0.907)	0.122 (0.102,0.148)	0.051 (0.038,0.062)	-0.122 (-0.286,0.064)	1.179 (0.787,1.502)
18	0.933 (0.906,0.955)	0.192 (0.16,0.227)	0.038 (0.027,0.049)	-0.245 (-0.415,-0.029)	1.461 (1.042,1.891)
19	0.894 (0.83,0.951)	0.152 (0.12,0.201)	0.064 (0.049,0.08)	0.017 (-0.136,0.173)	1.795 (1.406,2.225)

Table 6. This table contains marginal posterior means and 95 % credible intervals for the model parameters and the transient climate response, obtained from fitting our model to the HadCRUT dataset using forcing data from the last 10 ESMs.


Paper III

Emergent Scale Invariance and Climate Sensitivity

Climate, **6**, 93, 2018.

Article

Emergent Scale Invariance and Climate Sensitivity

Martin Rypdal *, Hege-Beate Fredriksen, Eirik Myrsvoll-Nilsen, Kristoffer Rypdal and Sigrunn H. Sørbye 

Department of Mathematics and Statistics, UiT The Arctic University of Norway, 19019 Tromsø, Norway; hege-beate.fredriksen@uit.no (H.-B.F.); eirik.myrsvoll-nilsen@uit.no (E.M.-N.); kristoffer.rypdal@uit.no (K.R.); sigrunn.sorbye@uit.no (S.H.S.)

* Correspondence: martin.rypdal@uit.no; Tel.: +47-77-620-754

Received: 23 October 2018; Accepted: 25 November 2018; Published: 28 November 2018



Abstract: Earth’s global surface temperature shows variability on an extended range of temporal scales and satisfies an emergent scaling symmetry. Recent studies indicate that scale invariance is not only a feature of the observed temperature fluctuations, but an inherent property of the temperature response to radiative forcing, and a principle that links the fast and slow climate responses. It provides a bridge between the decadal- and centennial-scale fluctuations in the instrumental temperature record, and the millennial-scale equilibration following perturbations in the radiative balance. In particular, the emergent scale invariance makes it possible to infer equilibrium climate sensitivity (ECS) from the observed relation between radiative forcing and global temperature in the instrumental era. This is verified in ensembles of Earth system models (ESMs), where the inferred values of ECS correlate strongly to estimates from idealized model runs. For the range of forcing data explored in this paper, the method gives best estimates of ECS between 1.8 and 3.7 K, but statistical uncertainties in the best estimates themselves will provide a wider likely range of the ECS.

Keywords: climate sensitivity; scale invariance; long-range persistence; climate variability; emergent constrains

1. Introduction

The Intergovernmental Panel on Climate Change [1] (IPCC) has estimated the likely range of equilibrium climate sensitivity (ECS) to be between 1.5 and 4.5 K. The ECS, which is widely used in assessments of anthropogenic climate change, is defined as the asymptotic temperature increase following an instantaneous CO₂ doubling. In Earth system models (ESMs), the ECS is generally estimated via the so-called Gregory plots [2], where the response in the top-of-the-atmosphere radiation N is plotted against the global mean surface temperature (GMST) anomaly ΔT during the equilibration following an instantaneous doubling or quadrupling of the atmospheric CO₂ concentration. The assumption is that the adjustment in radiation depends linearly on the surface temperature increase,

$$N = F - \lambda \Delta T, \quad (1)$$

so that the feedback parameter λ and the forcing F can be determined via linear regression. The ECS is hence $F_{2 \times \text{CO}_2} / \lambda$, where $F_{2 \times \text{CO}_2}$ is the forcing associated with a CO₂ doubling. The Gregory plots show that the linearity assumption is only approximate, and in particular, there are slow feedbacks in the models that reduce the feedback parameter as the planet warms [3]. A state dependence is also observed in the so-called paleo sensitivity [4–7]. Nevertheless, the usefulness of ECS and its estimation still relies on the linearity assumption in Equation (1). Satellite observations of the top-of-the-atmosphere radiation are available through the Clouds and the Earth’s Radiant Energy

System (CERES), but unfortunately, the data only covers the years 2000-present. The state-of-the-art ECS estimates based on the satellite data gives a wide likely range (in this case a 17–83% confidence interval) of 2.4–4.5 K [8].

A different approach, which can be used when the top-of-the-atmosphere radiation is unknown, is to combine model results with the instrumental temperature record. Recently Cox et al. claimed that ECS can be constrained to a “likely range” (in this paper specified to be the 66% confidence interval) of 2.2 to 3.4 K, with a best estimate of 2.8 K [9]. They propose a metric ψ characterizing the correlation structure of the internal variability of the GMST in both the instrumental temperature record in the period 1880 to 2016 and in the corresponding historical runs in the Coupled Model Intercomparison Project Phases 5 (CMIP5) ensemble. By exploring a so-called emergent relationship between ECS and ψ , they estimate a distribution $P(\text{ECS}|\psi)$ for the Gregory estimate of ECS conditioned on ψ , and using the law of total probability in conjunction with Bayes Theorem, they obtain a probability density function $P(\text{ECS})$ constrained by the instrumental record. However, it has been demonstrated that their estimated metric depends on the response to the strong anthropogenic forcing in the time period after year 1950, and hence one has to take into account that the historical forcing times series used in different models in the ensemble are not exactly the same [10]. Another problem is that the emergent relationship was derived from an oversimplified one-box stochastic energy balance equation (Equation (7) described in Section 2.1). This model does not take into account the memory effects in the response due to heat exchange between the ocean mixed layer and the deep ocean. Models that do incorporate such memory effects are briefly reviewed in Sections 2.2 and 2.3.

A method of constraining ECS from the instrumental record that does not draw on a simplified physical model is to include data for historical forcing, with its uncertainties, and to estimate response functions that describe the relationship between global radiative forcing and the observed GMST. If one adopts a hypothesis of a linear and stationary response, then the temperature anomaly ΔT can be written as a convolution of the forcing F with a response function $G(t)$:

$$\Delta T(t) = \int_{-\infty}^t G(t-s) (F(s)ds + \sigma dB(s)), \quad (2)$$

where the term $F(t)$ is the known (deterministic) forcing and $dB(t)$ represents a white-noise random forcing that gives rise to the internal variability. Equation (2) only assumes linearity and stationarity of the response, and it is only the functional form of $G(t)$ that depends on the particular physical modeling of this response. As discussed in Section 2.2, such a linear response can be derived from a multi-layer energy balance model, where the response function is a sum of exponential functions with decay rates that are given by the real and negative eigenvalues of the system of differential equations. Fredriksen and Rypdal [11] have shown that three exponential terms are sufficient to obtain a model that simultaneously displays responses to historical and reconstructed forcing that are consistent with the instrumental temperature record and the reconstructed last millennium global mean temperature, respectively. In addition, it correctly describes the statistical properties of the internal variability on time scales from months to centuries [12]. The constructed response function corresponds to an ECS estimate of 3.0 K, obtained by using the forcing $F(t) = F_{2 \times \text{CO}_2} \Theta(t)$ in Equation (2), where $\Theta(t)$ is the unit step function. Defining the ECS as $\lim_{t \rightarrow \infty} \Delta T(t)$, Equation (2) yields

$$\text{ECS} = F_{2 \times \text{CO}_2} \int_0^{\infty} G(t) dt. \quad (3)$$

The forcing $F_{2 \times \text{CO}_2}$ is well approximated by a logarithmic dependence of the CO_2 concentration, with a best estimate of 3.7 W/m^2 found by the IPCC [1]. Uncertainties associated with the radiative transfer calculations are small [13]. However, forcing estimates from CMIP5 models often include rapid adjustments of the atmosphere, resulting in larger uncertainties [14]. The more serious issues are the uncertainty of the estimate of the response function, the uncertainty of the adjusted forcing data, and the validity of the linearity assumption.

The uncertainty of the response function estimates can be assessed in several ways, for instance using an ensemble of runs of the same experiment in one ESM. The uncertainty of the forcing presents a significant challenge, which is not addressed by Cox et al. [9]. In the present paper, we take part of this uncertainty into account by analyzing the spread of the adjusted forcing over the CMIP5 ensemble. We shall also consider the order of magnitude of uncertainty that can be attributed to our limited knowledge about the forcing from volcanic aerosols. In model runs with historical forcing, the adjusted forcing is obtained from Equation (1) by comparing the time series of $\Delta T(t)$ and the top-of-the-atmosphere radiation $N(t)$ for a fixed estimate of the feedback parameter λ [15]. The resulting time series $F(t)$ is an estimate of the forcing experienced by the ESM. However, the construction of $F(t)$ from the assumed linear relationship between $\Delta T(t)$ and $N(t)$ results in forcing signals where some short-scale internal climate variability, including the El Niño Southern Oscillation (ENSO), are clearly observable in the forcing signal. Consequently, these forcing data are not suitable for statistical estimation of response functions $G(t)$ from Equation (2). The alternative, which is used in this paper, is to fix a forcing time series, for instance the time series provided by Hansen et al. [16], and to modify it for each model so that the trend (or low-frequency variability) is equal to the adjusted forcing for the model. This approach serves two purposes; we ensure that when we fit a response function to a model the increasing trend in the forcing is consistent with the forcing in the model run, and it provides an ensemble of forcing time series with different trends. The estimates of the response function from the observed temperature record can be repeated across this ensemble of forcing time series and provide an estimate of the uncertainty in the response function that is associated with the uncertainty in the forcing trend.

If one derives the response function from a multibox energy balance model it will take the form (see Section 2.2),

$$G(t) = \sum_{k=1}^N c_k e^{-t/\tau_k}. \quad (4)$$

In Section 3 it is described how to obtain statistical estimates \hat{c}_k and $\hat{\tau}_k$ of the parameters c_k and τ_k from historical runs of each of the ESMs in the CMIP5 ensemble, as well as for the instrumental temperature record. For each model, this estimate corresponds to an estimate of ECS through Equation (3), which in this case reads

$$\widehat{\text{ECS}} = F_{2 \times \text{CO}_2} \sum_{k=1}^N \hat{c}_k \hat{\tau}_k.$$

If the estimate $\widehat{\text{ECS}}$ correlates strongly with the Gregory estimate of ECS over the CMIP5 ensemble, then the estimate $\widehat{\text{ECS}}$ obtained from the instrumental temperature record can be used to constrain the distribution of ECS in the ensemble. Unfortunately, such an analysis will show a very weak correlation between the two estimates, and this apparently indicates that response function estimates are useless for constraining ECS. On the other hand, the reason for the low correlation is that the instrumental temperature record is too short to provide useful information about the slow response of the climate system, and the general form of the response function leads to statistical over-fitting. The method can be improved by reducing the number of free parameters. A naïve approach is to reduce the response function to one characteristic time scale (which is what comes out of using the one-box model employed by Cox et al. [9]). This gives a model that is unable to accurately describe the temporal structure of the temperature response, and would lead to a systematic underestimation of the ECS. A better alternative is to use the emergent property of temporal scale invariance.

Rypdal and Rypdal [12] have demonstrated that a scale-invariant response model, i.e., Equation (2) with

$$G(t) = \left(\frac{t}{\mu}\right)^{\beta/2-1} \Theta(t) \xi, \quad (5)$$

where $\xi = 1 \text{ km}^2 \text{ J}^{-1}$ is a factor needed to give $G(t)$ the right physical dimension, provides a parsimonious and accurate model on time scales from months to several centuries, although not on longer time scales. In fact, it will be argued in Section 4 that the power-law dependence (at least in the models) is invalid on time scales substantially longer than a millennium. The existence of a cut-off in this dependence on very long time scales is obvious, since the ECS according to Equation (3) would be infinite otherwise [12]. We don't have to worry about this cut-off when we estimate the model parameters from historical data since the temperature records and the forcing time series we have for the industrial period are relatively short compared to this cut-off time, which corresponds to the time it takes for global surface temperature to relax to a new equilibrium after an abrupt CO_2 doubling in ESMs. This large separation of the two time scales (observation time and relaxation time) is also the main reason why it is so difficult to provide accurate estimates of ECS from observational data. The fact that a response model with infinite ECS can perform well when tested on observation data suggests that these time series are too short for ECS assessment and that ECS may not be the most useful measure of climate sensitivity in the face of anthropogenic climate change. It may be more useful to study the scale-dependent (or frequency-dependent) sensitivity;

$$R(f) = F_{2 \times \text{CO}_2} |\tilde{G}(f)|, \quad (6)$$

where

$$\tilde{G}(f) = \int_{-\infty}^{\infty} G(t) e^{-2\pi i f t} dt$$

is the Fourier transform of the response function. However, as the main results of this paper will show, the scale dependent sensitivity evaluated at $f = 10^{-3} \text{ y}^{-1}$ correlates strongly with the Gregory estimate of ECS. Hence, this technique can be used to constrain the ECS in the model ensemble on the instrumental temperature record. It is evident from the results presented in this paper that uncertainty in the historical forcing data is the main obstacle for more accurate assessment of ECS.

The paper is structured as follows. In Section 2 we discuss stochastic linear response models for global surface temperature variability to motivate the analyses presented in Section 4. We also discuss some dissipation-response relations that follow from this modeling framework. Details on data employed and the statistical analyses are presented in Section 3. In Section 4 we present the main results, and in Section 5 we discuss and conclude our findings.

2. Linear Response Models and Scale-Dependent Sensitivity

2.1. The 1-Box Energy Balance Model

The simplest climate model, the so-called 1-box energy balance model, describes the temperature anomaly ΔT via the first order differential equation

$$Cd\Delta T(t) = -\lambda\Delta T dt + F(t)dt, \quad (7)$$

where C is a heat capacity, λ is the feedback parameter and $F(t)$ is the radiative forcing. If one includes a white-noise stochastic forcing, the model becomes a stochastic differential equation on the form

$$Cd\Delta T(t) = -\lambda\Delta T dt + F(t)dt + \sigma dB(t), \quad (8)$$

where $dB(t)$ is the white-noise random measure. The solution of the equation is

$$\Delta T(t) = \frac{1}{C} \int_{-\infty}^t e^{-(t-s)/\tau} F(s) ds + \frac{\sigma}{C} \int_{-\infty}^t e^{-(t-s)/\tau} dB(s), \quad (9)$$

where the characteristic time scale is $\tau = C/\lambda$. The second term in the above expression defines the Ornstein-Uhlenbeck process

$$X(t) = \frac{\sigma}{C} \int_{-\infty}^t e^{-(t-s)/\tau} dB(s),$$

i.e., the continuous-time version of an AR(1) process, sometimes referred to as red noise. This is a Gaussian process characterized by its exponentially decaying correlation function. In fact, the covariance structure of the process is given by the expression

$$r_X(\Delta t) = \langle X(t)X(t + \Delta t) \rangle = \frac{\sigma^2\tau}{2C^2} e^{-|\Delta t|/\tau},$$

and from the Wiener-Kinchin theorem it follows that the power-spectral density (PSD) of $X(t)$ is Lorentzian

$$S_X(f) = \int_{-\infty}^{\infty} r_X(t)e^{-2\pi ift} dt = \frac{1}{C^2} \frac{\sigma^2\tau^2}{1 + 4\pi^2\tau^2 f^2}.$$

The PSD scales as $S(f) \sim f^{-2}$ for frequencies $f \gg 1/\tau$, and as $S(f) \approx \sigma^2\tau^2/C^2$ for $f \ll 1/\tau$.

The first term in Equation (9) can be referred to as the response to the deterministic (or known) forcing, and denoted $\Delta T_{\text{det}}(t)$. If the forcing is an instantaneous CO₂ doubling at time $t = 0$ we can write $F(t) = F_{2 \times \text{CO}_2} \Theta(t)$, where $F_{2 \times \text{CO}_2}$ is the forcing corresponding to the CO₂ doubling, and $\Theta(t)$ is the unit-step function. The response is

$$\Delta T_{\text{det}}(t) = \frac{F_{2 \times \text{CO}_2}}{C} \int_0^t e^{-(t-s)/\tau} ds = \frac{F_{2 \times \text{CO}_2}\tau}{C} (1 - e^{-t/\tau}).$$

In particular an expression for the ECS is obtained in the limit $t \rightarrow \infty$:

$$\text{ECS} = \frac{F_{2 \times \text{CO}_2}\tau}{C} = \frac{F_{2 \times \text{CO}_2}}{\lambda}.$$

We note that there are connections between the response to deterministic forcing and the statistical properties of the random fluctuations $X(t)$. For instance, the low-frequency limit of the PSD is proportional to the square of the ECS:

$$\lim_{f \rightarrow 0} S_X(f) = \int_{-\infty}^{\infty} r_X(t) dt = \frac{\sigma^2\tau^2}{C^2} = \frac{\sigma^2}{\lambda^2} = \frac{\sigma^2}{F_{2 \times \text{CO}_2}^2} \text{ECS}^2.$$

The above expression is an example of a dissipation-response relation that holds for more general linear response models.

2.2. Generalizations of the 1-Box Model

The 1-box energy-balance model describes temperature response through a single characteristic time scale, and does not accurately take into account the warming of the deep oceans, which is much slower than the thermal response of the atmosphere. A more accurate energy-balance model is the so-called 2-box model, for which the analog of Equation (8) is

$$\begin{aligned} C_1 d\Delta T_1(t) &= -\lambda\Delta T_1 dt + \kappa(\Delta T_2 - \Delta T_1) dt + F(t) dt + \sigma dB(t) \\ C_2 d\Delta T_2(t) &= -\kappa(\Delta T_2 - \Delta T_1) dt. \end{aligned}$$

For $\kappa > 0$, this system has two negative eigenvalues $-1/\tau_1$ and $-1/\tau_2$, and the surface temperature anomaly $\Delta T = \Delta T_1$ can be written as Equation (2), where $G(t) = (c_1 e^{-t/\tau_1} + c_2 e^{-t/\tau_2}) \Theta(t)$ now is a response function with two characteristic time scales. The model can be further generalized to the class of N -box models for which we have a response function given by Equation (4), or to an even more general class of models for which we just assume that there is some response function $G(t)$ with

$G(t) = 0$ for $t < 0$. In the general case we find, by using the definition $X(t) = \sigma \int_0^t G(t-s) dB(s)$ of the noise-driven response process and the relation $\langle dB(s) dB(s') \rangle \propto \delta(s-s')$ for the white noise process, that

$$r_X(\Delta t) = \langle X(t)X(t+\Delta t) \rangle = \sigma^2 \int_0^\infty G(t)G(t+\Delta t)dt$$

for $\Delta t > 0$. The angle brackets here denote the expectation value. From Equation (3), we then have

$$\text{ECS}^2 = F_{2\times\text{CO}_2}^2 \int_0^\infty \int_0^\infty G(t)G(s)dt ds = \frac{F_{2\times\text{CO}_2}^2}{\sigma^2} \int_{-\infty}^\infty r_X(\Delta t)d\Delta t = \frac{F_{2\times\text{CO}_2}^2}{\sigma^2} \lim_{f \rightarrow 0} S_X(f). \quad (10)$$

We now define the scale-dependent climate sensitivity as

$$R(f) = \frac{F_{2\times\text{CO}_2}}{\sigma} S_X(f)^{1/2}. \quad (11)$$

It appears immediately from Equation (10) that $R(f \rightarrow \infty) = \text{ECS}$, so from a theoretical viewpoint, this definition makes sense. For computational purposes, however, the definition presented in Equation (6) is more practical. From the definitions of $S_X(f)$, $r_X(t)$, and $X(t)$ it is easy to demonstrate that

$$S_X(f) = \sigma^2 |G(f)|^2, \quad (12)$$

hence the two definitions are equivalent.

2.3. Scale-Invariant Models

The statistical properties of global surface temperature are consistent with those of long-range dependent (LRD) stochastic properties [17–22], in particular with fractional Gaussian noise (fGn). This can be modeled by letting the response function $G(t)$ take the form of Equation (5). In fact, the stochastic component

$$X(t) = \int_{-\infty}^t \left(\frac{t-s}{\mu} \right)^{\beta/2-1} \zeta dB(s)$$

can be taken as a formal definition of a fGn (see the Appendix of [12]). Its PSD is $S(f) \sim f^{-\beta}$. Studies also indicate that scale invariance is not only a feature of the observed temperature fluctuations, but an inherent property of the temperature response to radiative forcing [11,12,22–24]. This means that the deterministic component

$$\Delta T_{\text{det}}(t) = \int_{-\infty}^t \left(\frac{t-s}{\mu} \right)^{\beta/2-1} F(s) \zeta ds$$

is an accurate description of the temperature response to the known deterministic forcing. Moreover, the stochastic and deterministic responses can simultaneously describe the deterministic temperature response and the climate noise (residual), meaning that the parameters β and μ can take the same values in the two terms. This is a type of dissipation-fluctuation result, but not as strong as those that directly link the statistical properties of the climate noise to the characteristics of the response. More important; it provides a statistical model for which parameter estimates are very stable, and this makes these models suitable for extracting proxies of ECS from historical runs in the model ensemble.

3. Materials and Methods

3.1. Data

The instrumental temperature record used in this paper is the HadCRUT4 observational dataset which was downloaded from <https://crudata.uea.ac.uk/cru/data/temperature/>. The CMIP5 ESM data was downloaded from <https://esgf-data.dkrz.de/search/cmip5-dkrz/>. Forcing data was

retrieved from the sources provided in [15,16]. The time period 1850-2016 is used for all historical runs and for the instrumental temperature record.

3.2. Parameter Estimation

In discrete time, the statistical model given by Equations (2) and (5) can be written as

$$\Delta \mathbf{T} = \sigma_f G(\beta) (F_0 + \mathbf{F}) + \boldsymbol{\epsilon}(\sigma, \beta), \quad (13)$$

where we have defined a matrix

$$G_{t,s}(\beta) = \begin{cases} (t-s+\frac{1}{2})^{\beta/2-1}, & 1 \leq s \leq t \\ 0, & \text{otherwise} \end{cases}.$$

Here $\Delta \mathbf{T} = (\Delta T(t_1), \Delta T(t_2), \dots, \Delta T(t_n))^T$ is the time series for global surface temperature, $\mathbf{F} = (F(t_1), F(t_2), \dots, F(t_n))^T$ is the time series for the known forcing, and $\boldsymbol{\epsilon} = \boldsymbol{\epsilon}(\sigma, \beta) = (\epsilon(t_1), \epsilon(t_2), \dots, \epsilon(t_n))^T$, where ϵ is a fGn with parameters β and σ . In this paper we only consider time series that are sampled yearly, so we let $t_i = i$, and omit the time unit for simplicity. The random vector $\boldsymbol{\epsilon}$ is a segment of a fGn, so by definition it is a stationary zero-mean Gaussian vector with covariance matrix

$$\Sigma_{i,j} = \frac{\sigma^2}{2} (|i-j+1|^{\beta+1} + |i-j-1|^{\beta+1} - 2|i-j|^{\beta+1}).$$

The parameter β is related to the Hurst exponent H through the relation $\beta = 2H - 1$ [25].

In fitting Equation (13) to a given temperature series, the parameters β , σ_f , σ and F_0 are found numerically using the methodology of integrated nested Laplace approximation (INLA) [26]. In addition, the parameter μ is determined using the formula $(1/\mu)^{\beta/2-1} = \sigma_f$. INLA is available within the programming environment R, using the open-source package R-INLA which can be downloaded from www.r-inla.org. It represents a computationally efficient Bayesian approach which gives accurate estimates of the posterior marginals for all the parameters in Equation (13), potentially also including the predictor itself.

Specifically, INLA is designed to provide inference for a flexible class of three-stage hierarchical models, referred to as latent Gaussian models [26]. The first stage specifies that the observations ($\Delta \mathbf{T}$) are assumed conditionally independent given a latent field and hyperparameters. The second stage assumes that the latent field ($E(\Delta \mathbf{T})^T, \boldsymbol{\epsilon}^T$) given additional hyperparameters is a zero-mean Gaussian Markov random field. This assumption implies that the precision (inverse covariance) matrix of the latent field will be sparse. The third stage specifies a prior for each of the hyperparameters ($\beta, \sigma, \sigma_f, F_0$).

The model defined by Equation (13) does not fit into the class of latent Gaussian models without modifications. First, the LRD properties of the fGn process make the precision matrix of the latent field dense. To ensure computational efficiency, this is circumvented by approximating the fGn as a weighted sum of four AR(1) processes as introduced in [27]. Second, the mean of the observation vector, $E(\Delta \mathbf{T}) = \sigma_f G(\beta) (F_0 + \mathbf{F})$ has a non-standard form. This requires separate specification as described in [28], also providing implementation of the model using the freely available R package INLA.climate.

4. Results

For each ESM in the CMIP5 ensemble we modify the forcing data of Hansen et al. [16] such that its 17-year moving average becomes identical to the the moving average of adjusted forcing provided by Forster et al. [15] for that model. This is done by adding the difference between the moving average of the adjusted model forcing and the Hansen forcing to the raw Hansen forcing time series. The idea is to construct forcing time series for each model that retain a common structure on time scales that resolve volcanic forcing, the solar cycle and ENSO variability, but exhibit the overall trend on multi-decadal

time scales of the forcing time series used in the respective models. A 17-year moving average window is found to be the optimum choice to achieve that goal. For the model given by Equation (2) with response function given by Equation (5) we fit parameters β and μ to the global surface temperature of the historical run of the given ESM, using the modified Hansen forcing as input. The parameters are estimated using a technique described in Section 3. Figure 1a shows the adjusted forcing and the modified Hansen forcing for the NorESM1-M model, and Figure 1b shows the response to the modified Hansen forcing according to the fitted linear response model together with the global surface temperature in the historical run of the NorESM1-M model.

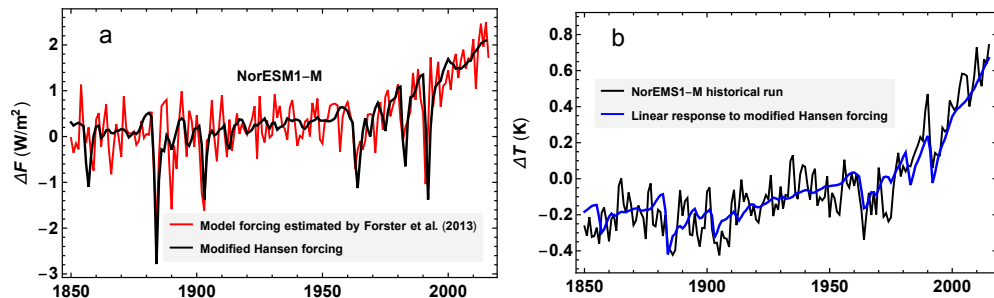


Figure 1. (a) The red curve is the adjusted forcing for the NorESM1-M model provided by Forster et al. [15]. The black curve is the forcing data of Hansen et al. [16] modified so that its 17-year moving average equals the 17-year moving average of the red curve. (b) The black curve is the global surface temperature in the historical run of the NorESM1-M model, and the blue curve is the response to the modified Hansen forcing (the black curve in (a)) for the model given by Equation (5). Parameters are estimated as $\beta = 0.67$ and $\mu = 7.8 \times 10^{-3} \text{ y}^{-1}$.

When parameters β and μ are estimated for the historical runs of each ESM, the estimated scale dependent sensitivity $R(f)$ can be computed for each model using Equation (6). The factor $F_{2 \times \text{CO}_2}$ is taken individually for each model based on the Gregory estimates in [1]. A scalar metric R is obtained by evaluating the functions $R(f)$ at the frequency $f = 10^{-3} \text{ y}^{-1}$. The results are presented in Table 1. The choice of frequency is based on how well the corresponding scalar metric correlates with the Gregory estimates of ECS. The scale-dependent sensitivities are computed from Equation (6) under the assumption that the response function is scaling and given by Equation (5). Hence the $R(f)$ -curves are power-laws and displayed as the straight, sloping lines in the double-logarithmic plot in Figure 2a. The figure shows that over the model ensemble, $R(f)$ typically equals the Gregory estimate of ECS for frequencies $f \approx 10^{-3} \text{ y}^{-1}$, and Figure 2b shows that the correlation (over the model ensemble) between $R(f)$ and the Gregory estimate of ECS has its maximum for $f \approx 10^{-3} \text{ y}^{-1}$. The falling correlation for lower f suggests that the power-law assumption for $R(f)$ fails for time scales much longer than a millennium.

Figure 3a shows a plot of the R , i.e., $R(f)$ evaluated at $f = 10^{-3} \text{ y}^{-1}$, versus the Gregory estimate of ECS. The points (letters) represent the different ESMs in the model ensemble, and the contour plot shows the conditional probability density function (PDF) $p(\text{ECS}|R)$ estimated from the seventeen data points corresponding to the seventeen ESMs in the ensemble. The method used to estimate $p(\text{ECS}|R)$ is the same as prescribed by Cox et al. (2018) [9], with the obvious weakness that it is based on the assumption that the deviation among the models from an emergent linear relationship $\text{ECS} = aR + b$ between ECS and R has a Gaussian distribution.

Table 1. Estimated quantities for the Earth system model (ESM) in the ensemble. The columns for equilibrium climate sensitivity (ECS) and $F_{2\times\text{CO}_2}$ are obtained from Gregory plots for $4 \times \text{CO}_2$ runs and taken from [1]. The columns denoted β , μ and σ show the estimates of the parameters in the model given by Equation (2) with response function given by Equation (5), obtained from historical runs of the ESMs and the modified Hansen forcing for each model. The last column displays the scale-dependent sensitivity $R(f)$ obtained from Equation (6) using the values of $F_{2\times\text{CO}_2}$, β and μ that are listed in the columns to the left, and evaluated at $f = 10^{-3} \text{ y}^{-1}$.

Model	ECS (K)	$F_{2\times\text{CO}_2}$ (W/m ²)	β	μ (10 ⁻³ y)	σ (W/m ²)	R (K) *
GISS-E2-R	2.1	3.8	0.49	13.8	0.07	3.3
HadGEM2-ES	4.6	2.9	0.95	7.3	0.32	4.8
IPSL-CM5A-LR	2.6	3.1	0.79	9.6	0.16	4.0
NorESM1-M	2.8	3.1	0.67	7.8	0.12	2.7
Access1-0	3.8	3.0	0.68	7.3	0.10	2.6
Miroc-ESM	4.7	4.3	0.73	6.6	0.12	3.9
Miroc5	2.7	4.1	0.78	4.0	0.21	3.2
CanESM2	3.7	4.1	0.59	17.5	0.15	4.8
CCSM4	2.9	3.8	0.49	14.9	0.12	3.5
CNRM-CM5	3.3	3.6	0.60	15.0	0.12	3.9
GFDL-CM3	4.0	3.0	0.62	19.0	0.14	4.0
GFDL-ESM2G	2.4	3.1	0.72	5.8	0.15	2.5
CSIRO-MK3	4.1	2.6	0.82	8.9	0.17	3.4
BCC-CSM1-1M	2.8	3.2	0.53	15.8	0.09	3.2
GFDL-ESM2m	2.4	3.1	0.47	15.3	0.16	2.8
INM-CM4	2.1	3.0	0.82	1.6	0.12	1.6
MPI-ESM-LR	3.6	4.1	0.78	7.6	0.16	4.5
MRI-CGCM3	2.6	3.2	0.58	9.9	0.10	2.6

* In the last column $R = R(f)$ for $f = 10^{-3} \text{ y}^{-1}$.

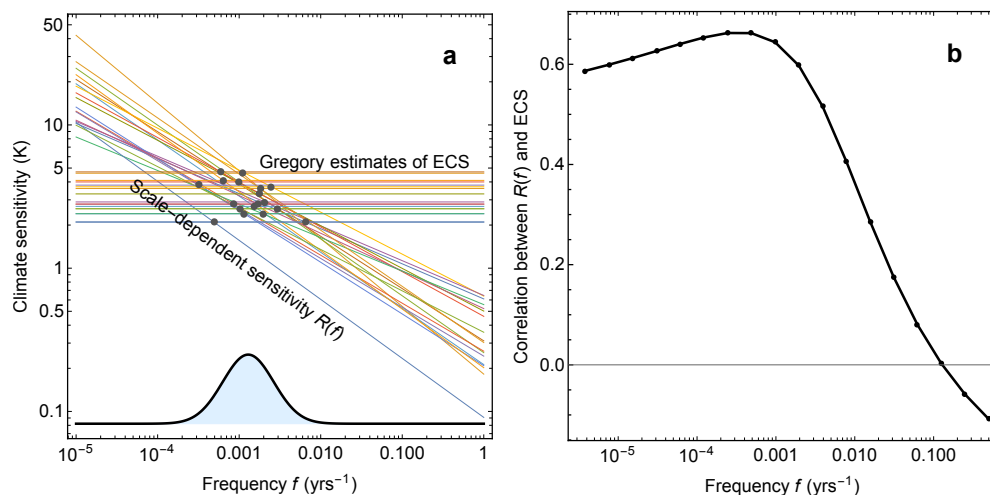


Figure 2. (a) The sloping lines are double-logarithmic plots of the scale dependent sensitivity $R(f)$ for each ESM in the ensemble. The different slopes correspond to different β -estimates. The horizontal lines indicate the ECS of the ESMs obtained from the Gregory plots and reported in [1], and the black dots indicate for which frequency f we have $R(f) = \text{ECS}$ for each model. (b) Correlation (over the ensemble of ESMs) between the scale-dependent sensitivity $R(f)$ and the Gregory estimate of the ECS. The correlation coefficient is plotted as a function of the frequency f .

The vertical black line in Figure 3a is $R = 2.9$ K. This value of R is obtained from the parameters $\beta = 0.66$ and $\mu = 11.9 \times 10^{-3} \text{ y}^{-1}$, which are estimated from the instrumental temperature record using the Hansen-forcing. We have used $F_{2 \times \text{CO}_2} = 3.8 \text{ W/m}^2$, which is the value for the GISS-E2-R model given in Table 1. Hence this value for R is the one estimated for the effective forcing used in this particular model and applied to the observed temperature time series. Similar estimates are made for the adjusted forcing in all the other models, using the values of $F_{2 \times \text{CO}_2}$ for those models given in Table 1. The black curve in the lower part of Figure 3a is a PDF $p(R)$ for the metric R estimated this way. The PDF is obtained by considering two sources of uncertainty in the R -estimates. One is the spread in parameter estimates when we vary the forcing. The forcing is varied over the set of modified Hansen forcing time series, where each modification corresponds to a historical run of an ESM in the ensemble. The parameter estimates for the instrumental temperature record, and the resulting value of R , for varying forcing data is shown in Table 2. Another source of uncertainty is the spread in the parameters β and μ across repeated historical runs of the same model, i.e., runs where the known forcing is the same, but where chaotic dynamics create random components that vary among realizations. Table 3 shows a set of parameter estimates for repeated historical runs of the CSIRO model, which is the model in the CMIP5 ensemble that provides the largest number of runs with identical forcing. The total variability from these two sources is obtained by a simple mixture model, and the plotted PDF is computed by a smooth kernel method. The black, full curve in Figure 3b shows the PDF for ECS computed from the formula

$$p(\text{ECS}) = \int p(\text{ECS}|R)p(R)dR, \quad (14)$$

where $p(R)$ is the PDF shown in Figure 3a. The histogram in Figure 3b is the distribution of ECS in the model ensemble, and the dotted curve is a Gaussian fit to the distribution of ECS in the model ensemble. The figure demonstrates that when constrained by the scale-dependent sensitivity of the instrumental temperature record, the best estimate of ECS in the model ensemble is reduced by approximately 0.2 K. The PDF $p(R)$ shown in Figure 3a, also shows that, with the uncertainties taken into account, models with ECS larger than 4 K are inconsistent with the instrumental temperature record.

From Figure 3a and Equation (14) we observe that the uncertainty represented by $p(\text{ECS})$ in Figure 3b is formed by a combination of the range of R -values R represented by the black curve for $p(R)$ in Figure 3a and the width of the conditional PDF represented by the contour lines in that panel. The latter represents the uncertainty associated with the deviation from the emergent linear relation between ECS and R among the models, which is the main source of uncertainty found by Cox et al. (2018) [9]. In our approach, however, the wide range of the metric R represented by $p(R)$ that we have found by using the adjusted forcing of each model to estimate R is a major contribution to the uncertainty in $p(\text{ECS})$.

One can explore the effect of uncertainty of adjusted forcing among models on the uncertainty of ECS by neglecting the uncertainty associated with deviations from the emergent linear relation. From the scatter plot in Figure 3a we can fit a linear relationship $\text{ECS} = aR + b$, and in Table 2 we have a set of estimates of R for the instrumental temperature record. The linear fit maps each of the R -estimates to an ECS-value, which can be interpreted as the best estimate of ECS based on the corresponding forcing data. This mapping is shown in Figure 4a. The range of these best estimates of ECS are between 2.3 and 3.4 K. Note that these are the best estimate of R for each model and that the uncertainty of each estimate arising from uncertainty in estimates of β and μ is not taken into account. For this reason, we don't plot PDFs, but only indicate the range of best estimates of R .

Table 2. The parameter estimates for the instrumental temperature record, and the resulting values of R , for varying forcing data.

Forcing	β	μ (10^{-3} y)	σ (W/m^2)	R (K) *
GISS-E2-R	0.61	5.8	0.12	2.4
HadGEM2-ES	0.87	5.3	0.20	3.3
IPSL-CM5A-LR	0.64	6.4	0.12	2.2
NorESM1-M	0.74	6.3	0.14	2.8
Access1-0	0.67	6.3	0.12	2.3
Miroc-ESM	0.68	7.6	0.14	3.7
Miroc5	0.68	6.6	0.12	3.3
CanESM2	0.68	5.5	0.13	3.0
CCSM4	0.62	4.5	0.13	2.1
CNRM-CM5	0.69	8.2	0.13	3.3
GFDL-CM3	0.86	5.6	0.19	3.4
GFDL-ESM2G	0.75	4.4	0.14	2.3
CSIRO-MK3	0.86	6.0	0.19	3.1
BCC-CSM1-1M	0.70	3.9	0.13	2.0
GFDL-ESM2m	0.73	4.9	0.14	2.4
INM-CM4	0.67	5.9	0.12	2.2
MPI-ESM-LR	0.81	1.8	0.15	2.3
MRI-CGCM3	0.79	6.9	0.15	3.4

* In the last column $R = R(f)$ for $f = 10^{-3} \text{ y}^{-1}$.**Table 3.** A set of parameter estimates for repeated historical runs of the CSIRO model.

Ensemble Run	β	μ (10^{-3} y)	σ (W/m^2)	R (K) *
1	0.82	13.0	0.17	3.5
2	0.91	8.0	0.23	3.9
3	0.80	19.4	0.16	4.1
4	0.88	13.6	0.23	4.4
5	0.73	21.8	0.14	3.6
6	0.89	9.9	0.22	3.8
7	0.82	16.9	0.17	4.1
8	0.87	9.5	0.19	3.4
9	0.86	11.6	0.19	3.8

* In the last column $R = R(f)$ for $f = 10^{-3} \text{ y}^{-1}$.

The effect of uncertainty in the forcing on the estimated ECS can be explored further by varying the various forcing components within plausible ranges of uncertainty. As an example we consider the forcing from volcanic aerosols, which are subject to considerable controversy. In Figure 4b we have made the same plot as in Figure 4a, but with the volcanic component of the Hansen forcing reduced by 50 percent. The effect on the spread in the estimated ECS is considerable. Another source of uncertainty is the choice of regression model for the emergent relation between ECS and R . From a physical viewpoint, vanishing ECS should correspond to vanishing R , so if one sticks to a linear model it could be reasonable to choose the model $\text{ECS} = aR$ rather than $\text{ECS} = aR + b$. The result for such a model, keeping the low volcanic forcing, is shown in Figure 4c, with a range of best estimates for ECS between 1.8 and 3.7 K.

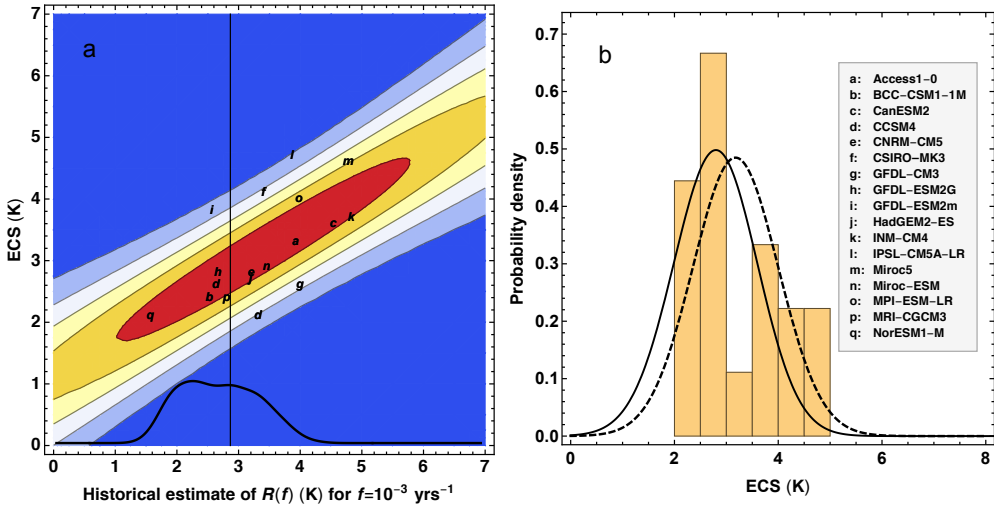


Figure 3. (a) The letters (see the legend inserted in panel (b)) show the Gregory estimate of ECS versus $R(f)$ evaluated at $f = 10^{-3} \text{ y}^{-1}$ for each model in the ensemble. The contour plot shows the conditional probability density function (PDF) $p(\text{ECS}|R)$. The vertical black line is $R = 2.9 \text{ K}$, which is obtained from the parameters $\beta = 0.66$ and $\mu = 11.9 \times 10^{-3} \text{ y}^{-1}$ estimated from the instrumental temperature record using the Hansen forcing. The thick, black curve is the estimated PDF of $R(f)$. (b) The full curve shows the PDF for ECS computed from Equation (14), where $p(R)$ is the PDF shown in (a). The histogram is the distribution of ECS in the model ensemble, and the dotted curve is a Gaussian fit to the histogram.

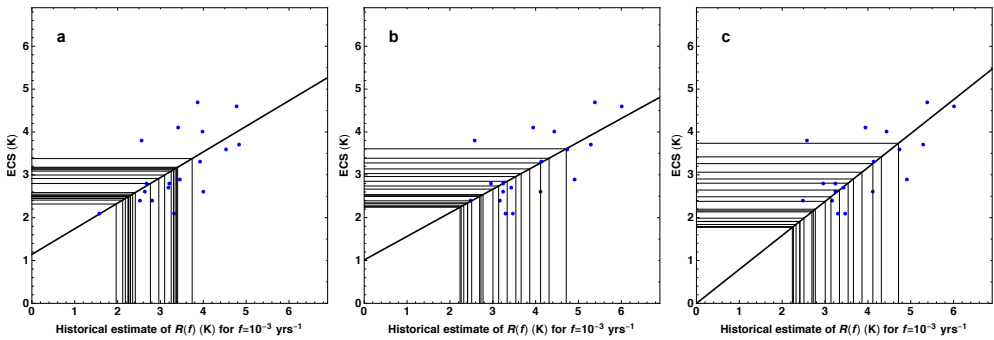


Figure 4. (a) The points in the scatter plot are the same as (the letters) in Figure 3a. The line is the least-square fit of the model $\text{ECS} = aR + b$. The vertical lines correspond to the R -values estimated from the instrumental temperature record for the different modified Hansen forcing time series. The horizontal lines show how these R -values are mapped to ECS-values by the linear model. (b) As in (a), but prior to the analysis the volcanic forcing is reduced to half of its original values. (c) As in (b), but using a linear model $\text{ECS} = aR$ with zero intercept to map R -values to ECS-values.

5. Discussion

The PDF for the ECS shown in Figure 3b is similar to the one presented by Cox et al. [9]. However, there are important differences in methodology that must be pointed out. Cox et al. use a pure dissipation-response relationship to constrain ECS in the model ensemble. They propose a metric ψ , which plays a similar role as the metric R proposed in this work, and claim that estimates of ψ are

independent of the forcing. This claim has been demonstrated to be false [10]. In our framework, an approach in the spirit of Cox et al. would be to use Equation (10), and to seek estimates of the correlation function (or equivalently the PSD) of the climate noise $X(t)$ that are independent of the forcing. Such an approach would lead to the same problems as those in [9], namely that the estimates would be influenced by the strong anthropogenic forcing in the instrumental period. This is our motivation for developing a method that employs forcing data in the estimation of our metric R , and as a consequence we have to take the uncertainty in the forcing into account. We have done this by using a fixed data set for historical forcing (the Hansen-forcing) and varied its low-frequency variability over the ensemble of adjusted forcing time series provided by Forster et al. [15]. Clearly, this does not represent the full uncertainty in the historical forcing, and hence the spread in the distribution of ECS (the black, full curve in Figure 3b) is narrower than what we expect to find if we were to model the full forcing uncertainty. We conclude that accurate estimates of the uncertainty in historical forcing is a key factor for establishing constraints on ECS in ESM ensembles.

The modeling of the relationship between R and ECS is also a source of uncertainty. It is evident from Figure 4a that the coefficient a in the linear map $\text{ECS} = aR + b$ is less than one. In fact, its estimated value is $a = 0.6$. As a consequence the mapping from R to ECS is contracting, so that the spread in ECS-values is smaller than the spread in R -values. The same is true for the analysis presented in Figure 3, since the conditional PDF $p(\text{ECS}|R)$ is constructed from the fitted line $\text{ECS} = aR + b$. We note that for a model without the intercept term b , and lower volcanic forcing, the estimated coefficient is $a = 0.91$, and the range of the best estimates of ECS becomes 1.8–3.7 K. Other assumptions about the functional relationship between R and ECS will lead to yet different ranges of best estimates.

Apart from the constraints on ECS, an important result presented in this paper is that scale-dependent climate sensitivity provides a good proxy for ECS. Moreover, despite having infinite ECS, scale-invariant linear response models are useful for estimating ECS from observational data. The advantage over multi-layer energy balance models is that the scale-invariant models have few free parameters and are less prone to statistical overfitting. The accuracy of the models is associated with the scaling nature of climate variability, an emergent property of the complex climate system.

Author Contributions: All authors conceived and designed the study; H.-B.F. collected data and constructed the modified forcing data. E.M.-N. and S.H.S. performed the parameter estimates; M.R. and H.-B.F. analyzed the results; M.R. and K.R. wrote the paper with input from all authors.

Funding: This research received no external funding.

Conflicts of Interest: The authors declare no conflict of interest.

Abbreviations

The following abbreviations are used in this manuscript:

ECS	Equilibrium climate sensitivity
ESM	Earth system model
IPCC	Intergovernmental Panel on Climate Change
GMST	Global mean surface temperature
CERES	Clouds and Earth's Radiant Energy System
CMIP5	Coupled Model Intercomparison Project Phase 5
ENSO	El Niño Southern Oscillation
PSD	Power Spectral Density
LRD	Long-range dependence
fGn	fractional Gaussian noise
PDF	Probability density function
INLA	Integrated nested Laplace approximation

References

1. IPCC. *Climate Change 2013: The Physical Science Basis. Contribution of Working Group I to the Fifth Assessment Report of the Intergovernmental Panel on Climate Change*; Cambridge University Press: Cambridge, UK, 2013.
2. Gregory, J.M.; Ingram, W.J.; Palmer, M.A.; Jones, G.S.; Stott, P.A.; Thorpe, R.B.; Lowe, J.A.; Johns, T.C.; Williams, K.D. A new method for diagnosing radiative forcing and climate sensitivity. *Geophys. Res. Lett.* **2004**, *31*, L03205. [[CrossRef](#)]
3. Knutti, R.; Rugenstein, M.A.; Hegerl, G.C. Beyond equilibrium climate sensitivity. *Nat. Geosci.* **2017**, *10*, 727–736. [[CrossRef](#)]
4. Von der Heydt, A.S.; Köhler, P.; van de Wal, P.R.S.W.; Dijkstra, H.A. On the state dependency of fast feedback processes in (paleo) climate sensitivity. *Geophys. Res. Lett.* **2014**, *41*, 6484–6492. [[CrossRef](#)]
5. Von der Heydt, A.S.; Dijkstra, H.A.; van de Wal, R.S.W.; Caballero, R.; Crucifix, M.; Foster, G.L.; Huber, M.; Köhler, P.; Rohling, E.; Valdes, P.J.; et al. Lessons on Climate Sensitivity From Past Climate Changes. *Curr. Clim. Chang. Rep.* **2016**, *2*, 148–158. [[CrossRef](#)]
6. Von der Heydt, A.S.; Ashwin, P. State dependence of climate sensitivity: Attractor constraints and palaeoclimate regimes. *Dyn. Stat. Clim. Syst.* **2017**, *1*, 1–21. [[CrossRef](#)]
7. Köhler, P.; Stap, L.B.; von der Heydt, A.S.; de Boer, B.; van de Wal, R.S.W.; Bloch-Johnson, J. A State-Dependent Quantification of Climate Sensitivity Based on Paleodata of the Last 2.1 Million Years. *Paleoceanography* **2017**, *32*, 1102–1114. [[CrossRef](#)]
8. Dessler, A.E.; Forster, O.M. An estimate of equilibrium climate sensitivity from interannual variability. *J. Geophys. Res. Atmos.* **2018**. [[CrossRef](#)]
9. Cox, P.M.; Huntingford, C.; Williamson, M. Emergent constraint on equilibrium climate sensitivity from global temperature variability. *Nature* **2018**, *553*, 319–322. [[CrossRef](#)] [[PubMed](#)]
10. Rypdal, M.; Fredriksen, H.B.; Rypdal, K.; Steene, R.J. Emergent constraints on climate sensitivity. *Nature* **2018**. [[CrossRef](#)] [[PubMed](#)]
11. Fredriksen, H.B.; Rypdal, M. Long-range persistence in global surface temperatures explained by linear multibox energy balance models. *J. Clim.* **2017**, *30*, 7157–7168. [[CrossRef](#)]
12. Rypdal, M.; Rypdal, K. Long-memory effects in linear response models of Earth's temperature and implications for future global warming. *J. Clim.* **2014**, *27*, 5240–5258. [[CrossRef](#)]
13. Myhre, G.; Myhre, C.L.; Forster, P.M.; Shine, K.P. Halfway to doubling of CO₂ radiative forcing. *Nat. Geosci.* **2017**, *10*, 710–711. [[CrossRef](#)]
14. Andrews, T.; Gregory, J.M.; Webb, M.J.; Taylor, K.E. Forcing, feedbacks and climate sensitivity in CMIP5 coupled atmosphere-ocean climate models. *Geophys. Res. Lett.* **2017**, *39*, L09712. [[CrossRef](#)]
15. Forster, P.M.; Andrews, T.; Good, P.; Gregory, J.M.; Jackson, L.S.; Zelinka, M. Evaluating adjusted forcing and model spread for historical and future scenarios in the CMIP5 generation of climate models. *J. Geophys. Res. Atmos.* **2013**, *118*, 1139–1150. [[CrossRef](#)]
16. Hansen, J.; Sato, M.; Kharecha, P.; von Schuckmann, K.; Beerling, D.J.; Cao, J.; Marcott, S.; Masson-Delmotte, V.; Prather, M.J.; Rohling, E.J.; et al. Young people's burden: Requirement of negative CO₂ emissions. *Earth Syst. Dyn.* **2017**, *8*, 577–616. [[CrossRef](#)]
17. Rypdal, M.; Rypdal, K. Late Quaternary temperature variability described as abrupt transitions on a 1/f noise background. *Earth Syst. Dyn.* **2016**, *7*, 281–293. [[CrossRef](#)]
18. Rybski, D.; Bunde, A.; Havlin, S.; von Storch, H. Long-term persistence in climate and the detection problem. *Geophys. Res. Lett.* **2006**, *33*, L06718. [[CrossRef](#)]
19. Lovejoy, S.; Schertzer, D. *The Weather and Climate: Emergent Laws and Multifractal Cascades*; Cambridge University Press: Cambridge, UK, 2013.
20. Huybers, P.; Curry, W. Links between annual, Milankovitch and continuum temperature variability. *Nature* **2005**, *441*, 329–332. [[CrossRef](#)] [[PubMed](#)]
21. Franzke, C. Long-Range Dependence and Climate Noise Characteristics of Antarctic Temperature Data. *J. Clim.* **2010**, *23*, 6074–6081. [[CrossRef](#)]
22. Fredriksen, H.B.; Rypdal, K. Spectral characteristics of instrumental and climate model surface temperatures. *J. Clim.* **2016**, *29*, 1253–1268. [[CrossRef](#)]
23. Rypdal, K.; Rypdal, M.; Fredriksen, H.B. Spatiotemporal long-range persistence in earth's temperature field: Analysis of stochastic-diffusive energy balance models. *J. Clim.* **2015**, *28*, 8379–8395. [[CrossRef](#)]

24. Rypdal, K. Global temperature response to radiative forcing: Solar cycle versus volcanic eruptions. *J. Geophys. Res. Atmos.* **2012**, *117*, D06115. [[CrossRef](#)]
25. Mandelbrot, B.; Ness, J. Fractional Brownian motions, fractional noises and applications. *SIAM Rev.* **1968**, *18*, 1088–1107. [[CrossRef](#)]
26. Rue, H.; Martino, S.; Chopin, N. Approximate Bayesian inference for latent Gaussian models using integrated nested Laplace approximations (with discussion). *J. R. Stat. Soc. Ser. B* **2009**, *71*, 319–392. [[CrossRef](#)]
27. Sørbye, S.H.; Myrvoll-Nilsen, E.; Rue, H. An approximate fractional Gaussian noise model with $\mathcal{O}(n)$ computational cost. *Stat. Comput.* **2017**. [[CrossRef](#)]
28. Myrvoll-Nilsen, E.; Sørbye, S.H.; Rypdal, M.; Fredriksen, H.B.; Rue, H. Method for estimating climate response under scaling assumption. **2018**, preprint.



© 2018 by the authors. Licensee MDPI, Basel, Switzerland. This article is an open access article distributed under the terms and conditions of the Creative Commons Attribution (CC BY) license (<http://creativecommons.org/licenses/by/4.0/>).

Paper IV

Warming trends and long-range dependent climate variability since year 1900: a Bayesian approach

Frontiers in Earth Science, **30**, 214, 2019.



Warming Trends and Long-Range Dependent Climate Variability Since Year 1900: A Bayesian Approach

Eirik Myrvoll-Nilsen, Hege-Beate Fredriksen, Sigrunn H. Sorbye and Martin Rypdal*

Department of Mathematics and Statistics, UiT The Arctic University of Norway, Tromsø, Norway

OPEN ACCESS

Edited by:

Susana Barbosa,
University of Porto, Portugal

Reviewed by:

Gunter Spöck,
Alpen-Adria-Universität
Klagenfurt, Austria
Niklas Boers,
Potsdam-Institut für
Klimafolgenforschung (PIK), Germany

*Correspondence:

Martin Rypdal
martin.rypdal@uit.no

Specialty section:

This article was submitted to
Environmental Informatics,
a section of the journal
Frontiers in Earth Science

Received: 28 February 2019

Accepted: 07 August 2019

Published: 21 August 2019

Citation:

Myrvoll-Nilsen E, Fredriksen H-B,
Sorbye SH and Rypdal M (2019)
Warming Trends and Long-Range
Dependent Climate Variability Since
Year 1900: A Bayesian Approach.
Front. Earth Sci. 7:214.
doi: 10.3389/feart.2019.00214

Temporal persistence in unforced climate variability makes detection of trends in surface temperature difficult. Part of the challenge is methodological since standard techniques assume a separation of time scales between trend and noise. In this work we present a novel Bayesian approach to trend detection under the assumption of long-range dependent natural variability, and we use estimates of historical forcing to test if the method correctly discriminates trends from low-frequency natural variability. As an application we analyze $2^\circ \times 2^\circ$ gridded data from the GISS Surface Temperature Analysis. In the time period from 1900 to 2015 we find positive trends for 99% of the grid points. For 84% of the grid points we are confident that the trend is positive, meaning that the 95% credibility interval for the temperature trend contained only positive values. This number increased to 89% when we used estimates of historical forcing to specify the noise model. For the time period from 1900 to 1985 the corresponding ratios were 42 and 52%. Our findings demonstrate that positive trends since 1900 are now detectable locally over most of Earth's surface.

Keywords: trend detection, climate change, long-range dependence, fractional Gaussian noise, bayesian methods

1. INTRODUCTION

Since the year 1900, the global mean surface temperature (GMST) has increased by almost 1 degree K due to increasing concentrations of greenhouse gases in the atmosphere. While we are far from a full understanding of the complex dynamics of Earth's climate, the cause of the industrial-era warming is well understood, and the question of detection of global warming is today of little relevance. Recent detection studies for global temperature have instead focused on identifying the onset time of the anthropogenic warming, as well as the time when the warming became statistically detectable (Abram et al., 2016). For local and regional temperatures the situation is different. Not all of Earth's surface has warmed since 1900, and in some locations the warming is small compared to the natural variability. Sutton et al. (2015) point out that the question of local detectability is highly relevant since it provides insight into the strength of the warming signal relative to the natural fluctuations for which ecosystems are adapted.

From a statistical point of view, temperature trends provide a unique challenge since the climate naturally fluctuates on an extended range of time scales. A standard set-up is to assume that a temperature anomaly time series $\Delta T(t)$ can be approximated by a model on the form:

$$\Delta T(t) = m(t) + \varepsilon(t), \quad (1)$$

where $m(t) = a + bt$ is a linear trend, and $\varepsilon(t)$ is a stochastic process (Bloomfield, 1992). In the zero-dimensional global energy-balance model (EBM),

$$C\Delta T = -\lambda\Delta Tdt + F(t)dt + \sigma_{OU}dB(t), \quad (2)$$

the unforced temperature fluctuations $\varepsilon(t)$ are defined by the equation $Cd\varepsilon = -\lambda\varepsilon dt + \sigma_{OU}dB(t)$, which describes an Ornstein-Uhlenbeck (OU) process (the continuous interpretation of a first-order auto-regressive (AR1) process) with a characteristic correlation scale $\tau = C/\lambda$:

$$\varepsilon(t) = \frac{\sigma_{OU}}{C} \int_{-\infty}^t e^{-(t-s)/\tau} dB(s).$$

In the equations above, C is the average heat capacity of Earth's surface, λ is the feedback parameter, and $F(t)$ is a forcing record. For this model, parameter estimates in temperature time series yield values of τ that are much shorter than those relevant for the warming trend. Hence, there is a separation of time scales that makes it easy to estimate the characteristics of the noise process without influence from the long-term trend. However, the zero-dimensional EBM in Equation (2) does not model the slow thermal response of the deep oceans, and the generalization to the so-called 2-box EBM (Geoffroy et al., 2013) gives a noise model on the form:

$$\varepsilon(t) = \int_{-\infty}^t G(t-s)dB(s),$$

where the response function $G(t) = c_1e^{-t/\tau_1} + c_2e^{-t/\tau_2}$ is a sum of two exponential functions. The generalization to N -box models gives response functions that are sums of N exponential functions. Models with multiple characteristic time scales are consistent with observations. Estimated power spectral densities (PSDs) of temperature reconstructions show approximate scale invariance, i.e., $S(f) \sim f^{-\beta}$, for frequencies corresponding to time scales from months to several hundred thousand years (Rypdal and Rypdal, 2016). Analyses of the relation between reconstructed forcing and reconstructed temperatures, as well as experiments in Earth System Models (ESMs), show approximate scale invariance in the climate response and in unforced climate variability on time scales from months to several hundred years (Rypdal and Rypdal, 2014; Rypdal et al., 2018). The implication for trend detection is that the noise processes that represent natural variability should be allowed to exhibit long-range dependence (LRD). A parsimonious model with LRD is obtained by using a power-law response function $G(t) = (t/\mu)^{\beta/2-1}$. With this choice, the noise model $\varepsilon(t)$ is a fractional Gaussian noise (fGn). The parameter β is identical to the exponent in the PSD and related to the so-called Hurst exponent via the relation $\beta = 2H - 1$.

We write the discrete-time version of Equation (1) on the following vector form:

$$\mathbf{y} = (y_1, \dots, y_n)^T = (m(t_1) + \varepsilon(t_1), \dots, m(t_n) + \varepsilon(t_n))^T, \quad (3)$$

where \mathbf{y} is the temperature time series. Using the short-hand notation $\varepsilon_i = \varepsilon(t_i)$, the vector $\boldsymbol{\varepsilon} = (\varepsilon_1, \dots, \varepsilon_n)^T$ is a

zero-mean stationary Gaussian process with covariance function (Mandelbrot and Ness, 1968):

$$\text{Cov}(\varepsilon_i, \varepsilon_j) = \frac{\sigma_\varepsilon^2}{2} (|i-j+1|^{2H} + |i-j-1|^{2H} + |i-j|^{2H}). \quad (4)$$

Several previous studies have modeled climatic data using a linear trend model $m(t_i) = a + bt_i$, $i = 1, \dots, n$, and an LRD noise term (Cohn and Lins, 2005; Koutsoyiannis and Montanari, 2007; Franzke, 2012; Løvsetten and Rypdal, 2016). Some of these studies conclude that trends that have been identified as statistically significant based on AR1 noise models, are not found to be significant when LRD noise models are used. Ideally, the parameters in the noise model (the Hurst exponent H and the scale parameter σ_ε) and the parameters in the trend model (the intercept a and the slope b) should be estimated simultaneously, but most previous studies have used non-parametric measures of the second-order statistics to determine the Hurst exponent. A standard approach is to estimate a trend using a least-squares method, and to subsequently estimate a Hurst exponent and a scale parameter of the de-trended signal using a fluctuation function over a range of time scales. The fluctuation function could be a wavelet-based fluctuation function, a variogram, the de-trended fluctuation (DFA) function, or the PSD. The significance of a positive trend can then be tested using Monte-Carlo simulations, or by theoretical estimates based on the specified noise model. The disadvantage of the two-step approach is that it does not fully take into account the dependence between the estimates of the trend and the estimates of the noise parameters. Part of the reason why fluctuation-based estimators of H and σ_ε are popular is that likelihood-based methods are computationally costly for processes with LRD. Computing the likelihood function involves inversions of the dense covariance matrix $\boldsymbol{\Sigma}$ defined by the elements $\Sigma_{ij} = \text{Cov}(\varepsilon_i, \varepsilon_j)$ in Equation (4).

In this paper we take advantage of recent work by Sørbye et al. (2019) who incorporate fGn models within a Bayesian hierarchical formulation using the computational framework of latent Gaussian models. These models can be analyzed efficiently using the methodology of integrated nested Laplace approximation (INLA) developed in Rue et al. (2009). The INLA methodology provides accurate estimates of the posterior marginal distributions for all of the model parameters which can then be used to calculate summary statistics like posterior means, variances, credible intervals, and posterior probabilities. Of particular interest is the posterior marginal distribution $p(b | \mathbf{y})$, which is used to calculate the probability $\text{Prob}[b > 0 | \mathbf{y}]$ of a positive trend given the observed temperature anomalies \mathbf{y} . The Bayesian modeling approach is described further in section 2. In section 3 we discuss an alternative approach to trend detection where data of historical forcing is used to discriminate between forced response and natural variability. The results of the latter is used to test and validate the methods described in section 2. Results of analyses of gridded temperature data from the GISS Surface Temperature Analysis are presented in section 4, and discussed in section 5.

2. BAYESIAN INFERENCE

To analyse the regression model defined by Equation (3) for a large number of gridded time series, computational efficiency is crucial. The presented Bayesian approach makes use of the computational framework of latent Gaussian models. These models can be seen as a flexible class of three-stage Bayesian hierarchical models where the different stages specify the distribution of an observational vector \mathbf{y} , a Gaussian prior for a latent random field \mathbf{x} and priors for random hyperparameters $\boldsymbol{\theta}$. The first stage of the model assumes that the observations are conditionally independent given the latent field and the hyperparameters. The resulting joint conditional distribution of the observations is then expressed as the product of the marginals:

$$p(\mathbf{y} | \mathbf{x}, \boldsymbol{\theta}) = p(y_1 | x_1, \boldsymbol{\theta}) \cdots p(y_n | x_n, \boldsymbol{\theta}).$$

In our case, the observations represent the temperature time series at some grid point and are assumed to have a Gaussian distribution and the marginals are just univariate Gaussian distributions. We consider each local time series independently and thus do not include spatial correlation.

The second stage of the latent Gaussian model formulation specifies that the conditional distribution of \mathbf{x} given $\boldsymbol{\theta}$ is a Gaussian random field. Based on the regression formulation in Equation (3), the expectation of \mathbf{y} is modeled in terms of a linear predictor, $\boldsymbol{\eta} = E(\mathbf{y})$. The latent field \mathbf{x} includes all the random variables of the predictor $\mathbf{x} = (a, b, \boldsymbol{\epsilon})^T$. By assigning Gaussian priors to all of these variables, \mathbf{x} will also be Gaussian and this is what separates a latent Gaussian model from general three-stage Bayesian hierarchical models. The conditional distribution of \mathbf{x} given hyperparameters is then defined by:

$$\mathbf{x} | \boldsymbol{\theta} \sim \mathcal{N}(\boldsymbol{\mu}, \mathbf{Q}^{-1}) \quad (5)$$

where $\boldsymbol{\mu}$ denotes the mean vector and \mathbf{Q} is the precision (inverse covariance) matrix of all the random variables in \mathbf{x} . The matrix \mathbf{Q} reflects conditional independence properties of the elements in \mathbf{x} , giving zeros for all combinations of elements x_i and x_j that are independent conditioned on the other elements of \mathbf{x} . Usually, \mathbf{x} is assumed to be a Gaussian Markov random field (GMRF) implying that the precision matrix \mathbf{Q} will be sparse.

The final stage of the model formulation specifies priors for the hyperparameters which here include $\boldsymbol{\theta} = (H, \sigma_\epsilon)$. Assuming independent priors, the probability density function is $p(\boldsymbol{\theta}) = p(H)p(\sigma_\epsilon)$ where both parameters are assigned penalized complexity priors (Simpson et al., 2017). This is a recently developed class of priors which introduces a framework to compute priors for hyperparameters based on specific principles. For scaling parameters such as σ_ϵ , the PC prior can be computed to equal the exponential distribution. The PC prior for the Hurst exponent is computed numerically as explained in Sørbye and Rue (2018). Using Bayes theorem, the posterior joint distribution of the latent field and the hyperparameters is expressed as:

$$p(\boldsymbol{\theta}, \mathbf{x} | \mathbf{y}) \propto \prod_{i=1}^n p(y_i | x_i, \boldsymbol{\theta}) p(\mathbf{x} | \boldsymbol{\theta}) p(H) p(\sigma_\epsilon). \quad (6)$$

The main aim of the current analysis is to find the posterior marginal distributions $p(b | \mathbf{y})$, $p(H | \mathbf{y})$ and $p(\sigma_\epsilon | \mathbf{y})$. These distributions are then used to find summary statistics for the parameters. Especially, significance of warming trends are assessed by the probability of $b > 0$ according to the density $p(b | \mathbf{y})$. More generally, posterior marginal distributions for all components of \mathbf{x} and the hyperparameters in $\boldsymbol{\theta}$ might be of interest. Theoretically, such marginals are expressed by integrating out all other variables in Equation (6), but this is not a computationally feasible approach. Posterior samples from the posterior marginals can be obtained using Markov chain Monte Carlo approaches (Geman and Lopes, 2006), but this is computationally slow as such approaches are simulation-based. The INLA methodology (Rue et al., 2009) represents an accurate and computationally superior alternative as it estimates the posterior marginals without any simulations, combining numerical approximations with numerical interpolation and integration (see Rue et al., 2017) for a recent review. In order for INLA to be computationally fast, the latent field \mathbf{x} needs to be a GMRF having a sparse precision matrix \mathbf{Q} in Equation (5). This is not the case when the noise term $\boldsymbol{\epsilon}$ is fGn having an LRD structure, but the precision matrix of an AR1 process is tridiagonal. In Sørbye et al. (2019), the fGn process is approximated using a weighted sum of AR1 processes where the weights and the first-lag autocorrelation coefficients of the approximation are optimized such that the covariance function of the approximation matches the exact covariance function of fGn defined in Equation (4). The latent field \mathbf{x} is extended to include the AR(1) components that make up the approximation. This implies that full Bayesian inference is obtained for these as well. For the time scales of interest, the approximation is very accurate using a sum of only four AR1 processes. This speeds up the model fitting of Equation (3) considerably, see section 4 for results.

3. USING HISTORICAL FORCING TO SPECIFY NOISE MODELS

The alternative approach to trend detection that we present in this paper makes use of the historical global data of radiative forcing $F(t)$ (an updated version of the forcing in Hansen et al., 2011). This is done to validate the results of the approach in section 2 which does not account for information about radiative forcing. For the EBM in Equation (2), the forced temperature response is:

$$\Delta T(t) = \frac{1}{C} \int_{-\infty}^t e^{-(t-s)/\tau} F(s) ds + \frac{\sigma_{\text{OU}}}{C} \int_{-\infty}^t e^{-(t-s)/\tau} dB(s).$$

Expressed as in (1) we get that $\varepsilon(t)$ is an OU model with characteristic correlation length τ and,

$$m(t) = \frac{1}{C} \int_{-\infty}^t e^{-(t-s)/\tau} F(s) ds$$

is a convolution of the exponential kernel $e^{-t/\tau}$ with the historical forcing.

Rypdal and Rypdal (2014) proposed an LRD modification of this model in discrete time where ε in Equation (3) is an fGn process with Hurst exponent H , variance σ_ε^2 , and mean function:

$$m(t_i) = \sigma_f \sum_{s=-\infty}^{t_i} (t_i - s)^{H-3/2} (F_0 + F(s)), \quad i = 1, \dots, n. \quad (7)$$

The parameter F_0 is introduced to make sure that the forcing records $F(t_i)$ have the correct mean as this a relative measure, while σ_f is an additional scaling parameter. Myrvoll-Nilsen et al. (submitted) extend the methodology described in section 2 to analyse models where the fGn process has mean defined by Equation (7). This approach is more computationally demanding as it introduces the additional hyperparameters σ_f and F_0 , such that $\theta = (H, \sigma_\varepsilon, \sigma_f, F_0)$. Here, F_0 is assigned a vague Gaussian prior, while the other hyperparameters are assigned penalized complexity priors.

Figure 1 shows surface temperature anomalies from two grid points, one located around the city of Moscow (55N, 37E), and one location in the tropical Pacific ocean (33S, 120W). The dotted blue lines show the estimated linear trend $m(t_i) = a + bt_i$ using the methods described in section 2, and the solid black curves are the estimated forced responses in Equation (7). Using historical forcing implies that we are imposing a global warming signal, and hence estimates of increasing functions $m(t_i)$ can not be considered as detection of warming trends. However, our purpose is not to obtain estimates of $m(t_i)$, but rather to estimate the parameters in the noise term ε when the forced response is modeled more realistically than a linear function. Hence, our second method for trend detection is to use a linear model $m(t_i) = a + bt_i$ together with a noise model ε , where the parameters σ_ε and H are fixed and equal to the posterior marginal mean values obtained from the model where $m(t_i)$ is given by Equation (7).

4. RESULTS

In this section we present results for $2^\circ \times 2^\circ$ gridded data from the GISS Surface Temperature Analysis. Annual data is used and parameter estimates are given for those time series that have no more than 5% missing values. We have used the two different methods described in sections 2 and 3, respectively. **Figure 2** shows maps of estimates for the trend parameter b , and the noise parameters σ_ε and H for the time period 1900–2015. The presented estimates are the posterior means obtained from the estimated posterior marginal distributions. The method described in section 2 is used to obtain the estimates in **Figures 2A,C,E**, and the method described in section 3 is used to obtain the estimates in **Figures 2B,D,F**. It is well-known that the Hurst exponents are higher for sea-surface temperatures than for land temperatures (Fraedrich and Blender, 2003; Monetti et al., 2003; Fredriksen and Rypdal, 2016), and this is confirmed in this study. We also observe stronger warming trends in the Arctic compared with the rest of Earth's surface, consistent with polar amplification. Of the 11,997 grid points that are analyzed, 11,883 and 11,906 had positive estimates for the trend parameter b for the two methods, respectively.

The two methods presented do give quite similar results for the parameters b , σ_ε , and H , indicating that the method described in section 2 produces reasonable estimates of the noise parameters. However, **Figure 3** shows that the root mean square error, defined by:

$$\text{RMSE} = \sqrt{\frac{\sum_{i=1}^n (y_i - \hat{m}(t_i))^2}{n}}, \quad (8)$$

where $\hat{m}(t_i)$ is the posterior marginal mean of $m(t_i)$, is generally higher when a linear trend is used. Hence, the noise processes need to account for more variability in the models described in section 2 than in the models described in section 3. This effect can also be seen in **Figure 4**, which summarizes the main findings of this work, but the effect is very subtle. **Figures 4A,C,E** show the posterior probability of a positive linear trend given the observed temperature time series for each grid point using the method described in section 2, and **Figures 4B,D,F** show the same numbers obtained using the method described in section 3. **Figures 4A,B** show results for the years 1900–1950, **Figures 4C,D** show results for the years 1900–1985, and **Figures 4E,F** show results for the time period 1900–2015. Using data up to the year 1950 we find $\text{Prob}[b > 0 \mid \mathbf{y}] > 0.95$ for 3571 and 4,606 out of the 11,997 analyzed grid points, for the two methods, respectively. These numbers increase to 5,140 and 6,223 if the time period extends to year 1985. And to 10,121 and 10,683 when the analysis includes all years from 1900 to 2015. **Figure 4** shows that there are large areas in the oceans where the sea-surface temperature warming signal has become detectable over the last 30 years.

Fitting the model in Equation (3) where the linear trend and the parameters of the fGn model are estimated simultaneously, required on average 2.7 s per time series. This gives a total elapsed computation time of ~ 9 h for all 11,997 grid points. Using the approach described in section 3, we first fit an fGn process where the mean is specified by Equation (7). The average run time to fit this model to a single time series was almost 8 s, giving a total run time of ~ 25.9 h. The second step of the method in section 3 fits the linear trend combined with the fGn noise term using fixed parameters. Fitting of this model required on average 1.5 s for individual time series, giving a total elapsed computation time of ~ 5 h for all grid points. The main reason for the increased computation time of the approach described in section 3 compared with the method in section 2 is the increased number of hyperparameters. Also, fitting of the model including radiative forcing required extensions to existing software, see Myrvoll-Nilsen et al. (submitted) for further details.

5. DISCUSSION AND CONCLUSIONS

The main contribution of this paper is to present a computationally efficient Bayesian method for trend-detection under the assumption of LRD noise, and to apply the method to detection of global warming in gridded temperature data. By considering two different methods, where the second

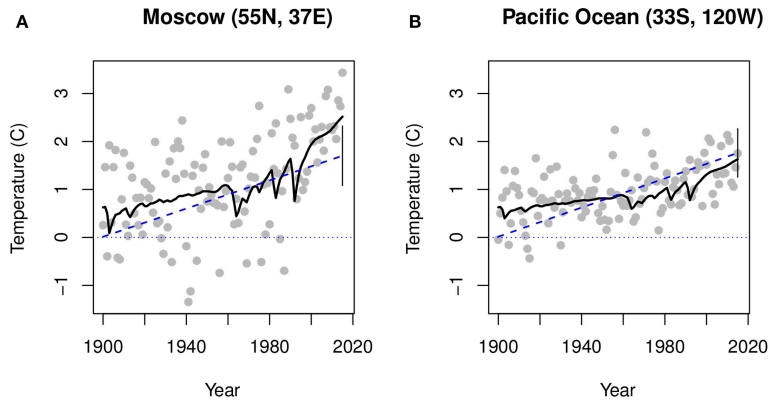


FIGURE 1 | (A) Shows surface temperature anomalies for a grid point located around the city of Moscow (55N, 37E). The dotted blue line shows the estimated linear trend $m(t) = a + bt$ estimated using the method described in section 2, and the solid black curve is the estimated forced responses in Equation (7). **(B)** As in **(A)**, but for a location in the tropical Pacific ocean (33S, 120W). For both panels the black vertical line show the 95% credible intervals at year 2015.

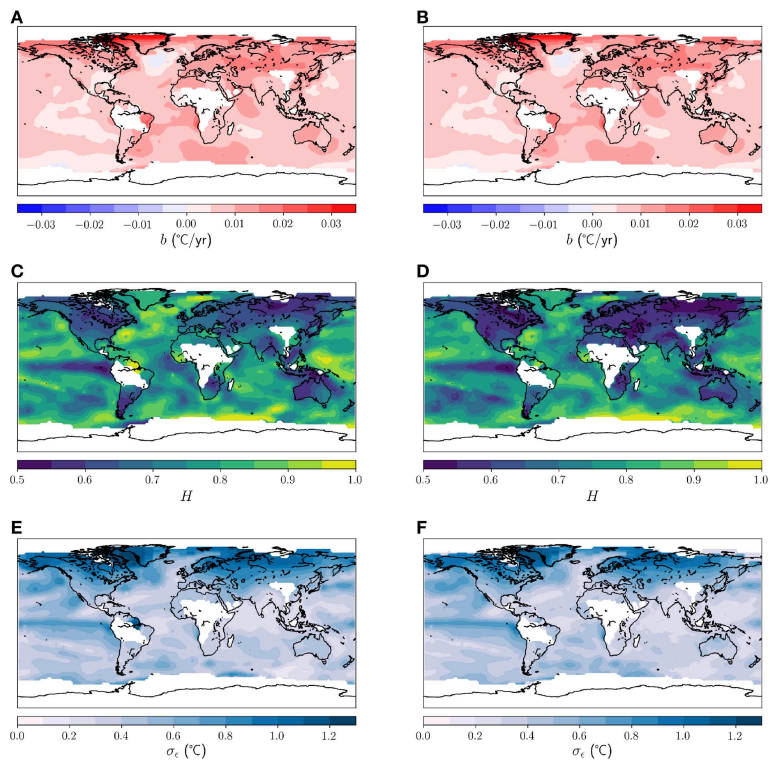


FIGURE 2 | Shows maps of estimates for the trend parameter b , and the noise parameters σ_ϵ and H for the time period 1900–2015. The presented estimates are the posterior means obtained from the estimated posterior marginal distributions. **(A)** Estimates of b using the methods described in section 2. **(B)** Estimates of b using the methods described in section 3. **(C)** Estimates of H using the methods described in section 2. **(D)** Estimates of H using the methods described in section 3. **(E)** Estimates of σ_ϵ using the methods described in section 2. **(F)** Estimates of σ_ϵ using the methods described in section 3.

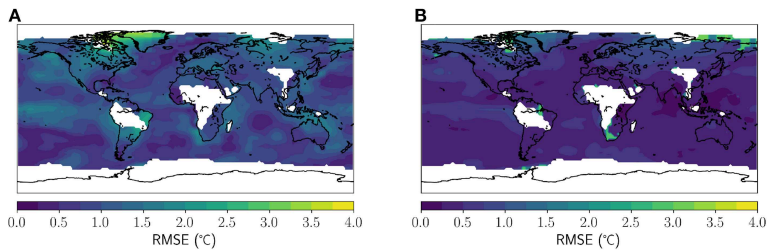


FIGURE 3 | The root mean square error (RMSE) as defined in Equation (8), measuring a standardized difference between the observed temperature signal and the trend model. **(A)** The RMSE for the model defined in section 2. **(B)** The RMSE for the model defined in section 3.

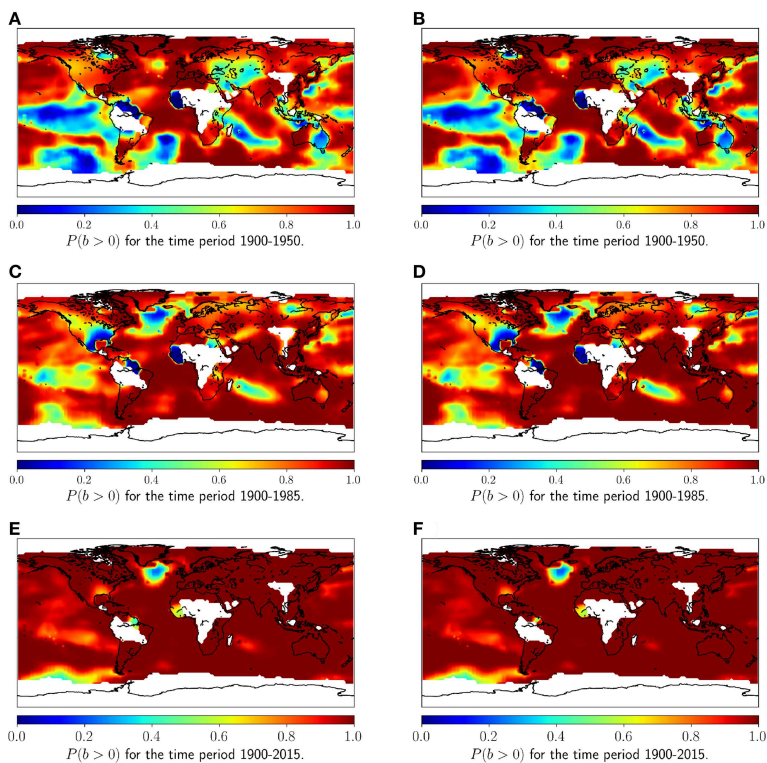


FIGURE 4 | The posterior probability of a positive linear trend given the observed temperature time series for each grid point. **(A)** For the time period 1900–1950 using the method described in section 2. **(B)** For the time period 1900–1950 using the method described in section 3. **(C)** For the time period 1900–1985 using the method described in section 2. **(D)** For the time period 1900–1985 using the method described in section 3. **(E)** For the time period 1900–2015 using the method described in section 2. **(F)** For the time period 1900–2015 using the method described in section 3.

uses historical data for global radiative forcing, we validate that the inaccuracy of a linear trend model does not affect the specification of the trend model to such a degree that it significantly affects the trend-detection results. Hence, we avoid a situation where the presence of non-linear temperature trends

produce biased estimates of σ_ε and H , which again affect the trend detection.

The results presented in this paper imply that even by the most conservative estimates, more than 84% of the analyzed grid points show significant warming at the 0.05-level. This ratio is

higher than the 80% ratio that Løvstetten and Rypdal (2016) obtained after making a model selection between ARI and fGn for each grid point, and much higher than what they obtain for a pure fGn model. Our results also show a striking difference for the time period 1900–2015 compared to 1900–1985, and clearly demonstrate that even locally, the warming signal has emerged from the noise over the last 30 years.

The limitations of the approach presented here is that noise models are restricted to the class of fGns. Whereas LRD models are highly accurate on decadal time scales in GMST, local temperatures exhibit modes of internal variability that are not well-approximated by scale invariance. The most prominent example being the El Niño Southern Oscillation (ENSO). We therefore believe that future work on trend detection in surface temperature data should be based on more flexible models, with more free parameters. The introduction of more flexible models must be weighed against the risk of statistical overfitting for the relatively short instrumental temperature record. An alternative approach is to characterize internal variability as the fluctuations around ensemble means in historical runs in ESMs. Using randomization of phases one can then run Monte-Carlo simulations without specifying parametric models. However, since spatial patterns of internal variability vary between models it is difficult to ensure that the unforced fluctuations in a particular grid point is a good representation of the unforced fluctuations of this grid point in the real climate system.

REFERENCES

- Abram, N. J., McGregor, H. V., Tierney, J. E., Evans, M. N., McKay, N. P., Kaufman, D. S., et al. (2016). Early onset of industrial-era warming across the oceans and continents. *Nature* 536, 411–413. doi: 10.1038/nature19082
- Bloomfield, P. (1992). Trends in global temperature. *Clim. Change* 21, 1–16.
- Cohn, T. A., and Lins, H. F. (2005). Nature's style: naturally trendy. *Geophys. Res. Lett.* 32:L23402. doi: 10.1029/2005GL024476
- Fraedrich, K., and Blender, R. (2003). Scaling of atmosphere and ocean temperature correlations in observations and climate models. *Phys. Rev. Lett.* 90:108501. doi: 10.1103/PhysRevLett.90.108501
- Franzke, C. (2012). On the statistical significance of surface air temperature trends in the Eurasian Arctic region. *Geophys. Res. Lett.* 39:L23705. doi: 10.1029/2012GL054244
- Fredriksen, H.-B., and Rypdal, K. (2016). Spectral characteristics of instrumental and climate model surface temperatures. *J. Climate* 29, 1253–1268. doi: 10.1175/JCLI-D-15-0457.1
- Gamerman, D., and Lopes, H. (2006). *Markov Chain Monte Carlo: Stochastic Simulation for Bayesian Inference*, 2nd Edn. New York, NY: Chapman & Hall/CRC.
- Geoffroy, O., Saint-Martin, D., Ollivé, D. J. L., Voldoire, A., Bellon, G., and Tytca, S. (2013). Transient climate response in a two-layer energy-balance model. Part I: analytical solution and parameter calibration using CMIP5 AOGCM experiments. *J. Climate* 26, 1841–1857. doi: 10.1175/JCLI-D-12-00195.1
- Hansen, J., Sato, M., Kharecha, P., and von Schuckmann, K. (2011). Earth's energy imbalance and implications. *Atmos. Chem. Phys.* 11, 13421–13449. doi: 10.5194/acp-11-13421-2011
- Koutsoyiannis, D., and Montanari, A. (2007). Statistical analysis of hydroclimatic time series: uncertainty and insights. *Water Resour. Res.* 43:W05429. doi: 10.1029/2006WR005592
- Løvstetten, O., and Rypdal, M. (2016). Statistics of regional surface temperatures after 1900: long-range versus short-range dependence and significance of warming trends. *J. Climate* 29, 4057–4068. doi: 10.1175/JCLI-D-15-0437.1
- Mandelbrot, B., and Ness, J. (1968). Fractional Brownian motions, fractional noises and applications. *SIAM Rev.* 18, 1088–1107.
- Monetti, R. A., Havlin, S., and Bunde, A. (2003). Long-term persistence in the sea surface temperature fluctuations. *Phys. A Stat. Mech. Appl.* 320, 581–589. doi: 10.1016/S0378-4371(02)01662-X
- Rue, H., Martino, S., and Chopin, N. (2009). Approximate Bayesian inference for latent Gaussian models using integrated nested Laplace approximations (with discussion). *J. R. Stat. Soc. Ser. B* 71, 319–392. doi: 10.1111/j.1467-9868.2008.00700.x
- Rue, H., Riebler, A., Sørbye, S. H., Illian, J. B., Simpson, D. P., and Lindgren, F. K. (2017). Bayesian computing with INLA: a review. *Ann. Rev. Stat. Appl.* 4, 395–421. doi: 10.1146/annurev-statistics-060116-054045
- Rypdal, M., Fredriksen, H.-B., Myrvoll-Nilsen, E., Rypdal, K., and Sørbye, S. H. (2018). Emergent scale invariance and climate sensitivity. *Climate* 6:93. doi: 10.3390/cli6040093
- Rypdal, M., and Rypdal, K. (2014). Long-memory effects in linear response models of earth's temperature and implications for future global warming. *J. Climate* 27, 5240–5258. doi: 10.1175/JCLI-D-13-00296.1
- Rypdal, M., and Rypdal, K. (2016). Late quaternary temperature variability described as abrupt transitions on a 1/f noise background. *Earth Syst. Dynam.* 7, 281–293. doi: 10.5194/esd-7-281-2016
- Simpson, D., Rue, H., Riebler, A., Martins, T. G., and Sørbye, S. H. (2017). Penalising model component complexity: a principled, practical

DATA AVAILABILITY

Software for the INLA methodology is available at `R-INLA.org` for the programming environment R. INLA allows for fast Bayesian inference for latent Gaussian models such as the one described in section 2. However, some modifications are required in order to ensure efficiency. First, the latent field is of non-standard form since the mean vector and covariance matrix of the latent Gaussian field share the same parameter H , and thus requires separate specification. Second, due to the LRD assumption, the precision matrix, defined as the inverse covariance matrix, is dense and therefore unsuited for the computationally efficient algorithms that INLA applies. In order to retain sparsity we have to introduce an approximation such as that introduced by Sørbye et al. (2019). The model with these modifications are available in the R-package `INLA.climate` which can be downloaded from the GitHub repository `eirikkm/INLA.climate`. The temperature data analyzed is downloaded from `https://data.giss.nasa.gov/gistemp/`, and the forcing data from `http://www.columbia.edu/~mhs119/Forcings/`.

AUTHOR CONTRIBUTIONS

EM-N, SS, H-BF, and MR designed the study. EM-N carried out the analyses. H-BF made the figures. MR, SS, and EM-N wrote the paper with input from all authors.

- approach to constructing priors. *Stat. Sci.* 232, 1–28. doi: 10.1214/16-ST576
- Sorbye, S. H., Myrvoll-Nilsen, E., and Rue, H. (2019). An approximate fractional Gaussian noise model with $\mathcal{O}(n)$ computational cost. *Stat. Comput.* 29, 821–833. doi: 10.1007/s11222-018-9843-1
- Sorbye, S. H., and Rue, H. (2018). Fractional Gaussian noise: prior specification and model comparison. *Environmetrics* 29:e2457. doi: 10.1002/env.2457
- Sutton, R., Suckling, E., and Hawkins, E. (2015). What does global mean temperature tell us about local climate? *Philos. Trans. R. Soc. A Math. Phys. Eng. Sci.* 373:20140426. doi: 10.1098/rsta.2014.0426

Conflict of Interest Statement: The authors declare that the research was conducted in the absence of any commercial or financial relationships that could be construed as a potential conflict of interest.

Copyright © 2019 Myrvoll-Nilsen, Fredriksen, Sorbye and Rypdal. This is an open-access article distributed under the terms of the Creative Commons Attribution License (CC BY). The use, distribution or reproduction in other forums is permitted, provided the original author(s) and the copyright owner(s) are credited and that the original publication in this journal is cited, in accordance with accepted academic practice. No use, distribution or reproduction is permitted which does not comply with these terms.

